Diss. 2007 - 04
April

Projectile Continuum Electrons and the Short Wavelength Limit of Electron-Nucleus Bremsstrahlung Studied in the Collision of 90 MeV/u U^{88+} with a N_2 Target

M. Nofal

(Dissertation Universität Frankfurt)

Gesellschaft für Schwerionenforschung mbH
Planckstraße 1 · D-64291 Darmstadt · Germany
Postfach 11 05 52 · D-64220 Darmstadt · Germany

Projectile Continuum Electrons and the Short Wavelength Limit of Electron-Nucleus Bremsstrahlung Studied in the Collision of 90 MeV/u U^{88+} with a N_2 Target

Dissertation
zur Erlangung des Doktorgrades
der Naturwissenschaften

vorgelegt beim Fachbereich Physik
der Johann Wolfgang Goethe-Universität
in Frankfurt am Main

von
Muaffaq Nofal
aus Jordanien

Frankfurt am Main 2007
(DF1)

vom Fachbereich Physik der Johann Wolfgang Goethe-Universität
als Dissertation angenommen.

Dekan:	Prof. Dr. Wolf Aßmus
Gutachter:	Prof. Dr. Siegbert Hagmann
	Prof. Dr. Reinhard Dörner
Datum der Disputation:	28.03.2007

Contents

Chapter 1

Introduction

When energetic electrons enter matter they will be scattered and lose energy through the interaction with the electrons and nuclei in the medium. The interaction is primarily governed by the long range Coulomb force and can be generally thought of as collisions between the incident electrons and either the atomic electrons or the nuclei of the medium. In these collisions electrons undergo deceleration; hence they emit electromagnetic radiation. This radiation process is related to the fundamentals of the theory since it is a consequence of the general coupling of the electromagnetic field and matter fields.

There is another class of radiation phenomena in which radiation is emitted when an energetic charged ion impinges on a neutral atomic system, the so called ion-atom collision. This process constitute reaction channels of great importance not only for fundamental physics, but also in applied fields. Examples include astrophysics, radiology, radiation therapy, and material science. It is assumed that during the entire collision the distance between the two nuclei involved remains large enough so that only electromagnetic interactions prevail while strong nuclear interactions of the ionic nuclei do not play any role. In order to experimentally ensure a purely atomic collision, in which the nuclei never overlap, one has to accept only those events in which the projectile emerges intact, except perhaps for the gain or loss of one or more electrons.

In ion-atom collisions, electrons can be excited, ionized, or transferred from one collision partner to the other. The spectroscopy of electrons emitted in ion-atom collisions is based on the analysis of electron energies and scattering

angles in the final state, i.e. cross sections doubly differential in kinetic energy and emission angle for the ejected electrons. Electron spectroscopy continues to be one of the most important and sensitive tools to study the electronic structure of the collision partners and contains a wealth of necessary information on the interaction potentials and the collision dynamics [1, 2]. The rapid growth in the last three decades in basic- and application-studies using electron spectroscopy can be attributed to the advance in the technology and design of accelerators and storage rings which provided new atomic systems such as high-Z few-electron atoms and bare high-Z nuclei and thus exposed them to experimental study. Whereas experiments in the past were frustrated for lack of high resolution energy analyzers, sensitive electron detection systems, or sufficiently good vacuum for meaningful results, today there is almost bewildering array of technology and instrumentation in all these areas with which accurate results can be supplied.

The electronic emission in ion-atom collisions is a rich field of research in atomic physics and has received a great deal of attention in recent years. In particular, electrons which are emitted with nearly zero velocity relative to the projectile, called cusp electrons and appear in the laboratory frame in the forward direction with a velocity that equals the projectile velocity, and their peak structures have been the focus of a variety of experimental and theoretical investigations as the doubly differential cross section $\frac{d\sigma}{dEd\Omega}$ for the production of these cusp electrons in ion-atom collisions provides detailed information about the dynamics of the collision process [3] and its detailed comparison with the underlying theoretical models provides a stringent test of theory.

At low collision energies ($<\sim$13 *MeV/u for protons*, $<\sim$ 50 *to* 100 *MeV/u for uranium*), cusp electrons are most likely generated by either direct Coulomb electron capture from bound states of the target to low-lying continuum states of the projectile (*electron capture to continuum* ECC) or by the excitation to the projectile continuum from bound projectile states (*electron loss to continuum* ELC). A striking feature distinguishing the two cusp processes is the strong asymmetry in the velocity spectrum of the emitted electrons in the ECC process skewed to the low energy side of the cusp in contrast to the nearly symmetric ELC [4]. The important consequence of the measured asymmetry of

the ECC cusp distribution is the experimental support it has given to the theoretical claim of the importance of second Born terms in the double differential cross section as the first order theories predict a symmetric distribution [5, 6, 7].

The dynamics of the ECC process is complex and requires a violent collision with a large momentum transfer [8], it can be visualized as a continuation of the nonradiative capture to Rydberg states (NEC) across the ionization threshold of the projectile with increasingly larger orbits such that the captured electron finally becomes unbound at the continuum threshold [2, 9]. Burgdörfer [10] emphasized that a measurement of the asymmetry of the double differential cross section for the ECC cusp allows the determination of the charge asymmetry of the electron clouds in the ECC and thus provides unprecedented details of the dynamics of the transfer mechanism.

With increasing collision energy in the relativistic domain, electron capture process becomes predominantly accompanied by the emission of radiation. The radiative capture to bound (REC) and continuum states (RECC) rapidly gains importance over the nonradiative capture channels (NRC and ECC) as it exhibits a much gentler decrease with collision energy (*see equations* 2.40 *and* 2.41 *and figur*e 1.1) due to the additional radiative degree of freedom [7, 11, 12].

In the RECC and ECC processes initial and final states are identical except for the presence of a photon appearing with the RECC. The photons emitted from RECC have the same physical origin as those emitted from REC which is due to the radiative electron capture into the projectile ion, followed by x-ray emission. The difference is the final state of the electron in the projectile ion; a discrete bound state in the case of REC and a continuum state in the case of RECC. Consequently, the cross sections for REC and RECC exhibit different dependence on the projectile charge Z_p and projectile velocity v_p as discussed by Shakeshaft and Spruch [14].

A detailed analysis of the RECC [6, 7] laid open the close relationship between the RECC process and the bremsstrahlung radiation process: the radiative capture of an electron from a bound target state into a low-lying continuum state of the heavy projectile appears in the projectile rest frame

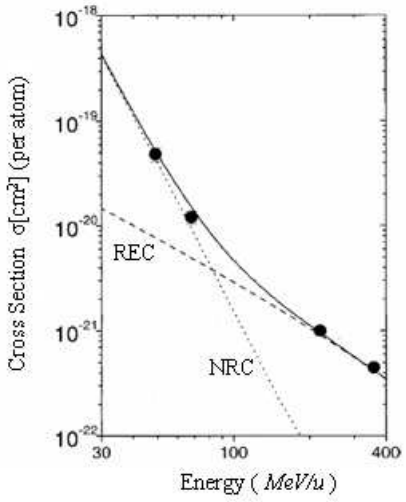

Figure 1.1: Total electron-capture cross sections for U^{92+} on a N_2 target versus projectile energy. The dotted line represents the result of the eikonal approach for the NRC process. The dashed line gives the prediction obtained within the dipole approximation for the REC process. The solid line refers to the sum of both predictions. Figure adapted from [13].

(*i.e. in inverse kinematics*) as the fundamental process of electron-nucleus bremsstrahlung at the short wavelength limit where the entire kinetic energy of an incident electron is transferred to a photon due to the interaction with the target nucleus.

It deserves to be emphasized that the complete differential cross sections for the short wavelength limit of electron nucleus bremsstrahlung are not accessible using standard experimental configurations [15] in which bremsstrahlung is measured during electron scattering from solid targets, simply because electrons which have during their collision lost almost their entire kinetic energy cannot escape from the target foil. This means, coincidences between x-ray photons and outgoing electrons of near zero kinetic energy could not be accomplished. For this reason complete differential cross sections for electron nucleus bremsstrahlung reported in the literature cover only the soft x-ray regions and those of moderate energy loss of the incident electron [15]. There are numerous treatises on e-n bremsstrahlung in the literature, the high frequency end of the photon spectrum is only scarcely covered. To the best of our knowledge, the fundamentally interesting short wavelength limit of the e-

n bremsstrahlung with its profound intrinsic relationship to photo-ionization (*section* 2.1.3) could not be studied up to now in kinematically complete fashion. We thus turn our attention to the study of coincidences between electrons in the RECC cusp and outgoing photons as a study in inverse kinematics which should eventually lead to the long desired fully differential cross sections for e-n bremsstrahlung at the short wavelength limit.

In the course of the present work, which represents a first step in a series of experiments, we report a measurement of the RECC and the differential cross sections for e-n bremsstrahlung produced by 90 MeV/u U^{88+} beryllium-like uranium impinging upon N_2 gaseous target. Particular attention has been paid to the short wavelength limit (*hard photon emission*) of the spectrum and its relation to the radiative electron capture to continuum RECC.

The experiment was performed by means of a forward electron spectrometer which is implemented in the experimental storage ring ESR at GSI in Darmstadt (www.gsi.de) and dedicated to 0° electron spectroscopy. As emphasized in a commissioning phase, the spectrometer is capable of guiding fast electrons emitted in the forward direction in a narrow cone around the beam direction towards a position and time sensitive detector. This electron spectrometer is being joined presently (*fall 2006*) to a reaction microscope to enable for the first time for kinematically complete experiments at relativistic energies. Before being implemented in the ESR, the reaction microscope was mounted temporarily in the linear accelerator (UNILAC) and used for studies of dynamics of simultaneous target and projectile ionization [16, 17]. Here, we report also a detailed description of the construction of the reaction microscope and its advantages and limitations besides the first experimental results for simultaneous target and projectile ionization in the collision of 3.6 MeV/u Ne^{3+} ions and argon target.

The present thesis is organized as follows: the theoretical aspects are discussed in chapter 2, including the forward electron emission in ion-atom collisions and the classical and quantum mechanical points of view of the electron nucleus bremsstrahlung. The short wavelength limit and its close relation to the RECC as inverse kinematics is also presented. A short summery of the binary encounter process and the kinematics of inelastic ion-atom collisions

is also given at the end of this chapter. In chapter 3 we discuss in details the experimental setup used for the two experiments reported in this work. The forward electron spectrometer is described together with the electronics for the data acquisition system and the commissioning phase results. The reaction microscope is also described in this chapter with the detectors used and its momentum resolution. The experimental results obtained using the reaction microscope at low energy are also presented in this chapter. Chapter 4 represents the actual experimental results on the short wavelength limit of e-n bremsstrahlung and the collected x-ray spectrum coincident with RECC electrons. The observed forward-backward asymmetries of ECC and RECC are presented together with the symmetric ELC and cusp electron distributions. The performed measurements and the obtained results are summarized in English in chapter 5 and in German in chapter 6. In chapter 7 a view into the future is given.

Chapter 2

Theoretical and Experimental Background

2.1 Elementary Process of Electron-Nucleus Bremsstrahlung

The emission of radiation in the scattering of an electron from an atom is called bremsstrahlung, German for "breaking radiation", because it was first observed when high energy electrons were stopped in a thick metallic target. In fact, bremsstrahlung radiation gains its importance from the fact that it constitutes the simplest reaction beyond pure elastic scattering because the final state consists of two interacting fragments plus a photon while other inelastic processes, such as particle production, involve three or more interacting particles. In addition, bremsstrahlung radiation represents an important x-ray production mechanism in ion-atom collisions and for very heavy projectiles contains information about the coupling of electromagnetic field with matter in the presence of strong fields.

In a bremsstrahlung event, the main force acting on the incident electron leading to bremsstrahlung emission is due to the Coulomb field of the nuclear charge. The bremsstrahlung radiation which results from the interaction between an incident electron and the nucleus of the target atom is called electron-nucleus bremsstrahlung (*e-n bremsstrahlung*). The effect of the

atomic electrons is twofold: On the one hand, the charge distribution of the atomic electrons screens the Coulomb field of the target nucleus as a static charge distribution. the main consequence of the screening is a reduction in the cross section for bremsstrahlung emission corresponding to a reduction in the effective charge seen by the electron being scattered by the atom. The reduction is largest at large impact parameters for which the nuclear charge is nearly completely shielded, the reduction is least at small impact parameters (*interior atomic distances*) and even negligible at relativistic collision velocities [18]. On the other hand, the atomic electrons may act as individual particles and the bremsstrahlung process may also take place in the collision with an atomic electron. The bremsstrahlung radiation which results from the interaction between the incident electron and the orbital electrons of the target atom is called electron-electron bremsstrahlung (*e-e bremsstrahlung*). The e-e bremsstrahlung in general gives a small contribution to the total bremsstrahlung emission that it is not taken into account in most bremsstrahlung measurements. Especially in the case of high-Z targets, the experiments give almost pure e-n bremsstrahlung, since the e-n bremsstrahlung is closely proportional to Z_T^2, Z_T being target atomic number, whereas the e-e bremsstrahlung is proportional to the number of electrons, i.e. Z_T for neutral targets [19, 20]. Besides, the e-e system has no electric dipole moment so that at non-relativistic energies the e-e quadrupole radiation is much weaker than the dipole radiation of the electron-nucleus system. The e-n bremsstrahlung is thus considered always to be the dominant source of producing bremsstrahlung radiation. It is, however, not always easy to distinguish experimentally between bremsstrahlung photons produced in the fields of atomic nuclei and of the atomic electrons [21, 22, 23]. The only way to isolate neatly the contribution of e-e bremsstrahlung is based on coincidence measurements of the differential cross section [24, 25, 26, 27, 20].

The term "elementary process of bremsstrahlung" means that not only the emitted bremsstrahlung photons are considered but also the pertinent scattered electrons. Experimentally the elementary process is observed by detecting the photons in coincidence with outgoing electrons scattered inelastically into a particular direction. Although such a coincidence experiment between

emitted photons and outgoing electrons had been suggested as early as 1932 by Scherzer [28], the first measurements of the elementary bremsstrahlung process have been performed beginning in 1966 by Nakel [29, 30, 31], those of the elementary process of e-e bremsstrahlung beginning in 1972 by Nakel and Pankau [24, 25, 26, 27]. The results of such electron-photon coincidence experiments yield stringent tests for theoretical predictions of the fully differential cross section of the process. The e-n bremsstrahlung has been the subject of several reviews (*see for example* [18] *for a recent review; for an early review see* [32]).

2.1.1 Classical Considerations on the e-n Bremsstrahlung Process

From the classical point of view, e-n Bremsstrahlung is generated when a high-speed incoming free electron with initial kinetic energy $E_\circ$ interacts with the Coulomb field of the nucleus of a target atom. As a result, the electron undergoes a significant deflection in angle and slows down, losing kinetic energy. The energy lost by the incident electron is converted into a photon of electromagnetic radiation (*figure* 2.1). The energy lost by the incoming electron ranges from small fractions of $E_\circ$ up to its total initial kinetic energy $E_\circ$. Similarly, the emitted photon may have any amount of energy up to the total kinetic energy of the incoming electron. According to energy conservation this process is situated along a straight line

$$E = E_\circ - E_\gamma \tag{2.1}$$

in a E, E_γ graph. Here, E and E_γ are the outgoing electron and photon energies respectively; the recoil energy of the nucleus is negligible due to its large mass.

The collision time is considered to be the time interval τ during which significant acceleration occurs. Significant acceleration occurs only when the electron experiences appreciable strength of the target nucleus Coulomb field. A measure of the time interval over which the Coulomb field of the target nucleus seen by the electron is appreciable is [33]

$$\tau \simeq \frac{b}{\gamma v} \tag{2.2}$$

where b is the impact parameter, v is the electron velocity, and γ is the relativistic factor $(1/\sqrt{1-\beta^2})$. The intensity I of radiation emitted by the electron during the collision can be expressed as (*equation* 15.1 *of Jackson* [33])

$$\frac{d^2I}{d\omega d\Omega} = \frac{e^2}{4\pi^2 c} \mid \int \frac{d}{dt}[\frac{\mathbf{n}\times(\mathbf{n}\times\mathbf{B})}{1-\mathbf{n}\cdot\mathbf{B}}]e^{i\omega(t-\frac{\mathbf{n}\cdot\mathbf{r}(t)}{c})}dt \mid^2 \tag{2.3}$$

where ω is the emitted radiation frequency. The radiation emitted by the incident electron will be appreciable only when the phase

$$\Phi(t) \sim \omega(t - \frac{\mathbf{n}\cdot r(t)}{c}) \tag{2.4}$$

of the integrand changes relatively little during the collision. For non-relativistic collisions ($\gamma \simeq 1, \beta << 1$), this leads to a relation between the emitted radiation frequency ω and the collision time τ that must be satisfied if there is to be significant radiation given by [33]

$$\omega\tau < 1 \tag{2.5}$$

while at higher frequencies ($\omega\tau > 1$) the radiation intensity will fall rapidly to zero.

The initial momentum $\mathbf{P}_\circ$ of the incident electron is shared after the collision between three particles, the outgoing electron, $\mathbf{P}$, the emitted photon, $\mathbf{k}$, and the recoil nucleus, $\mathbf{q}$.

$$\mathbf{P}_\circ = \mathbf{P} + \mathbf{k} + \mathbf{q} \tag{2.6}$$

Due to its large mass the nucleus can take any recoil momentum, so that for a fixed momentum of the outgoing electron the photon can be emitted in any direction and similarly for a fixed momentum of the emitted photon the outgoing electron can be scattered in any direction. Mathematically, the equation of momentum conservation, equation 2.6, puts no restrictions on the directions of emission of photons and directions of scattering of electrons; this is not in agreement with experimental findings. Electron-photon coincidence experiments for electron-nucleus bremsstrahlung were conducted by several

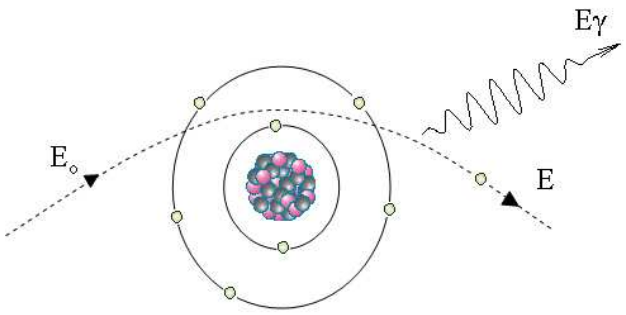

Figure 2.1: Schematic of the elementary process of e-n bremsstrahlung.

groups [27, 34, 35]. In all these experiments, coincident photon and electron angular distributions were reported. It was proved that there is a strong angular correlation with the photons emitted predominantly on the same side as the decelerated outgoing electrons relative to the primary beam. At extreme relativistic energies both the photon and the outgoing electron tend to proceed in the same direction as the incident electron [15]. This behavior can be understood classically by considering the radiation patterns of the electron along its hyperbolic orbit around the nucleus. In this situation the electron is in instantaneously circular motion with its acceleration perpendicular to its velocity (*figure* 2.2). The motion of the electron can be determined precisely from the classical dynamics. The intensity, the spectrum, and the angular distribution of the radiation of the electron can then be related directly to the properties of its trajectory and motion by classical electrodynamics where the instantaneous emitted energy flux is given by the Poynting vector, i.e. energy flow per unit area per unit time. The general formula for the classical angular distribution of the radiated power is given by (*equation* 14.44 *of Jackson* [33]):

$$\frac{dP}{d\Omega} = \frac{e^2}{4\pi c^3}\frac{a^2}{(1-\beta\cos\theta)^3}[1-\frac{\sin^2\theta\cos^2\phi}{\gamma^2(1-\beta\cos\theta)^2}] \tag{2.7}$$

where $\frac{dP}{d\Omega}$ is the power radiated per solid angle, e is the electron charge, c is the speed of light, a is the acceleration of the electron, β is the speed of the electron in units of the speed of light, $\gamma = 1/\sqrt{1-\beta^2}$ is the relativistic factor, θ and ϕ are the customary polar angles defining the direction of observation $\mathbf{n}_\gamma$ with the coordinate system chosen such that instantaneously β is in the z

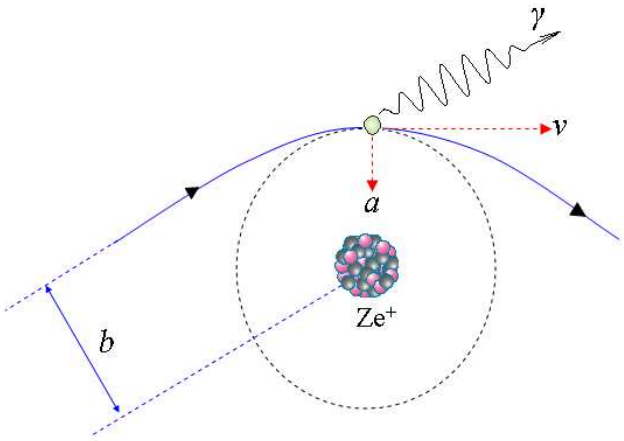

Figure 2.2: Classical hyperbolic orbit of the electron around the nucleus.

direction and a is in the x direction, as shown in figure 2.3.

In the above formula, the emitted power is proportional to the square of the acceleration of the electron ($\frac{dP}{d\Omega} \propto a^2$), which means inversely proportional to the impact parameter b ($\frac{dP}{d\Omega} \propto b^{-4}$), this leads to the conclusion that at the smallest distance from the nucleus the interaction between the electron and the nucleus is strongest and the radiation is strongest. On the other hand, at large impact parameters when the electron passes far away from the nucleus, the acceleration becomes negligible and as a result no radiation is emitted.

Qualitative patterns for the velocity dependence of the angular distribution of the radiated power to be expected from electrons at low and relativistic velocities according to equation (2.7) are shown in figure (2.4). At low electron velocities, there is a symmetric broad distribution with the direction of acceleration as the symmetry axis. At higher electron velocities, the distribution is no longer symmetric and becomes increasingly forward peaked for increasing incident velocity.

The radiation cross section was investigated from a quasi-classical point of view by Kim and Pratt [36]. They have pointed out that the radiation spectrum generated from a certain trajectory of an incident electron in a central potential can be obtained by taking the Fourier transform of the dipole moment

$$\mathbf{d}(t) = -e\mathbf{r}(t) \tag{2.8}$$

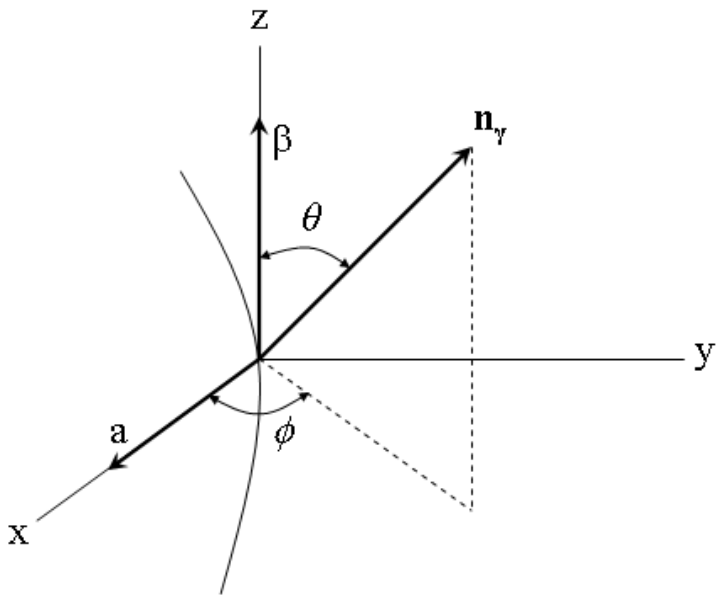

Figure 2.3: Coordinate system chosen in describing the classical angular distribution of e-n bremsstrahlung in equation 2.7. $\mathbf{n}_\gamma$ is the direction of observation.

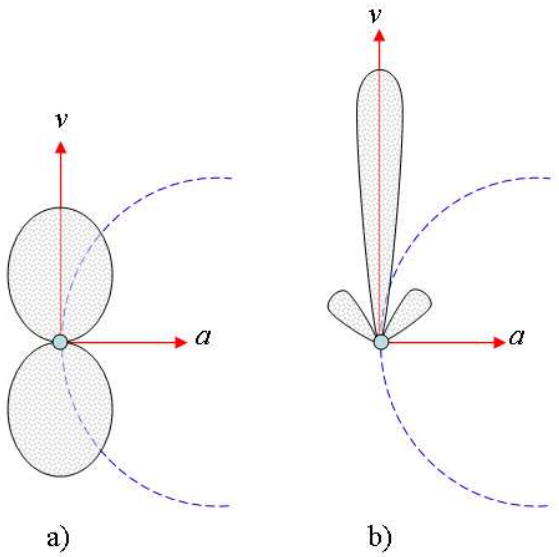

Figure 2.4: Qualitative radiation patterns to be expected from electrons (a) at low velocities (b) at relativistic velocities [18].

of the electron on that trajectory, defined as

$$\mathbf{d}_f(t) = \int_{-\infty}^{\infty} \mathbf{d}(t) e^{i\omega t} dt \tag{2.9}$$

where ω is the frequency of the radiation. The total radiation spectrum is then obtained by integrating the spectrum of a single trajectory over all trajectories, i.e. all different impact parameters of electrons. The resulting photon frequency spectrum (*shown in figure* 2.5) in this case tends to an asymptotic value and unphysically extends to infinity.

Finally, it should be noted that the classical theory of e-n bremsstrahlung fails to predict some quantum mechanical aspects of radiation such as the existence of the high frequency cutoff of the radiation spectrum, for details see the next section 2.1.2.

2.1.2 Quantum Mechanical Considerations on the e-n Bremsstrahlung Process

The classical theory of bremsstrahlung predicts the emission of radiation in every collision in which the electron undergoes changes in its velocity in magnitude or direction. However, the quantum mechanical point of view of e-n bremsstrahlung is quit different. Quantum mechanically, most of the collisions of the incident electrons with the target nucleus are elastic. Therefore, when the electron is scattered from the nucleus there is only a small but finite probability that a photon of finite energy will be emitted: according to quantum electrodynamics each electron is surrounded by a cloud of virtual photons and it will shake off a photon only under rare conditions as for instance in the collision with an atomic nucleus. Because the radiation process involve the coupling of the electron with the electromagnetic field of the emitted photon, the probability that the scattered electron will radiate is of the order of the fine structure constant $\alpha \approx 1/137$. Therefore the cross section for bremsstrahlung is of the order of α times the cross section for elastic scattering [18].

It deserves attention that all experimental findings concerning e-n bremsstrahlung are in good agreement with the results of the quantum theory whereas most features of the bremsstrahlung spectrum cannot be described classically.

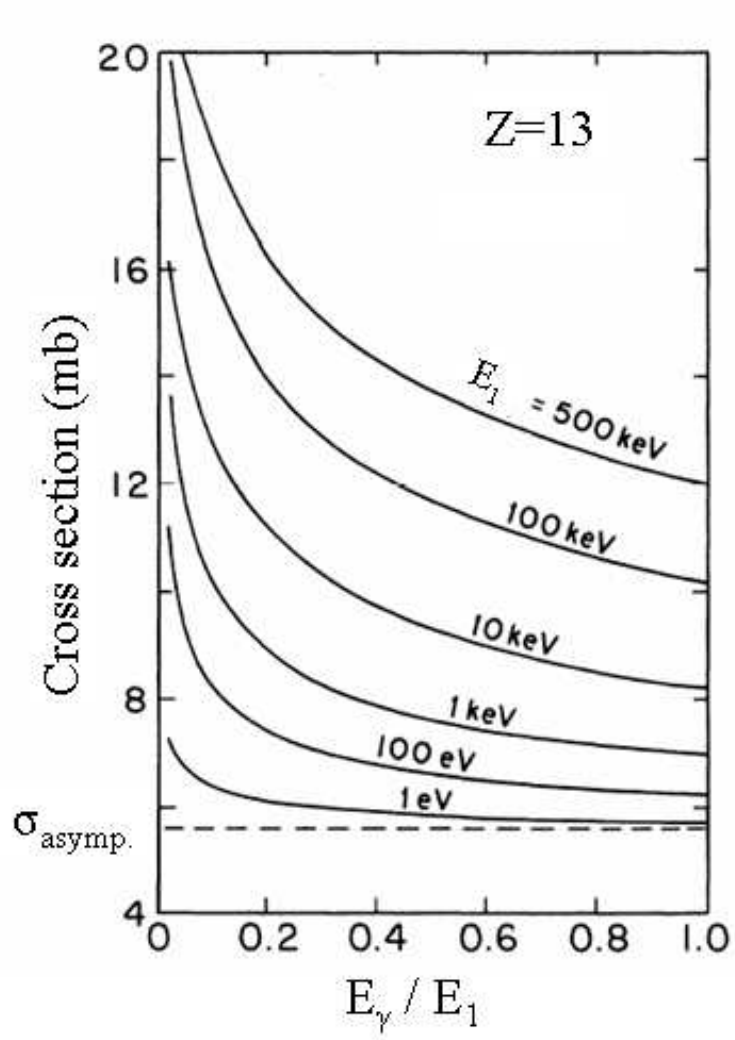

Figure 2.5: Classical spectra for e-n Bremsstrahlung radiation from a point Coulomb potential for electron energies from 1 eV to 500 keV. Cross sections are obtained by taking the Fourier transform of the dipole moment of the electron and integrating the radiation over all possible impact parameters. The resulting spectra tend to an asymptotic value σ_{asymp} and extends to infinity. Figure adapted from Kim and Pratt [36] .

Bremsstrahlung Cross Section

In this entire section we follow the discussions given in the textbook of Haug and Nakel [18] and the review article of W. Nakel [15]. For an electron to emit one photon of energy $h\nu$ and momentum $\mathbf{k}$ and the electron transition from an initial state ψ_1 to a final state ψ_2 the matrix element has the form [18]

$$M_{1\to 2} = -\frac{e\hbar c}{\sqrt{2\epsilon_\circ h\nu L^3}} \int \psi_2^\star(\mathbf{r})(\overrightarrow{\alpha}.\mathbf{e}^\star)e^{-i\mathbf{k}.\mathbf{r}}\psi_1(\mathbf{r})d^3r \tag{2.10}$$

where $\epsilon_\circ$ is the permitivity of vacuum and the unit vector $\mathbf{e}$ gives the direction of polarization of the emitted photon which is always perpendicular to the wave vector $\mathbf{k}$, i.e. $\mathbf{e}.\mathbf{k} = 0$.

According to time-dependent perturbation theory the transition rate from the state $|i\rangle$ of a quantum mechanical system to a set of continuous final states $|f\rangle$ is given in the first order by

$$W_{i\to f} = \frac{2\pi}{\hbar}|\langle i|V|f\rangle|^2\rho_f \tag{2.11}$$

where V is the perturbation defining the interaction of the eigenstates $|i\rangle$ and $|f\rangle$ of the unperturbed Hamiltonian and ρ_f is the number of final states per energy interval dE_f. In the final state of the bremsstrahlung process there is a photon with momentum $\mathbf{k}$ and an electron with momentum $\mathbf{p}$ and energy E. In this case the density of the final state ρ_f is equal to the product of the density functions ρ_k and ρ_p for the photon and electron respectively and can be written as [18]

$$\rho_f = \frac{p(E + m_ec^2)k^2\ d\Omega_p d\Omega_k dk}{(2\pi m_e)^6c^8} \tag{2.12}$$

where $d\Omega_p$ and $d\Omega_k$ are the elements of solid angle in the direction of $\mathbf{p}$ and $\mathbf{k}$, respectively.

The cross section of a process is defined as the number of interactions per unit time per unit flux of the incident particles. Dividing $W_{i\to f}$ by the incident electron flux, i.e. the current density in a cube of side L,

$$J = \frac{v}{L^3} = \frac{1}{L^3}\frac{p_\circ c^2}{E_\circ + m_ec^2} \tag{2.13}$$

and inserting equations (2.10) and (2.12), we can obtain the differential cross section for the elementary process of e-n bremsstrahlung given by

$$\frac{d^3\sigma_{e-n}}{dkd\Omega_k d\Omega_p} = \frac{\alpha}{(2\pi)^4}(\frac{\hbar}{m_e c})^2 \frac{p(E_\circ + m_e c^2)(E + m_e c^2)k^2}{m_e^4 c^5 p_\circ (h\nu)}|M|^2 \tag{2.14}$$

where $\alpha = e^2/(4\pi\epsilon_\circ \hbar c) \approx 1/137$ is the fine-structure constant, and

$$M = \int \psi_2^\star(\mathbf{r})(\overrightarrow{\alpha}.\mathbf{e}^\star)e^{-i\mathbf{k}.\mathbf{r}}\psi_1(\mathbf{r})d^3r \tag{2.15}$$

is the matrix element (2.10) without the factor before the integral. Using $k = h\nu$ and denoting the total electron energy including rest mass energy by ε ($\varepsilon = E + m_e c^2$) lead to the final formula for the differential cross section for the elementary process of e-n bremsstrahlung given by

$$\frac{d^3\sigma_{e-n}}{dkd\Omega_k d\Omega_p} = \frac{\alpha}{(2\pi)^4}\frac{\varepsilon_\circ \varepsilon p k}{m_e^4 c^5 p_\circ}(\frac{\hbar}{m_e c})^2|M|^2 \tag{2.16}$$

Theoretical predictions of the process of e-n bremsstrahlung require calculations of the probability that the incident electron will make a transition to a different electronic continuum state with a photon emitted while in the Coulomb field of the atom whose internal state remains unchanged

$$electron + atom \rightarrow electron + photon + atom(unchanged).$$

The interaction causing the transition consists of two parts: the interaction of the electron with the radiation field giving rise to the emission of the photon, and the interaction of the electron with the screened nuclear Coulomb field. Whereas the interaction of electrons with the radiation field can be treated only by perturbation theory, their interaction with the atomic field can, in principle, be handled exactly. For that, exact solutions of the Dirac wave equation

$$\{-i\overrightarrow{\alpha}.\nabla + \beta - \epsilon - \frac{\alpha Z}{r}\}\psi(\mathbf{r}) = 0 \tag{2.17}$$

are required. It is, however, not possible to solve the Dirac wave equation in closed form for a free electron in a screened nuclear field. Therefore either approximate analytic solutions or numerical methods have to be used to obtain the triply differential cross section for e-n bremsstrahlung. The simplest method is the Born approximation where one expands the wave function $\psi(\mathbf{r})$ of an electron scattered in the Coulomb potential of a point charge (Ze) as a function of the coupling to the external field (αZ)

$$\psi = \psi_\circ + (\alpha Z)\psi_1 + (\alpha Z)^2\psi_2 + ... \tag{2.18}$$

where α is the fine structure constant, $\psi_\circ$ is the solution of the force free zeroth order Dirac equation

$$\{-i\overrightarrow{\alpha}.\nabla + \beta - \epsilon\}\psi_\circ(\mathbf{r}) = 0 \tag{2.19}$$

with the plane wave solution

$$\psi_\circ(\mathbf{r}) = e^{i\mathbf{p}.\mathbf{r}}u(\mathbf{p}) \tag{2.20}$$

where $u(\mathbf{p})$ is the free-electron spinor. Higher order terms of equation (2.18) characterize the distortion by the potential with which the wave interacts. The basic assumption of the **first Born approximation** is that if the product (αZ) is small compared to unity only the first term $\psi_\circ(\mathbf{r})$ of equation (2.18) needs to be kept. The physical meaning of this assumption is that the incident and outgoing waves are only weakly deformed from a plane wave by the nuclear potential with which the electron interacts. The Born approximation only gives correct results if the de Broglie wavelength of the electron, $\hbar/m_e v$, is large compared with the size d of the Coulomb field given by $Ze^2/(4\pi\epsilon_\circ d) \approx m_e v^2$ [18]. Therefore the condition for validity is

$$\frac{\alpha Z}{\beta_\circ} << 1 \qquad \text{and} \qquad \frac{\alpha Z}{\beta} << 1 \tag{2.21}$$

where $\beta_\circ$ and β are the electron velocities in units of the velocity of light c before and after being scattered respectively. The calculation of bremsstrahlung with first Born approximation was first done by Bethe and Heitler [37]; it yields for the triply differential cross section [15]

$$
\begin{aligned}
d\sigma_{e-n} =& \frac{Z^2 e^4}{2\pi\alpha}\frac{dk}{k}\frac{p}{p_\circ}\frac{\sin\theta\sin\theta_\circ d\theta d\theta_\circ d\phi}{q^4}\{\frac{p^2\sin^2\theta}{(E-p\cos\theta)^2}(4E_\circ^2-q^2) \\
&+\frac{p_\circ^2\sin^2\theta_\circ}{(E_\circ-p_\circ\cos\theta_\circ)^2}(4E^2-q^2)-\frac{2pp_\circ\sin\theta\sin\theta_\circ\cos\phi}{(E-p\cos\theta)(E_\circ-p_\circ\cos\theta_\circ)}(4EE_\circ-q^2) \\
&+\frac{2k^2(p^2\sin^2\theta+P_\circ^2\sin^2\theta_\circ-2pp_\circ\sin\theta\sin\theta_\circ\cos\phi)}{(E-p\cos\theta)(E_\circ-p_\circ\cos\theta\circ)}\}
\end{aligned}
\tag{2.22}
$$

where Z is the target-nucleus atomic number, e is the electronic charge, $p_\circ, p$ are the momenta of the incident and outgoing electron respectively, $E_\circ, E$ are the kinetic energies of the incident and outgoing electron respectively, k is the momentum of the emitted photon, $\theta, \theta_\circ$ are the angles between $\mathbf{k}$ and $\mathbf{p}, \mathbf{p}_\circ$ respectively, ϕ is the angle between the ($\mathbf{pk}$) plane and the ($\mathbf{p}_\circ\mathbf{k}$) plane (*figure* 2.6), and $\mathbf{q} = \mathbf{p}_\circ - \mathbf{p} - \mathbf{k}$ represents the total momentum transferred to the target nucleus. This is the famous Bethe—Heitler formula. It is averaged over the spins of the incident electron and summed over the spins of the outgoing electron and the polarization directions of the photon. One of the noticeable consequences of the Bethe—Heitler formula is the prediction of a gradual decrease in photon yields as a function of the photon energy (*figure* 2.7). The formula fails to predict a non-zero doubly differential cross sections at the tip of the photon spectrum (*see section* 2.1.2). This is a consequence of the fact that high energy photons arise from collisions where the final electron velocity is close to zero. Here, the condition of validity of the first Born approximation ($\alpha Z/\beta << 1$) is not satisfied.

As an example of electron and photon coincident angular distributions, the quantum mechanical angular distribution of e-n bremsstrahlung was predicted theoretically in the calculations of Elwert and Haug [38] for 300 keV electrons incident on aluminum ($Z = 13$) target and outgoing electron energy of 100 keV. The resulting angular distributions are presented in figure (2.8). The left part represents the photon angular distributions for fixed electron scattering angles ($0°, 8°, 15°, 30°$) and shows clearly the increase of asymmetry in the photon angular distribution and the vanishing of the minimum between the two lobes with increasing electron scattering angle. The right part represents the electron angular distributions for fixed photon emission angles ($0°, 4°, 8°, 16°$)

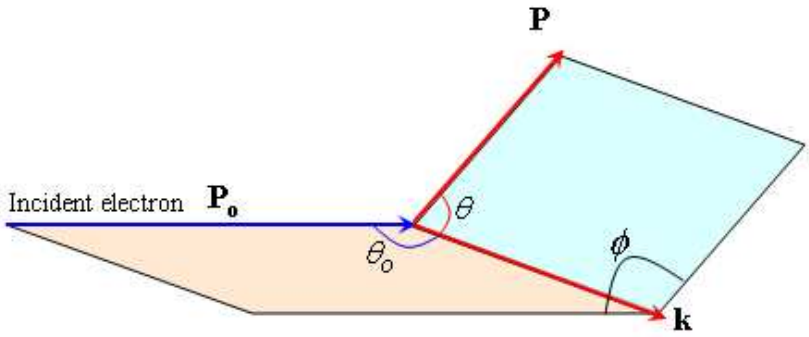

Figure 2.6: Geometric relative location of different momenta and angles used in the Bethe-Heitler formula.

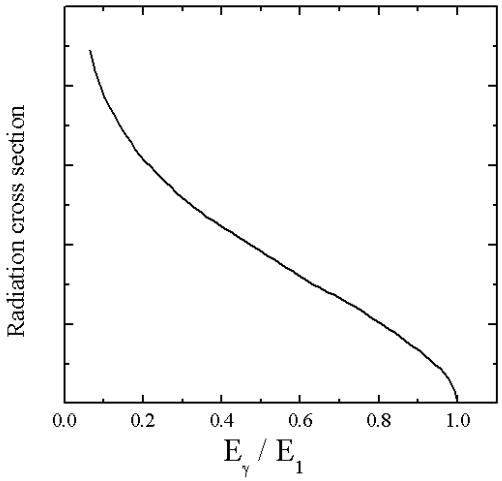

Figure 2.7: Relative differential cross section for classical e-n bremsstrahlung as function of the emitted photon energy E_γ in units of the energy of the incident electron E_1 calculated using the Bethe-Heitler formula. The classical spectrum emphasizes the very low photon energies and decreases gradually to zero at the end point of the spectrum. Figure adapted from Jackson [33].

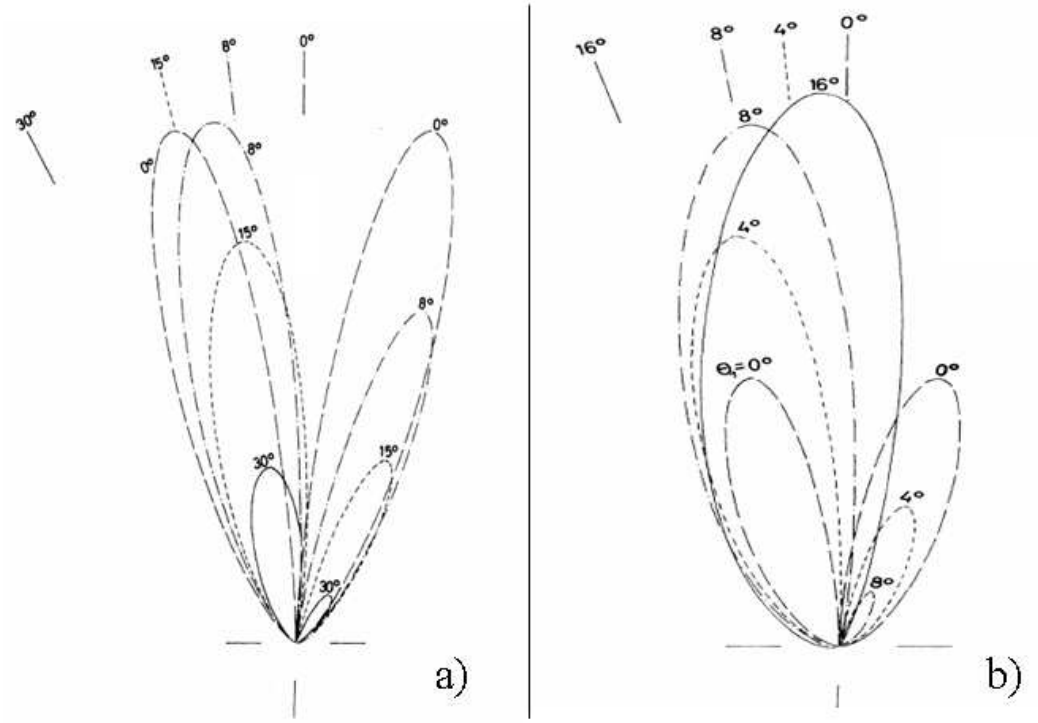

Figure 2.8: Theoretical photon angular distributions (left side) for various electron scattering angles $(0°, 8°, 15°, 30°)$ and the corresponding electron angular distributions (right side) for various photon emission angles $(0°, 4°, 8°, 16°)$ resulting from 300 keV electrons incident on aluminum ($Z = 13$) targets and outgoing electron energy of 100 keV. Figure adapted from [38].

and shows the same behavior as that for photons.

Short Wavelength Limit (SWL) of e-n Bremsstrahlung

Quantum mechanical treatment of e-n bremsstrahlung shows also that the radiation process has a finite cross section at the short-wavelength limit which appear as a sharp cut-off at the high frequency limit of the radiation spectrum (*figure* 2.9) which can not be described classically. This behavior has been observed in the experimentally measured x-ray spectra in many works in the last three decades [39, 40, 41].

In an e-n bremsstrahlung event, energy conservation

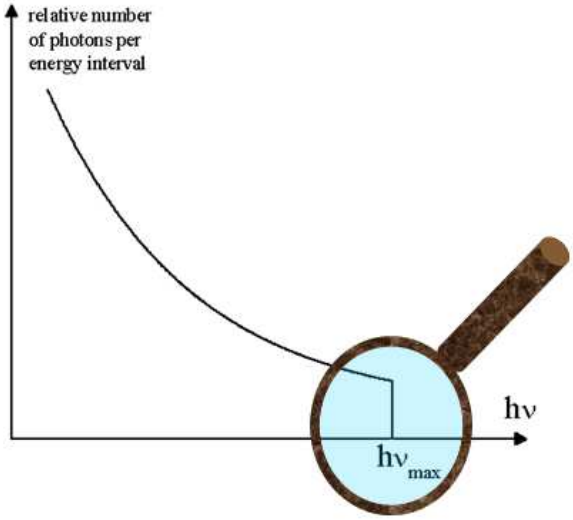

Figure 2.9: The photon frequency spectrum showing that the spectrum cuts off sharply at the maximum photon energy, $h\nu_{max}$ [18].

$$E_\circ = E + h\nu \tag{2.23}$$

implies that the maximum energy of any one of the emitted photons cannot be greater than the kinetic energy $E_\circ$ of the incident electron ($h\nu \leq E_\circ$):

$$h\nu_{max} = \frac{hc}{\lambda_{swl}} = E_\circ \tag{2.24}$$

where h is Planck's constant, c is the speed of light, and λ_{swl} is the shortest wavelength of the emitted photon. The photon of highest energy will be emitted when an incident electron loses its entire kinetic energy in one deceleration process to a photon of electromagnetic radiation and ends up with virtually zero momentum [38]. This shows that the very existence of a high frequency limit is a quantum phenomenon. In the rest frame of the nucleus, the photon will possess the energy of the incident electron $(\gamma - 1)mc^2$ but will appear in the rest frame of the electron with maximum energy given by

$$E_{swl} = \frac{(\gamma - 1)mc^2}{\gamma(1 - \beta\cos\theta_{lab})} \tag{2.25}$$

which, in the present case, for 90 MeV/u $U^{88+} + N_2$ at 90° equals to 45.02 keV.

The condition of validity of the first Born approximation (*equation* 2.21) is satisfied for low atomic number elements if the electron energies are relativistic ($\beta_\circ$ *and* $\beta \approx 1$) since the fine structure constant $\alpha \approx 1/137$ is a small quantity. But even for initially energetic electrons the second constraint is violated near the short wavelength limit where the electron final velocity $\beta << 1$. In this case, the distortion of the electron wave function by the nuclear Coulomb field (*higer order terms of equation* 2.18) should be taken into account and the cross section does not vanish for $p \rightarrow 0$. It is now easy to understand why the Bethe-Heitler cross section tends to zero in the limit $p \rightarrow 0$. According to equations (2.18) and (2.20) the final electron in the first Born approximation is described by a plane wave for which the matrix element M remains finite as $p \rightarrow 0$. The cross section is proportional to $p|M|^2$ (*see equation* 2.16) so that the cross section vanishes with p. By contrast, when a coulomb correction (*distortion of the electron wave function*) is included, the exact point-Coulomb wave functions (*equations* 3.314 *and* 3.315 *of* Haug *and* Nakel [18]) do not remain finite in the limit $p \rightarrow 0$ but diverges as $p^{-1/2}$ thus leading to a finite cross section at the short wavelength limit. The divergence of the exact wave function for small values of p is a consequence of the long-range nature of the point-Coulomb potential. If the potential is cut off at some distance the wave function will be finite as $p \rightarrow 0$.

Physically, the finite bremsstrahlung cross section at the tip of the spectrum is related with the fact that the photon energy $h\nu = E_\circ$ is a limit only for the free-free transitions. If the electron is captured into a bound state it can emit a photon of energy $h\nu > E_\circ$. Highly excited bound (*Rydberg*) states are similar to free states at low kinetic energies. Hence there is a relationship between the high-frequency endpoint region of bremsstrahlung and recombination radiation [42]: The matrix element for radiative recombination, involving a final negative binding energy state may be analytically continued to the corresponding bremsstrahlung matrix element involving a positive kinetic energy final state. The short wavelength limit has been at the focus of theoretical attention because of this deep relation with the radiative recombination, i.e.

the time-reversed photoionization process (*details in section* 2.1.3). Moreover, it is well established that hard-photon bremsstrahlung is closely related to the radiative electron capture to continuum (*details in section* 2.3).

The calculated bremsstrahlung cross section at the short wavelength limit is reported [18, 38] to be proportional to the third power of the atomic number Z ($d\sigma \propto Z^3$). Hence, the relative strength of the high energy end of the bremsstrahlung spectrum increases for targets of high atomic number. It is also interesting to note that the cross section for e-n bremsstrahlung at the short wavelength limit depends on the direction of the outgoing electron [43]. This means that although the outgoing electrons have virtually zero velocity, their angular distribution is still correlated to the direction of emission of photons (*figure* 2.10).

Measurements of the differential cross section for e-n bremsstrahlung at the upper end of the x-ray frequency spectrum have never been accomplished in the standard experimental techniques which requires a coincidence between a photon and an outgoing electron which in turn means the detection of an electron that lost its entire energy and does not leave the target. in most Bremsstrahlung experiments, solid targets are used or electrons are detected using solid state detectors which restricts the outgoing electron energy to a minimum value in the range of 100 keV. As a result, these experiments are by design not able to test the short wavelength limit or the relationship between the bremsstrahlung theory and the relativistic theory of photoionization.

2.1.3 Bremsstrahlung and Photoeffect

As has been discussed, in contrast to the Born approximation prediction of the Bethe-Heitler formula, the bremsstrahlung remains finite in the high frequency limit, when the photon energy achieves its maximum value. Fano *et a*l [44] and McVoy *et al* [45] have reported that, in this limit bremsstrahlung is an approximate inverse of the atomic photoelectric effect in which a bound atomic electron is ionized by the absorbtion of a photon. The relationship of the high frequency limit of bremsstrahlung and photoeffect is apparent in a comparison of matrix elements. The matrix element for the case in which an electron in a free state ψ_1 radiate a photon of momentum $\mathbf{k}$ and polarization $\mathbf{e}$, thereby

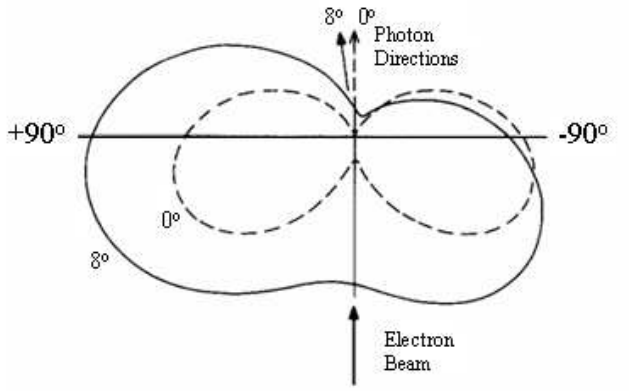

Figure 2.10: Calculated angular distribution of decelerated outgoing electrons for fixed photon directions (0° *and* 8°) at the short-wavelength limit. Incident electron energy 300 keV and atomic number Z = 13. Figure adapted from [43]

going into a final continuum state ψ_2 can be written as [38, 46]

$$M_{brems} = \int \psi_2^{\star}(\overrightarrow{\alpha}.\mathbf{e}^{\star})e^{-i\mathbf{k}.\mathbf{r}}\psi_1 d^3r \tag{2.26}$$

where $\overrightarrow{\alpha}$ is the Dirac operator and $\mathbf{r}$ is the electron coordinate. The matrix element for the case in which an electron in a bound state ψ_1 absorbs a photon of momentum $\mathbf{k}$ and polarization $\mathbf{e}$, thereby going into a final free state ψ_2 can be written as [46]

$$M_{photo} = \int \psi_2^{\star}(\overrightarrow{\alpha}.\mathbf{e})e^{i\mathbf{k}.\mathbf{r}}\psi_1 d^3r \tag{2.27}$$

and its complex conjugate is

$$M_{photo}^{\star} = \int \psi_1^{\star}(\overrightarrow{\alpha}.\mathbf{e}^{\star})e^{-i\mathbf{k}.\mathbf{r}}\psi_2 d^3r \tag{2.28}$$

The difference between the matrix elements for the short wavelength of e-n bremsstrahlung in 2.26 and that for the photoeffect in 2.28 is the replacement of a continuum wave function by a bound-state wave function. Pratt [46] and Fano [44] have noted when a wave function of a bound atomic electron with quantum numbers n, l, j, goes over at the limit $n\rightarrow \infty$ into a continuum-electron wave function with the same quantum numbers l and j, this limit is

approached rapidly by the values of the wave function near the nucleus (*for small r*), which alone are relevant, at relativistic energies, to the photoeffect or to the emission of bremsstrahlung at the high frequency limit. The screening action of atomic electrons differs in the photoeffect and bremsstrahlung processes, but this difference should be very small near the nucleus. Of course, the similarity between bound and continuum wave functions implies a similarity between the matrix elements for inverse photoeffect and the high frequency limit of e-n bremsstrahlung if the major contribution to the integrals over wave functions which determines the matrix elements comes from the region where the wave functions agree in lowest order matrix elements.

However, a measurement of the short wavelength limit of e-n bremsstrahlung is crucial to support the theoretical claim of the presence of such a correspondence. Any difference in the experimental total differential cross sections of the short wavelength limit of e-n bremsstrahlung and photoionization would hint at deficiency of the underlying theoretical description. If this equivalence between the short wavelength limit of e-n bremsstrahlung and the photoionization is experimentally proved to exist, It has a practical consequence that theoretical predictions for the cross section of the high frequency limit of e-n bremsstrahlung follow from the theoretical work on the photoionization. This provides a mean of investigating theoretically the bremsstrahlung process at the spectrum limit, where the usual Born approximation breaks down completely [44, 47].

2.1.4 Bremsstrahlung in Ion Atom Collisions

Besides characteristic target and projectile x-ray lines, x-ray spectra generated in ion atom collisions [39, 40, 41] contain a large low-energy continuum. In early experiments using light projectiles [48, 49] this continuum was thought to be due to γ-ray production in nuclear reactions [50]. When experiments were extended to the use of relativistic heavy ions, it became obvious that the continuum x-ray production cross sections were too large (*as large as* 100 *barn/KeV at some x-ray energies*) to be due to nuclear reactions. A nuclear reaction requires a close projectile target-nucleus encounter whose geometric cross section rarely exceeds a few barns, even for heaviest projectiles. There-

fore, nuclear reactions cannot produce γ-rays with such large cross section and the continuum must be due to atomic physics phenomena. However, this continuum was found [39, 40, 51] to be well explained in terms of bremsstrahlung radiation. Here, the predominant source of bremsstrahlung accompanying ion atom collisions is mainly the quasifree inelastic scattering of an initially bound target electron in the field of the projectile nucleus. For not too heavy targets, the Impulse approximation [52] can be adapted. The impulse approximation consists of three basic assumptions. In the case of a single particle incident upon a complex target system consisting of two or more particles bound together they are [53, 54]: (1) The range of interaction is small compared with the inter-particle distances, so that the incident particle interacts with only one particle of the target system during the collision. (2) The target system can be regarded as transparent, so that the amplitude of the incident particle is not appreciably diminished in crossing the target system. This is to say that the near particles of the target system do not cast shadows on the far ones. (3) The interaction occurs over such a short time that the effect of the binding forces during the collision may be neglected, if the velocity of the projectile is large enough in comparison with the velocity of the orbital electron, the bound electron can be considered free and at rest [40]. We thus think of the scattering as taking place from only one quasifree electron of the target system. The only part played by the initial state of the target system is to give a momentum distribution to the electrons of the target system. Radiation emitted in this collision process is called the quasifree-electron bremsstrahlung (QFEB). The production cross section of the QFEB based on the first born approximation is expressed by [55]

$$\begin{aligned}\frac{d\sigma_{_{QFEB}}}{dE_\gamma d\Omega} =& \frac{N_t}{\pi} Z_p^2 (\frac{e^2}{\hbar c})^5 a_\circ^2 \frac{m_e c^2}{E_\circ E_\gamma} \\ & \times [\sin^2\theta + \frac{1}{4}(1+p^2)(3\cos^2\theta - 1)\ln(\frac{1+p}{1-p}) - \frac{1}{2}p(3\cos^2\theta - 1)]\end{aligned} \tag{2.29}$$

where $p^2 = 1 - E_\gamma/E_\circ$, N_t is the number of electrons of the target atom, Z_p is the atomic number of the projectile, $a_\circ$ is the Bohr radius, m_e is the electron mass, e is the electron charge, c is the speed of light, $\hbar$ is the reduced Planck

constant , $E_\circ$ is the energy of an electron moving with the projectile velocity, E_γ is the energy of the emitted photon, and θ is the angle between the direction of the projectile and the photon.

It is to be noted that, for a fixed projectile velocity the cross section for production of a bremsstrahlung photon increases as Z_p^2. Apart from the scaling factor Z_p^2, the shape of the bremsstrahlung spectrum is independent of the choice of the projectile. A formula of QFEB for the case where the velocity of the orbital target electron is not negligible in comparison with the projectile velocity (*the velocity distribution of the orbital target electrons is taken into account*) has been given by Jakubaßa and Kleber [51] on the basis of the first Born approximation. The QFEB spectra were calculated [40] for the two cases for 20 MeV protons incident on Be and Al targets where it was apparent that the two calculations yield similar results for the Be target but rather different results for the Al target. This fact reveals that QFEB spectrum becomes increasingly dependent on the velocity distribution of the orbital target electrons as the target atomic number increases. It was also noted that the intensity decline near the short wavelength limit becomes less steep for higher target atomic numbers.

Since the QFEB is produced in the rest frame of the projectile, a Doppler shift in the emitted photon energy is expected; the observed photon energy E_{lab} is related to the projectile-frame energy $E_{emitter}$ by [56]:

$$E_{lab} = \frac{E_{emitter}}{\gamma(1 - \beta \cos\theta_{lab})} \tag{2.30}$$

where θ_{lab} denotes the laboratory observation angle ($90°$*in this work*), β is the speed in units of the speed of light and γ is the relativistic Lorentz factor $\frac{1}{\sqrt{1-\beta^2}}$. This Doppler shift becomes larger for high-energy projectiles; with 90 MeV/u $U^{88+} + N_2$, the photon energy decreased by 9% at $90°$ (*see chapter* 4)

Within the impulse approximation assumptions, the differential cross section for bremsstrahlung accompanying ion atom collisions ($\frac{d^2\sigma_{ion-atom}}{dE_{lab}d\Omega_{lab}}$) can be given by the differential cross section of e-n bremsstrahlung ($\frac{d^2\sigma_{e-n}}{dE_{proj}d\Omega_{proj}}$) caused by a quasifree target electron moving with the projectile speed multiplied by the number of available target electrons [41], Lorentz transformed into the laboratory frame [48]

$$\frac{d^2\sigma_{ion-atom}}{dE_{lab}d\Omega_{lab}} = N_t \frac{d^2\sigma_{e-n}}{dE_{proj}d\Omega_{proj}} \frac{dE_{proj}}{dE_{lab}} \frac{d\Omega_{proj}}{d\Omega_{lab}} \tag{2.31}$$

where

$$\frac{dE_{proj}}{dE_{lab}} = \frac{1-\beta\cos\theta_{lab}}{\sqrt{1-\beta^2}} \tag{2.32}$$

and

$$\frac{d\Omega_{proj}}{d\Omega_{lab}} = \frac{1-\beta^2}{(1-\beta\cos\theta_{lab})^2} \tag{2.33}$$

which gives

$$\frac{d^2\sigma_{ion-atom}}{dE_{lab}d\Omega_{lab}} = N_t \frac{d^2\sigma_{e-n}}{dE_{proj}d\Omega_{proj}} \frac{\sqrt{1-\beta^2}}{1-\beta\cos\theta_{lab}} \tag{2.34}$$

here, the bremsstrahlung cross section can be given by the Bethe-Heitler formula (*Equation* 2.22) or alternatively can be taken from tables of electron bremsstrahlung cross sections given by Kissel *et al* [57]. Equations (2.25) and (2.34) assume that the target electrons are free and have no intrinsic momentum, and therefore give a sharp cutoff x-ray energy equal to the electron kinetic energy. Disregarding the motion of the atomic electrons can be justified if the target atoms have low atomic numbers Z_t where the electron binding energy is small compared with the kinetic energy of the incoming electrons. When one adds the Compton profile of the target electrons to the translational momentum, larger electron kinetic energies and end point energies are obtainable and the shape of the bremsstrahlung spectrum near its cutoff reflects the momentum distribution of the target electrons.

In the last two decades, the double differential cross section ($d^2\sigma/dEd\Omega$) for e-n bremsstrahlung accompanying ion–atom collisions has been investigated for intermediate projectile energies [40, 51, 58, 59, 60, 61]. In this energy domain the adaptation of the relativistic Born approximation (*section* 2.1.1) together with the impulse approximation generally gives reasonable agreement with the experimental data. The major advantage of ion–atom collisions for the study of bremsstrahlung is that the charge state of the projectile can be easily and selectively varied. In particular, high-Z projectiles are of interest, as they exclusively probe the coupling between the continuum states and the radiation field in the presence of strong external potentials [41].

In ion-atom collisions using thick solid targets, bremsstrahlung is also expected to be generated in a two step process called secondary electron bremsstrahlung

(SEB). In the first step target atoms are ionized via coulomb excitation. The free electrons produced in this step radiate in the field of another target nucleus. The maximum energy which can be transfered from a projectile with velocity v to a free electron with mass m is $2mv^2$ (*see section* 2.4). Sohval *et al* [62] have estimated that for intermediate energy ion–atom collisions the cross section for SEB becomes comparable with the primary bremsstrahlung or the radiative electron capture (REC) cross sections for target densities above 10^{18} particles/cm^2 and expected to become much smaller for lower target densities. In our case using a gaseous N_2 target with density 10^{12} particles/cm^2, the SEB contribution to the observed bremsstrahlung spectrum can be expected to be negligible taking into account the fact that high-energy ($\sim$50–200 keV) secondary electrons produced in such relativistic collisions can pass without much scattering through the N_2 target.

2.2 Electron Transfer to Continuum (Cusp Electrons)

In 1970 Crooks and Rudd [63] have measured the energy spectrum of electrons ejected in the forward direction from helium bombarded by protons. In the resulting spectra they found a cusp shaped peak in the doubly differential cross section ($\frac{d^2\sigma}{dEd\Omega}$) for electron emission close to the direction of the outgoing projectile. The electron cusp appears when the electron velocity vector in the laboratory frame approximately equals the projectile velocity in both magnitude and direction. This behavior was also predicted in the associated theoretical works of Salin[64] and Macek[9]. In the same year Harrison and Lucas [65] observed a similar cusp in the electron distribution ejected by light ions traversing carbon foil targets. In both cases the electron cusp was interpreted as an effect of charge exchange into low-laying continuum states centered around the moving projectile. These electrons are considered to be free electrons (*in contrast to the bound electrons of proper charge exchange*) with very small velocities as seen in the rest frame of the projectile. After these first experiments, the forward electron cusp was detected for various projectiles traversing thin solid and occasionally gaseous targets at projectile energies up

to 1.2 *MeV/u* [66, 67, 68, 69]. Rudd and Macek [2] had already emphasized the close connection between excitation to or capture into a band of high Rydberg states and similar contiuum bands above the ionization limit. As they point out, ejection of slow secondary electrons is a natural continuation of excitation to states of high principal quantum numbers, and that the electron capture process should continue beyond the ionization limit of the atom in a smooth, continuous, and uninterrupted way. Since that time the process of electron transfer to continuum has been investigated with increasing interest, both experimentally and theoretically. This field has been reviewed [4, 70, 71] covering all experimental developments.

The quantity of experimental interest is the differential cross section ($\frac{d^2\sigma}{dv_e d\Omega}$) for the electron to emerge into a narrow forward cone of specific semiangle with a speed v_e close to the speed of the projectile v_{proj}.

For ion-atom collisions under single-collision conditions two different mechanisms for the production of cusp electrons have been isolated [8]: electron loss to the projectile continuum (*projectile ionization*) abbreviated as ELC, and electron capture to the projectile continuum (*target ionization*) abbreviated as (ECC).

2.2.1 Electron Loss to Continuum (ELC)

Electron loss to continuum (ELC) can appear in ion atom collisions when the incident ions carry electrons into the collision (*partially ionized projectiles*). These projectiles may become ionized by the excitation of one or more electrons from an initial bound state of the projectile ion into a low lying continuum state of the projectile itself due to an interaction with either the target nucleus or a target electron (*figure* 2.11). Mostly projectile electrons having orbital velocities less than the velocity of the projectile are ionized, i.e. the ELC cross section is large when the projectile velocity is larger than the orbital velocity of the electron with the lowest binding energy. The resulting ELC electrons, ejected in the moving frame of reference, cause a cusp-shaped peak in the velocity spectrum and exhibit also a preferred longitudinal emission parallel to the beam axis [72, 73]. ELC cusps have been observed in different measurements concerning electron transfer to continuum [2, 74, 75] where it has

been emphasized that the velocity distribution of electrons from the projectile is centered around $v_e \simeq v_p$ (v_p *and* v_e *are the projectile and emitted-electron laboratory velocities respectively*) for all ion angles.

Theoretical discussions [76, 77, 78] of the ELC lead to a cross section which diverges when $v_e \simeq v_p$ and can be written as

$$\frac{d\sigma_{_{ELC}}}{dv'} = F(v_e, v_p, \varphi) f(|v_e - v_p|) \tag{2.35}$$

where $v' = v_e - v_p$, φ is the electron emission angle in the projectile rest frame, $F(v_e, v_p, \varphi)$ is finite near $v_e \simeq v_p$ and describes the yield of the ELC process as a function of v_p, v_e and φ, and $f(|v_e - v_p|)$ describes the divergent factor of the differential ELC cross section in terms of the absolute value of the projectile electron velocity difference. Essentially, all theories [79, 80, 81] agree that to a first approximation

$$f(|v_e - v_p|) \propto \frac{1}{|v_e - v_p|} \tag{2.36}$$

which is symmetric about $v_e = v_p$ and results from the Coulomb interaction between the outgoing projectile and the ejected electron. Thus the observed shape of the ELC cusp must be associated with the function $F(v_e, v_p, \varphi)$. An expansion of $F(v_e, v_p, \varphi)$ in terms of a projectile-frame partial-wave expansion and the inclusion of only the leading terms (*first Born approximation*) serve to put $F(v_e, v_p, \varphi)$ in the form [76, 78, 73]

$$\begin{aligned} F(v_e, v_p, \varphi) &= a_\circ + a_2 P_2(\cos\varphi) \\ &= A[1 + \eta P_2(cos\varphi)] \\ &= A[1 - \frac{\eta}{2} + \frac{3\eta}{2}\cos^2\varphi] \end{aligned} \tag{2.37}$$

where $P_2(x) = \frac{1}{2}(3x^2 - 1)$ is the legendre polynomial, A is a magnitude and η is anisotropy parameter ranging between $-1 \leq \eta \leq 2$. This leads to the final generally accepted form of the ELC differential cross section given by

$$\frac{d\sigma_{_{ELC}}}{dv'} = \frac{A}{|v_e - v_p|}[1 - \frac{\eta}{2} + \frac{3\eta}{2}\cos^2\varphi] \tag{2.38}$$

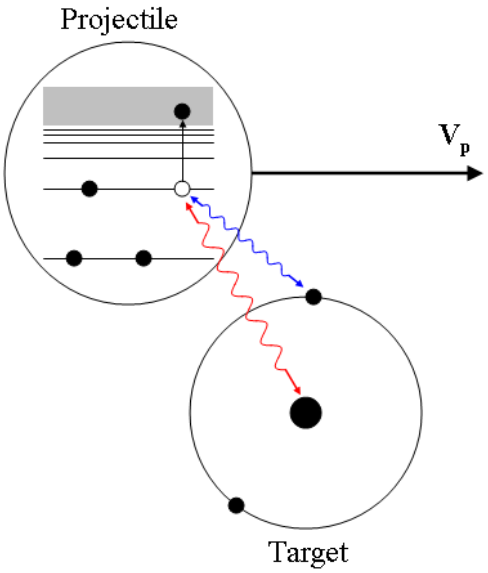

Figure 2.11: Schematic representation of the ELC process.

The character of the ELC distribution changes dramatically with ejection angle. In the forward direction (*around* 0° *with respect to the incident beam direction*) the distribution assumes a cusp-shaped form around $v_e \simeq v_p$ while at higher angles (*greater than* $\sim 25°$) the distribution is still centered around $v_e \simeq v_p$ but reflects the momentum distribution of the projectile bound state occupied by the electrons before the collision. Burch *el al* [75] have shown that the distribution can be well represented by that of free electrons (*with an initial momentum distribution of the projectile bound state*) having scattered elastically from the target atom.

The ELC event is a single step ionization process in which the target atom plays the role of an ionizing projectile in the rest frame of the projectile, and a weak collisional interaction is sufficient to emit electrons into low-lying projectile continuum states. Burgdörfer [8] has pointed out that a soft collision with a small momentum transfer q of the order $q \geq q_{min} \cong \epsilon_i/v_p$ (*where* ϵ_i *denotes the binding energy of the projectile electron to be ionized,* v_{proj} *is the projectile velocity*) is enough to promote an electron from a projectile bound state to a

state at the continuum threshold. The reported cross sections for ELC exhibit q^{-4} dependance [6, 8, 2] which means that electrons are predominantly populate states at the continuum threshold which leads to the nearly symmetric peak. Because of the small momentum transfer required for an ELC event, a first-Born perturbation treatment was considered suitable by Day [79] and Briggs and Day [82] to describe details of the resulting electron distribution. generally, the Born approximation for excitation is believed to be valid in the limit of large projectile velocities [83].

As mentioned previously, the ELC event is a result of the Coulomb interaction between the active projectile electron with the target nucleus (e-N) or with one of the target electrons (e-e). The two different mechanisms can be distinguished according to their different kinematics. If (e-N) interaction leads to the ELC event, the target nucleus plays the active role, whereas the target electrons stay at rest and act as spectators. In this case, the momentum transferred to the target nucleus is expected to be bigger than the one transferred to any target electron. If (e-e) interaction leads to the ELC event, a target electron plays the active role, whereas the target nucleus acts as a spectator. Here, the momentum transferred to the active target electron is expected to be bigger than the one transferred to the target nucleus.

The (e-e) interaction channel leads mainly to ionization of both collision partners, i.e. in the case of ELC caused by (e-e) interaction, simultaneous excitation or ionization of the target electron (*a doubly inelastic process*) is expected to take place. In the case of pure ELC (*the target is not ionized*), electron loss is due essentially to the screened target nucleus (*e-N interaction*) with the target electrons remaining in their ground states [84].

While the (e-N) interaction can occur at all projectile velocities, the (e-e) interaction has a threshold (*for* He^+ *projectile on* He, *this threshold is near* 0.4 MeV, *equivalent to an electron energy of* 54 eV, *the projectile binding energy* [84]) due to the fact that the target electron (*as seen from the projectile frame*) must have sufficient energy that it can ionize the projectile and simultaneously escape from the target [85]. Therefore, projectile ionization process in which there is simultaneous excitation and ionization of the target, become dominant at high projectile velocities [86]. To achieve simultaneous target and projectile

ionization only one Coulomb interaction is necessary for the (e-e) process. In the case of (e-N) process two Coulomb interactions (*projectile nucleus with one of the target electrons and target nucleus with the active projectile electron*) are needed [85].

Furthermore, the cross section for the (e-N) interaction can be expected to dominate the cross section for projectile ionization at impact parameters around the shell radius of the projectile while the (e-e) interaction is expected to dominate at larger impact parameters since the nuclear potential of the target (*that might cause ionization of the projectile in an* (e-N) *interaction*) is effectively screened by the target electrons [85, 87].

The shape of the ELC cusp (*characterized by the* FWHM *and the forward-backward asymmetry with respect to the cusp peak*) was investigated theoretically [79, 80, 81]. In the longitudinal electron spectrum, an almost symmetric cusp shape is predicted with FWHM that increases linearly with the projectile velocity. For a fixed spectrometer acceptance half angle $\vartheta_\circ$, the FWHM of the cusp when it is parallel to the direction of the bombarding ion beam is given by [80, 81]

$$(\Delta v_e)_{||} = \frac{3}{2} v_p \vartheta_\circ \tag{2.39}$$

which is similar to the analytic expression derived by Dettmann *et al* [66] describing the cusp shape of ECC velocity distribution. For highly charged projectiles having relatively loosely bound L-shell electrons, Burgdörfer [88] has calculated an almost symmetric cusp with a narrow width nearly independent of the projectile velocity, projectile charge state, or the target (*figure* 2.12). However, measurements [4, 89] of the ELC cusp shape revealed that the ELC cusp is nearly symmetric as predicted by the theory but with FWHM that is nearly constant independent of the projectile velocity and weakly dependent on projectile charge state (*mostly from broadening due to autoionization lines in the wings of the cusp*).

Generally, ELC bears a rather special relationship to the ionization process because of its ability to examine those electrons having only very small energies relative to the projectiles from which they were ejected.

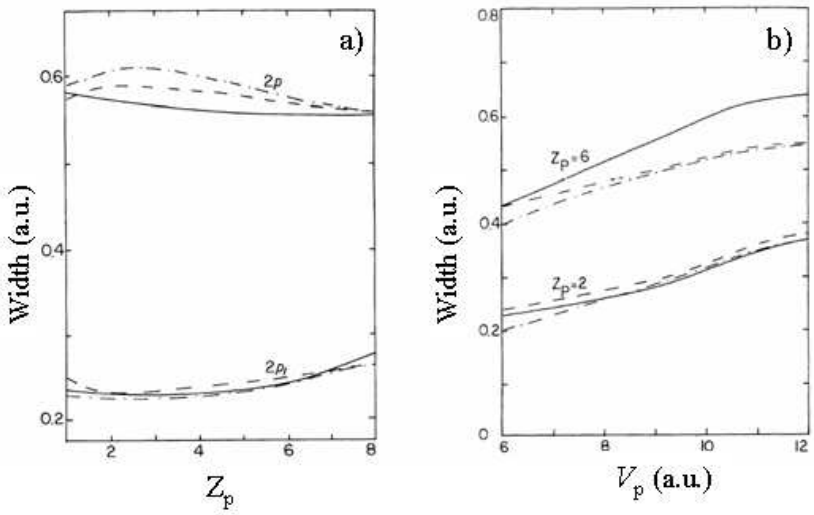

Figure 2.12: Cusp width as a function of a) the projectile charge Z_p for $2p_1$ and average $2p$ states b) the projectile velocity v_p for different Z_p and targets: hydrogen (full line); helium (dashed line); and argon (dash-dot line) adapted from [88].

2.2.2 Electron Capture to Continuum

When a projectile collides with a target atom, emitted electrons can originate from the ionization of the target as well. However, an electron ionized from a bound state of the target may be subjected to a post-collision long-range Coulomb interaction with the moving projectile capturing it into a low-lying projectile centered continuum state. This process of capturing a bound target electron to the projectile continuum can follow either a non-radiative (*abbreviated* **ECC**) or a radiative (*abbreviated* **RECC**) process accompanied with simultaneous emission of a photon (*figure* 2.13).

In the ECC and RECC processes initial and final states are identical except for the presence of a photon appearing with the RECC. The relative contribution of the ECC and RECC to the entire capture cross section depends strongly on the collision velocity. Dettmann *et al* [66] developed an expression for the ECC singly differential cross section. They obtained the result

$$\frac{d\sigma_{ECC}}{dv_e} \sim \frac{2^{17}}{5} Z_p^3 Z_t^5 (\frac{e^2}{\hbar v_p})^{10} (\frac{1}{v_p^2}) \times [\sqrt{(v_e - v_p)^2 + (v_p \vartheta_\circ)^2} - |v_e - v_p|](\pi a_\circ^2) \quad (2.40)$$

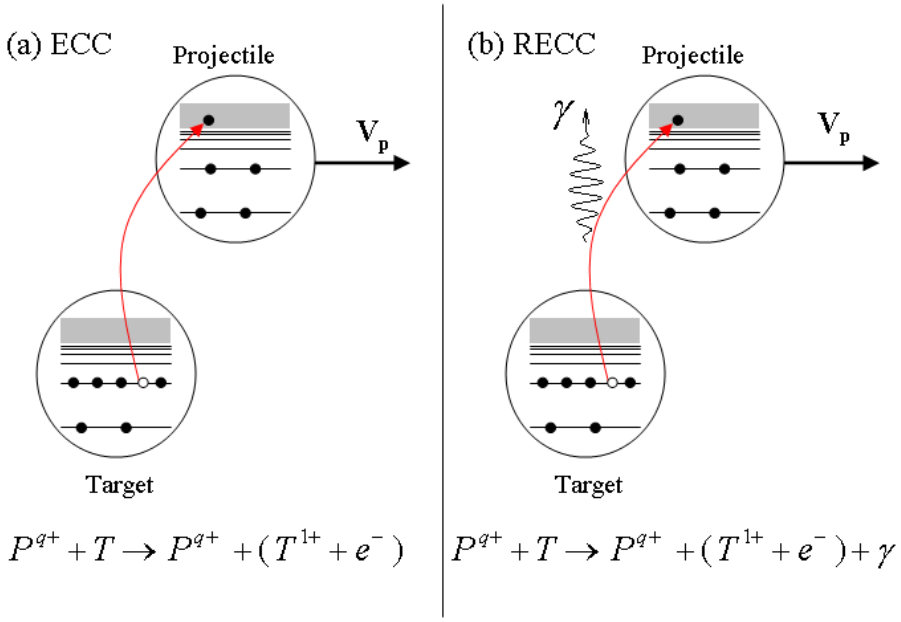

Figure 2.13: Schematic representation of the (a) ECC (b) RECC processes.

where Z_p and Z_t are the projectile and target atomic numbers respectively, v_p and v_e are the projectile and emitted-electron laboratory velocities respectively, e is the electronic charge, $\hbar$ is the reduced Planck constant, $a_\circ$ is the Bohr radius, and $\vartheta_\circ$ is the spectrometer acceptance angle. The differential cross section for the RECC was obtained by Shakeshaft and Spruch [14] as

$$\frac{d\sigma_{RECC}}{dv_e} \sim \frac{2^6}{3} Z_p^2 Z_t \left(\frac{e^2}{\hbar v_p}\right)^3 \left(\frac{1}{v_p^2}\right) \times \left[\sqrt{(v_e - v_p)^2 + (v_p \vartheta_\circ)^2} - |v_e - v_p|\right](\pi a_\circ^2) \quad (2.41)$$

A fourfold differential cross section ($\frac{d^4\sigma}{dE_e d\Omega_e dE_\gamma d\Omega_\gamma}$) based on a relativistic formulation of the impulse approximation for the RECC by very fast and very heavy projectiles is calculated by Jakubaßa-Amundsen [7] (*the expression is too lengthy to be mentioned here*). Note that the velocity dependence of the ECC ($d\sigma_{ECC} \propto v_p^{-12}$) and the RECC ($d\sigma_{RECC} \propto v_p^{-5}$) processes implies that both branches of the capture cross section decrease with collision velocity and that the non-radiative capture (ECC) is the dominant mechanism at moderate collision energies while the additional photon emission becomes important at

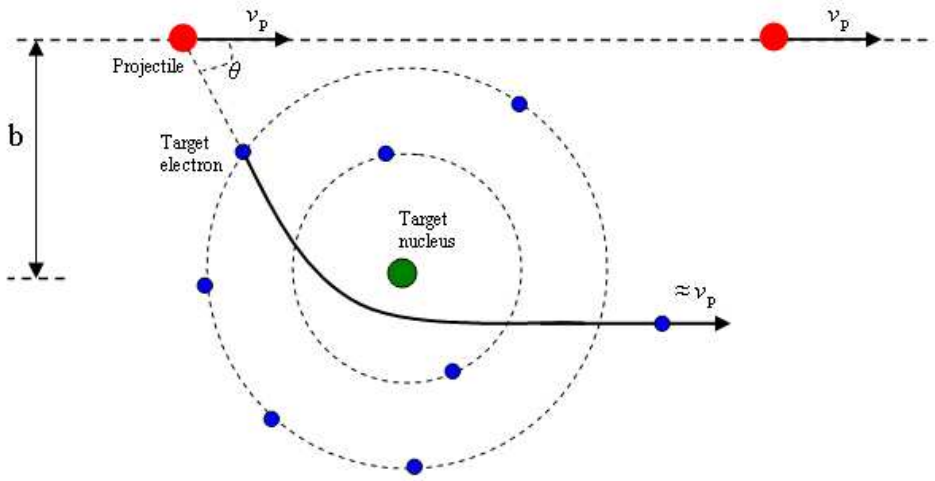

Figure 2.14: Schematic diagram of the double scattering mechanism used to describe the ECC process.

sufficiently high energies (>13 *MeV/u for protons*, ≈ 50 *to* 100 *MeV/u for uranium*).

For the ECC process to take place the target electron must acquire a velocity very close to the velocity of the projectile. This needs a violent collision with a large minimum momentum transfer to a target electron of the order $q_{min} \cong v_p$ so that it finally ends up in a low-lying continuum state around the projectile [8]. This can be viewed as a double scattering mechanism which requires (*from conservation of energy and momentum*) that, in the laboratory frame, the target electron first be knocked by the projectile towards the target nucleus at large angles (*with respect to the direction of the projectile motion*) with a speed very close to the projectile speed. The target electron then scatters from the target nucleus itself without change of speed, and emerges with a velocity very close to the projectile velocity (*figure* 2.14). The mutual attraction between the scattered target electron and the projectile nucleus then serves to bind them. This double scattering mechanism (*first suggested by Thomas* [90] *in the case of protons and hydrogen targets*) is a two-step process which should therefore correspond to a second Born term in the quantum mechanical treatment of the ECC process [14, 91].

Rudd [2] and Macek [9] have given theoretical explanation of the ECC cusp

and pointed out that ECC can be visualized as a smooth continuation across the ionization limit of capture into excited bound states with increasingly larger orbits such that the captured electron finally becomes unbound and that the population of low-lying continuum states and high-lying Rydberg states should be strongly related to one another [10].

The most remarkable feature in the ECC cusp is the strong asymmetry in the sense of an enhancement of the emission of lower energy electrons (*figure* 2.15). This has been observed with heavy [4, 92] and light [71, 93, 78] projectiles and has been discussed in details by Meckbach *et al* [94]. This skewness of the ECC cusp towards lower laboratory energies is intrinsic to the process and may be attributed to the Coulomb interaction of the emitted electron by the residual parent ion during the collision especially in the case of low Z projectiles [94]. Burgdörfer [10] emphasized that a measurement of the asymmetry of the double differential cross section for the ECC cusp allows the determination of the charge asymmetry of the electron clouds and may reveal information on the shape of Rydberg orbits and thus provides unprecedented details of the dynamics of the transfer mechanism.

From the theoretical point of view, the skewness of the ECC cusp towards lower laboratory velocities has been traditionally interpreted as a clear signature of the presence of a strong second-Born contribution in the electron capture amplitude since the first-Born approximation to charge transfer gives an isotropic electron distribution in the limit $v \to 0$ [5, 6, 7]. As an example, figure (2.15) is adapted from the calculations of Shakeshaft and Spruch [5] and represents a comparison between the contribution to the differential cross section from the first-order Born term (*the blue symmetric curve*) and the contribution from the sum of the first- and the second-order Born term (*the red negative skewed curve*).

The shape of the radiative capture to continuum RECC cusp distribution has never been subject of investigation until Jakubaßa-Amundsen work [7] even though the active mechanism is distinct from the non-radiative ECC. She has predicted an asymmetry in the RECC cusp skewed to the high energy side and thus opposite to that found for the non-radiative ECC. For weakly relativistic systems, this RECC asymmetry scales approximately with $Z_{proj}/\gamma v_{proj}$

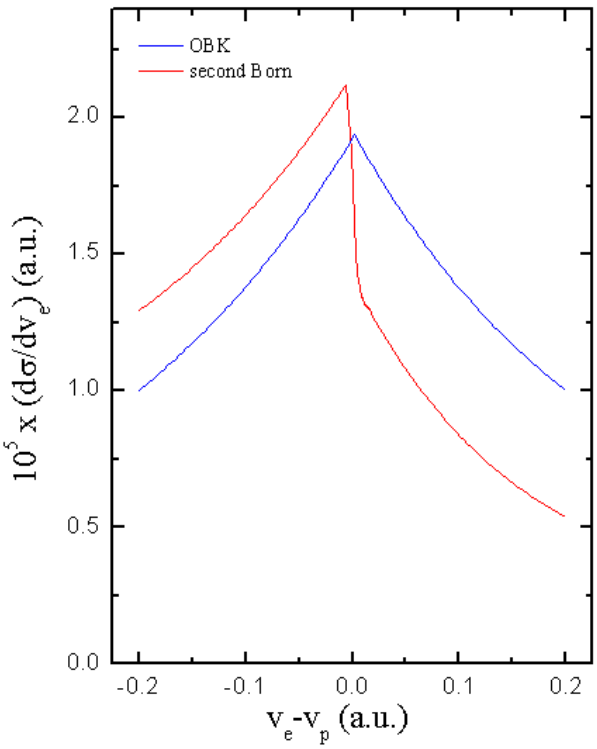

Figure 2.15: Singly differential cross section for continuum electron capture from the 1s state of a hydrogen atom by a bare ion of atomic number Z_B=6 incident with an energy 2 *MeV/u* in the lab frame. The blue curve is the contribution to the differential cross section from the first-order Born term, while the red curve is the contribution from the sum of the first- and the second-order Born term. Figure adapted from Shakeshaft and Spruch [5].

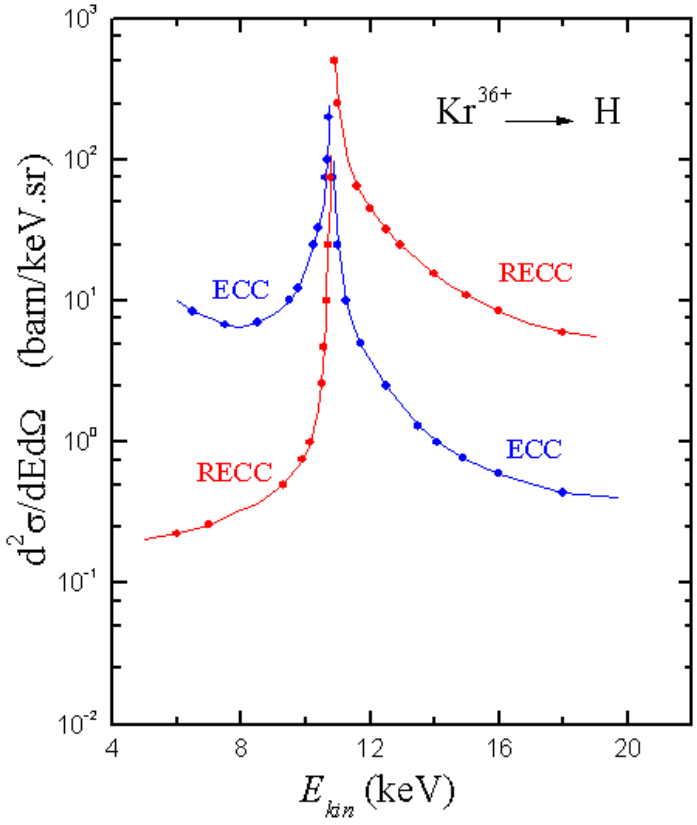

Figure 2.16: Opposite asymmetries in the doubly differential cross section for ECC (blue) and RECC (red) for forward electron emission in 20 MeV/u Kr^{36+} + H collisions as a function of kinetic electron energy. Figure adapted from Jakubaßa-Amundsen [7].

(*increasing strongly with projectile charge* Z_{proj} *but decreasing with projectile velocity* v_{proj}) and is considerably stronger than that for ECC. Figure (2.16) is adapted from Jakubaßa-Amundsen work [7] and represents the calculated opposite forward-backward asymmetries in the doubly differential cross section ($\frac{d^2\sigma}{dEd\Omega}$) for ECC and RECC precesses for the 20 MeV/u Kr^{36+} + H collision.

A physical interpretation of the forward-backward opposite asymmetries of ECC and RECC was given by Jakubaßa-Amundsen [7]. In the ECC process the cusp electrons originate from high momentum components of the target $p_z > v_{proj}/2$ (p_z *is the longitudinal momentum*), which scatter quasielastically from the projectile. Elastic scattering favours forward angles, such that the electrons are predominantly emitted antiparallel to the beam direction (*left*

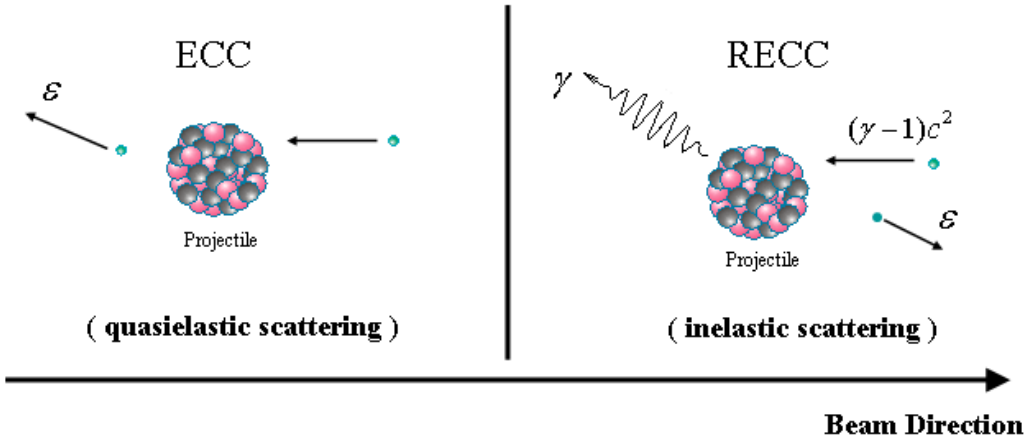

Figure 2.17: Schematic view of electron scattering from the projectile during the ECC process (left) and the RECC process (right). Figure adapted from Jakubaßa-Amundsen [7].

panel of figure 2.17) which leads to higher electron intensity at the lower energy side of the cusp. On the other hand, RECC is accompanied by the emission of photons so that the target bound state wave function does not need to contain high momentum components for providing overlap with the projectile wave function. This means RECC is caused by electrons approximately at rest in the target frame (*but having kinetic energy* $(\gamma - 1)mc^2$ *in the projectile frame*) which are decelerated to low energy ϵ while the excess energy is carried away by the emitted photon. These electrons bounce back from the projectile and are therefore mostly emitted in the beam direction (*right panel of figure* 2.17) which leads to higher electron intensity at the higher energy side of the cusp. Additionally, Jakubaßa-Amundsen has pointed out that a comparison between the non-radiative ECC cusp shape with the RECC cusp shape provides a sensitive test of the influence of the additional photon degree of freedom on the dynamics of the target ionization.

Simultaneous Bound- and Continuum-State Electron Capture

A process of particular interest is the situation when two target electrons are captured by the projectile, one into a bound state and the other into the

continuum of the projectile (*figure* 2.18).

$$P^{q+} + T \rightarrow P^{(q-1)+} + (T^{2+} + e^{-}) \tag{2.42}$$

Experimentally, when coincidence with emergent ion charge state is performed, ECC can be sorted as to whether additional bound state electron capture occurred during the same collision which generated the continuum electrons. Another channel that can give rise to the same final state is the correlated electron-electron capture in which two electrons are captured to highly excited states (*autoionizing states*) as

$$P^{q+} + T \rightarrow P^{(q-2)+} + T^{2+*}$$

with subsequent autoionization via electron emission to

$$P^{(q-1)+} + T^{2+*} + e^{-}$$

leaving the projectile in a final charge state $(q-1)$. When the impact parameter dependence for cusp electron production is studied [95] in coincidence with the emergent ion charge state at low collision velocities ($0.53\ MeV/u\ F^{8+} + Ne$), this correlated electron-electron capture process was observed to have the largest magnitude in probability, while the probability for processes leading to cusp electron emission when the projectile did not simultaneously capture an electron to bound states, which is the true pure one-electron capture to a continuum state of the projectile ECC, is very low. Moreover, the results of Breinig *et al* [4] and Vane *el al* [96] demonstrated directly that often one or more closely associated additional bound state captures occur whenever a continuum capture event is observed. They also pointed out that the cusp shapes observed are relatively independent of whether or not additional capture events occurred.

2.3 Inverse Kinematics

In RECC, a target electron approximately at rest in the target frame is captured into a low-lying continuum state of a fast highly charged projectile with simultaneous photon emission. The emitted photon will carry away the excess

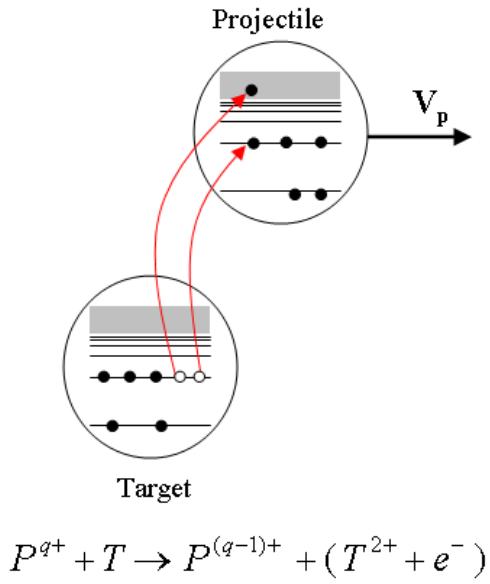

Figure 2.18: Schematic representation of the two electron ECC process.

energy of the electron allowing for high capture to continuum cross sections even when the relative velocity between the target and the projectile is high [7]. The target electron after being captured will find itself with very low positive kinetic energy in the projectile continuum but will appear in the laboratory frame having kinetic energy of $(\gamma - 1)mc^2$ due to the translational motion of the projectile and can easily be detected in the electron cusp under 0° with a velocity equal to the velocity of the projectile.

It is interesting to think about this RECC process from a different point of view. Instead of using the laboratory frame where the electron is at rest we view the process as taking place in the rest frame of the projectile. In this case, an observer sitting on the projectile will see the quasifree target electron coming with a high kinetic energy $(\gamma - 1)mc^2$ and collides with the stationary projectile ion and emits nearly the entire of its kinetic energy as an x-ray photon which then appears in the observed x-ray continuum as short wavelength limit bremsstrahlung while the incoming electron ends up with virtually zero velocity. This inverse picture of the RECC looks exactly like the e-n Bremsstrahlung process at the short wavelength limit. This means that

RECC is closely related to the bremsstrahlung emission of a fast electron in the field of the heavy projectile. In fact, within the impulse approximation (IA) the cross section for RECC is basically obtained by folding the cross section for e-n bremsstrahlung with the momentum distribution of the electron in its initial state [7].

It is of interest to note the very useful feature of using RECC as inverse kinematics. The kinematic transformation between projectile and laboratory frames results in a nonlinear but high gain amplification of small energy intervals very near zero energy in the projectile rest frame. For example, the [0 - 1 eV] electron kinetic energy interval in the rest frame of a 90 MeV/u projectile is transformed into the interval [49.372 keV - 49.827 keV] for zero degree electrons in the laboratory frame for an overall energy interval amplification factor of ≈ 455.

In conclusion, using RECC as inverse kinematics opens the door to the long desired access to the short wavelength limit of e-n bremsstrahlung by measuring the coincidence between the continuum electrons of the projectile and the emitted photons. For this reason one needs to turn attention to the forward electron emission and the continuum electrons of the projectile and to look at the different channels contributing to the cusp electrons which may interfere with the bremsstrahlung photons.

2.4 Binary Encounter

When an ion collides with an atom, ionization of the target may occur as a consequence of the transfer of kinetic energy from the projectile to target electrons by Coulomb interaction. Perhaps the simplest ionization mechanism is a two-body collision between a projectile and a target electron referred to as a binary encounter (BE) if the interaction of the ejected binary-encounter electron with the target nucleus is neglected [97, 98]. According to classical (*non-relativistic*) two-body kinematics, electrons initially at rest in the laboratory frame should be ejected with an emission angle θ-dependent velocity of

$$v_{BE} = 2v_p \cos\theta_{lab} \tag{2.43}$$

if their binding energy and also relativistic effects are neglected (v_p *denotes the projectile velocity*). This corresponds to an energy of

$$E_{BE} = 4(\frac{m_e}{M_p})E_p \cos^2\theta_{lab} \tag{2.44}$$

where m_e is the electron mass, M_p is the mass of the projectile, and E_p is the projectile energy . In the case of forward electron spectrometry ($\theta = 0°$, *present work*) the binary encounter peak is expected at $v_{BE} = 2v_p$ ($E_{BE} = 4(\frac{m_e}{M_p})E_p$) which is the maximum velocity a target electron can acquire in a binary collision with the projectile.

At relativistic velocities (*but still no binding effects*), the momentum of the ejected electron $P = \gamma m v_e$ rather than its velocity v_e is the relevant quantity which can be related to the projectile velocity v_p as:

$$P = \frac{2\gamma\sqrt{\gamma^2 - 1}}{\alpha} \tag{2.45}$$

with $\gamma = (1 - (v_p/c)^2)^{-1}$ and α is the fine structure constant ($\alpha \simeq 137$). The kinetic energy of the ejected binary encounter electron in this case can be given by [99]:

$$E_{BE} = \frac{2v_p^2 \cos^2\theta_{lab}}{1 - \beta^2\cos^2\theta_{lab} + 2m_e/(M_p\gamma) + m_e^2/(M_p\gamma)^2} \tag{2.46}$$

The target nucleus now comes into play in that the electrons are bound to it in different shells. Therefore, the observed distribution of binary encounter electrons at a fixed angle is not a δ-function as described by equation (2.43), but a broad distribution centered around v_{BE} which reflects the initial one dimensional momentum distribution of the bound electrons of the target atom (*projected onto the axis of the projectile trajectory*), that is, the "Compton profile" [100, 101]. Both the momentum distribution and the binding energy cause a slight shift of the binary encounter peak towards lower energies [102].

It is noteworthy that in the case of collisions of bare ions with a few-electron target (*pure target ionization*), the electron-ion elastic scattering cross section is smooth and given in the projectile frame by the classical Rutherford formula. In this case, the result of convolution of the elastic scattering cross section with

the electronic momentum distribution is that a symmetric binary encounter peak is produced with a width that is proportional to the target Compton profile [99, 103]. For projectiles with many electrons (*partially stripped ions*), the elastic scattering cross sections are not smooth, but have significant structure or oscillation and are larger for these ions than for bare projectiles at backward angles in the projectile frame. It is explained as being due to the interference between the static Coulomb scattering amplitude and the additional scattering amplitude due to the short-range potential of the screened ions[104, 105]. This leads to enhanced binary encounter peaks in the forward direction in the laboratory frame. Here, the convolution of the elastic scattering cross section with the electronic momentum distribution will result in a binary electron distribution which reflects these oscillations [103].

2.5 Kinematics of Inelastic Ion Atom Collisions

In this section, only a short summary on the kinematics of inelastic ion atom collisions will be given which is helpful for the understanding of experimental aspects and results mentioned in chapter 3 of this work. details can be found elsewhere [106, 107, 108, 109]. The typical momentum transfer in most ion atom collisions is in the range of a few atomic units. This is only a very small fraction of the initial momentum of the projectile in most collisions (*for example in a few MeV* H^+ *on* He *collisions the momentum exchange is less than* 10^{-4} *of the initial projectile momentum*). Thus observation of momentum transfer in ion atom collisions by projectile detection (*scattering angle and/or energy gain or loss measurements*) is restricted in resolution by the fact that in the laboratory system a small change of a huge momentum must be resolved. Much higher resolution can be achieved by measuring quantities like electron or recoil ion momenta since these reaction products are initially nearly at rest in the laboratory frame. Because any momentum change of the projectile must be compensated by the sum momentum of the recoiling ion and all emitted electrons, the complete momentum balance of the reaction can be measured with much improved resolution by detecting recoil ions and electrons

[110, 111, 112].

In the collision process, the projectile and its electrons (*if non-bare ionic projectiles are used*) interact with the target atom through Coulomb interaction. The three most important processes can be induced are: ionization of n_T target electrons, ionization of n_p projectile electrons, and the capture of n_c target electrons into projectile bound states. Certainly, all these reaction channels might occur simultaneously within the same collision. As a result, there will be N fragments in the final state with $N = n_T + n_p + 2$ for ion impact and a total of $n = n_T + n_p$ electrons released to the continuum. Due to momentum and energy conservation, the collision kinematics is fully determined if $3N - 3$ linear independent (*scalar*) momentum components are measured in kinematically complete experiments (*neglecting the spin*). Then, fully differential cross sections can be extracted. The energy change of the projectile (ΔE_p) resulting from nonrelativistic energy conservation is given by (*all in atomic units where the electron mass m_e, the electron charge e, and the planck's constant $\hbar$ is equal to unity*: $m_e = e = \hbar = 1$):

$$\Delta E_p = -Q + \frac{1}{2}(n_c - n_p)v_p^2 - \sum_{i=1}^{n_p+n_T} E_e^i \tag{2.47}$$

where Q (Q-*value*) denotes the change in internal energy of the projectile and the target, i.e. the energy difference between the final and initial bound electronic states $Q = E_f^{bind} - E_i^{bind}$, v_p is the projectile velocity, and E_e^i is the continuum energy of the i^{th} electron in the laboratory frame. The momentum change of the projectile in the longitudinal direction $\Delta P_{p||}$ can be related to the energy change as:

$$\Delta P_{p||} = \frac{\Delta E_p}{v_p} = -\frac{Q}{v_p} + \frac{1}{2}(n_c - n_p)v_p - \sum_{i=1}^{n_p+n_T} \frac{E_e^i}{v_p} \tag{2.48}$$

From momentum conservation laws it follows for the longitudinal momentum of the recoil ion ($P_{R||}$):

$$P_{R||} = -(\Delta P_{p||} + \sum_{i=1}^{n_p+n_T} P_{e||}^i) \tag{2.49}$$

where $P^i_{e||}$ is the final momentum of the i^{th} electron. Using equation (2.48) we come to the general result

$$P_{R||} = \frac{Q}{v_p} + \frac{1}{2}(n_p - n_c)v_p + \sum_{i=1}^{n_p+n_T}(\frac{E^i_e}{v_p} - P^i_{e||}) \tag{2.50}$$

This general equation can now be simplified if we focus on several special reaction channels.

2.5.1 Kinematics of Pure Electron Capture

In this process, n_c electrons are transfered from the target to bound states of the projectile ($n_p = n_T = 0$). For pure electron capture, only discrete values of $P_{R||}$ occur corresponding to the energy eigenvalues of the projectile and target electrons. Equation (2.50) reduces to

$$P_{R||} = \frac{Q}{v_p} - \frac{1}{2}n_c v_p = -\Delta P_{p||} \tag{2.51}$$

and the final longitudinal recoil-ion momentum directly reflects the Q-value of the reaction.

2.5.2 Kinematics of Pure Target Ionization

For pure target ionization ($n_p = n_c = 0$), in the longitudinal direction one obtains

$$P_{R||} = \frac{Q}{v_p} + \sum_{i=1}^{n_T}\frac{E^i_e}{v_p} - \sum_{i=1}^{n_T}P^i_{e||} \tag{2.52}$$

The Q-value is given by the sum of the well known sequential ionization potentials of the emitted electrons and the excitation energies of the remaining target (*and projectile*) electrons (*if non-bare ionic projectiles are used*). So, Q/v_p is fixed for a given beam velocity and final target (*and projectile*) excitation and the recoil-ion longitudinal momentum only depends on the energies and longitudinal momenta of the emitted electrons [113, 114].

For very low-energy target electrons (*continuum electrons*) at large projectile velocities, the condition

$$\frac{Q + \sum_{i=1}^{n_T} E_e^i}{v_p} \ll P_{R||} \tag{2.53}$$

is valid. Consequently, the first two terms on the right-hand side of equation (2.52) are small and the recoil-ion longitudinal momentum distribution mirrors the sum-momentum distribution of the emitted electrons along the beam direction $P_{R||} = -\sum_{i=1}^{n_T} P_{e||}^i$.

2.5.3 Kinematics of Pure Projectile Ionization

For the ionization of n_p electrons of the projectile ($n_c = n_T = 0$) from equation (2.50) it follows:

$$P_{R||} = \frac{Q}{v_p} + \sum_{i=1}^{n_p} \frac{E_e^i}{v_p} \tag{2.54}$$

For this case one can calculate the total energy loss (*or gain*) of the projectile directly from the measured $P_{R||}$.

Chapter 3

The Experiment

3.1 The GSI Accelerator Facility

Ion beams of bare and few electron projectiles with beam energies extending up to the relativistic energy regime can be produced at the GSI accelerator facility. It consists of the linear accelerator (UNILAC), the heavy ion synchrotron (SIS), and the experimental storage ring (ESR). The Layout of the accelerator facility and experimental areas at GSI are displayed in figure (3.1).

The large number of experiments performed at the GSI accelerator facility are demanding a great variety of different ion species and beam intensities. For that purpose, ion beams of most elements across the periodic table up to uranium are delivered to the UNILAC by three different injectors equipped with three different ion sources: the standard injector with a penning ion source, the high current injector with a MEVVA ion source, and the high charge state injector (HLI) with an ECR ion source. For details about ion sources used at GSI see [115, 116, 117, 118].

After being produced in the source, low-charge uranium ions (U^{+4}, ..., U^{+10}) are first pre-accelerated in the UNILAC which is designed to accelerate all ion species with mass over charge ratios of up to 8.5. The UNILAC consists of three main parts: the 36 MHz high current RFQ/IH-injector, a N_2 gas stripper section at energy of 1.4 MeV/u and maximum charge state of 28+ for uranium, and finally a 108 MHz Alvarez type radio frequency (RF) accelerator which accelerates ions up to an ion-beam-energy of 11.4 MeV/u which is sufficient to fill

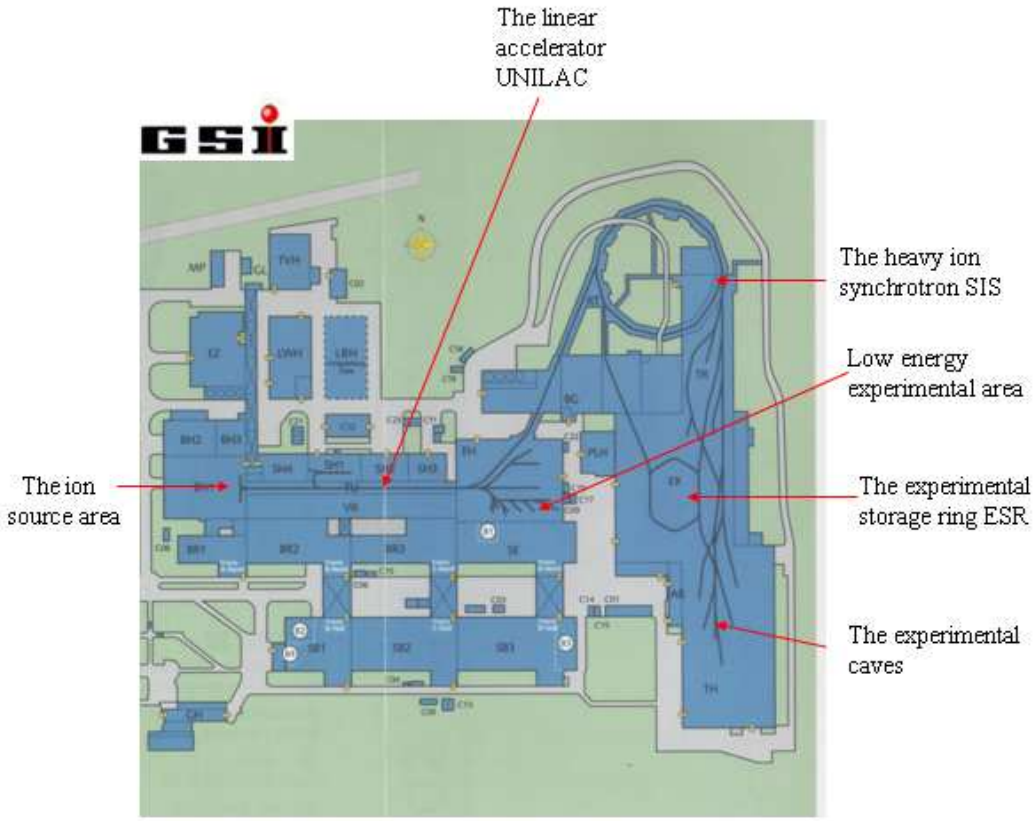

Figure 3.1: Layout of the accelerator facility and experimental areas at GSI.

the SIS up to its space charge limit [119]. After 110 m acceleration, ion beams can be supplied simultaneously to low energy experiments ($\leq$ 11.4 MeV/u) and the injection line for the heavy ion synchrotron SIS in a fast time sharing mode based on the 50 Hz macro-structure of the beam [120]. Subsequently, the ion beam passes through a thick ($few\ mg/cm^2$) carbon stripper foil. Then the charge state of 73+ is magnetically separated and transported towards the heavy-ion synchrotron SIS where ions are subjected to a further acceleration. The SIS is a fast cycled, free programmable, separated function machine with circumference 216 m and maximum magnetic rigidity of 18 Tm. The magnetic rigidity of the SIS limits the range of available specific ion energies to 2 GeV/u for light ions, e.g. Ne^{10+} and 1 GeV/u for U^{73+}. SIS bunches are then transferred through a transfer line towards the experimental installations like caves A, B, and C, the fragment separator (FRS), and the ESR. In the transfer line, ions may be stripped and from the emerging charge state distribution, the beam fraction in the required charge state is magnetically separated. In order to strip ions to very-high-charge states, successive collisions are required and a center-of-mass energy greater than the total binding energy of all the electrons is to be removed. In equilibrium stripping, the mean charge state of the outgoing beam after stripping is the charge state such that all electrons with orbital velocities less than the projectile velocity are removed. For example, for the case of uranium ions where the K-shell binding energy amounts to $\approx$ 130 keV, a beam energy of at least 300 MeV/u is required in order to produce fully stripped ions with sufficient intensity, a beam energy which corresponds approximately to $\beta = 0.6$, where β denotes the ion velocity in units of the speed of light c. For this purpose the SIS bunches intended for transfer to ESR pass in the transfer line through a thick 20 mg/cm^2 Cu stripper foil. The beam may be first directed to the large fragment separator FRS before being transferred to the ESR [121].

3.2 The Experimental Storage Ring ESR

The heavy-ion storage ring ESR at GSI in Darmstadt is the only storage ring capable to store high-Z ions at relativistic energies (*from* 4 MeV/u *up*

to 556 MeV/u); it represents a unique part of the accelerator facility of the GSI. Figure (3.2) shows a schematic sketch of the ESR storage ring and its main components such as the electron cooler device, the internal gas-jet target, the x-ray detector chamber, the forward electron spectrometer, and the radio frequency cavities (*rf-cavities*). The magnetic rigidity of the ESR amounts to 10 Tm which corresponds to a specific beam energy of 556 MeV/u for U^{92+}.

The ring geometry is a stretched hexagon determined by a special magnet structure and consists of 6 bending magnets and two 10 m long magnet-free straight sections leaving sufficient space for electron cooling and in-ring experiments. The circumference of the ESR amounts to 108.36 m which is exactly one half of the SIS-circumference and represents the result of carefully balancing the advantages of small ring size against the demand for easy beam transfer and comfortable space for special equipment for beam cooling and in-ring experiments [120, 122, 123].

In the storage ring the injected ion beam is very efficiently cooled by Coulomb interaction with co-moving electrons in the 2.5 m long electron cooler section [124]. The electron cooler current I determines the cooling power which is directly proportional to I. However, operation with high electron currents is less desirable in most applications for experiments with highly charged ions because the beam lifetime drops significantly with increasing the current: $\tau \propto 1/I_{cooler}$ where τ is the beam lifetime. The electron cooler current causes beam ions and cooler electrons to recombine thus reduces the beam lifetime of the cooled heavy ion beams under UHV conditions by the REC. The estimated lifetime of U^{92+} beam at 20 MeV/u is about 100 *sec.* Therefore, a high efficiency of the cooling system is desired in order to reduce ion beam losses by operation of the electron cooler at low electron currents [125]. For this purpose, Electron currents up to 1 A are applied if fast cooling is required. For cooling of stored beams, electron currents of typically 100 to 300 mA are preferred [126]. Electron energy and electron current can be set independently in order to match the cooling parameters to the needs of the experiment. The electron cooling system was designed for operation in the energy range from a few keV up to a maximum electron energy of 320 keV. Presently its maximum accelerating voltage for breakdown safe operation is 240 keV corresponding to an ion en-

Electron energy	1.6 - 240	keV
Electron beam current	0.001 - 1	A
Electron beam density	2×10^8	cm^{-3}
Electron beam diameter	50.8	mm
Electron beam temperature	transverse 0.1	eV
	horizontal ~ 0.1	meV
Length of cooling section	2.5	m
Diameter of cooling section	25	cm
Magnetic guiding field	0.015 - 0.2	T

Table 3.1: The main parameters of the electron cooler in the ESR at GSI.

ergy of 440 MeV/u [127]. A variable longitudinal solenoidal magnetic guiding field of $\approx 0.1\ T$ is also applied in the electron cooler in order to conserve the electron beam diameter of $\approx 50\ mm$ [124, 128]. In figure (3.3), the layout of the electron cooler design as used at the ESR is shown. The main parameters of the electron cooler are listed in table (3.1).

Electron cooling in the ESR is applied to provide ion beams of low momentum spread. Electron cooling reduces the relative longitudinal momentum spread in the injected ion beam from $\Delta p/p \approx 10^{-3}$ to about 10^{-5} and the transverse emittance of the stored ion beam from about $5\pi\ mm\ mrad$ to less than $0.1\pi\ mm\ mrad$. However, both the transverse emittance and the relative momentum spread of the stored beam depend on the number of stored ions and the applied cooler current. The large reduction in the longitudinal momentum spread of strongly electron-cooled heavy ions in the ESR is explained by the fact that intrabeam scattering becomes strongly suppressed. This in turn is interpreted at low intensities as the effect of beam ordering, in such a way that the ions become lined up after one another like beads on a string without being able to pass each other due to their small relative velocity which is due to the cooling and the strong Coulomb repulsion between the highly charged ions [130]. In particular, electron cooling ensures a well-defined beam velocity with a velocity spread better than $\Delta\beta/\beta \approx 10^{-4}$. For detailed discussion of the electron cooling technique see [129].

For the cooling process, a certain cooling time t_c is needed which may be

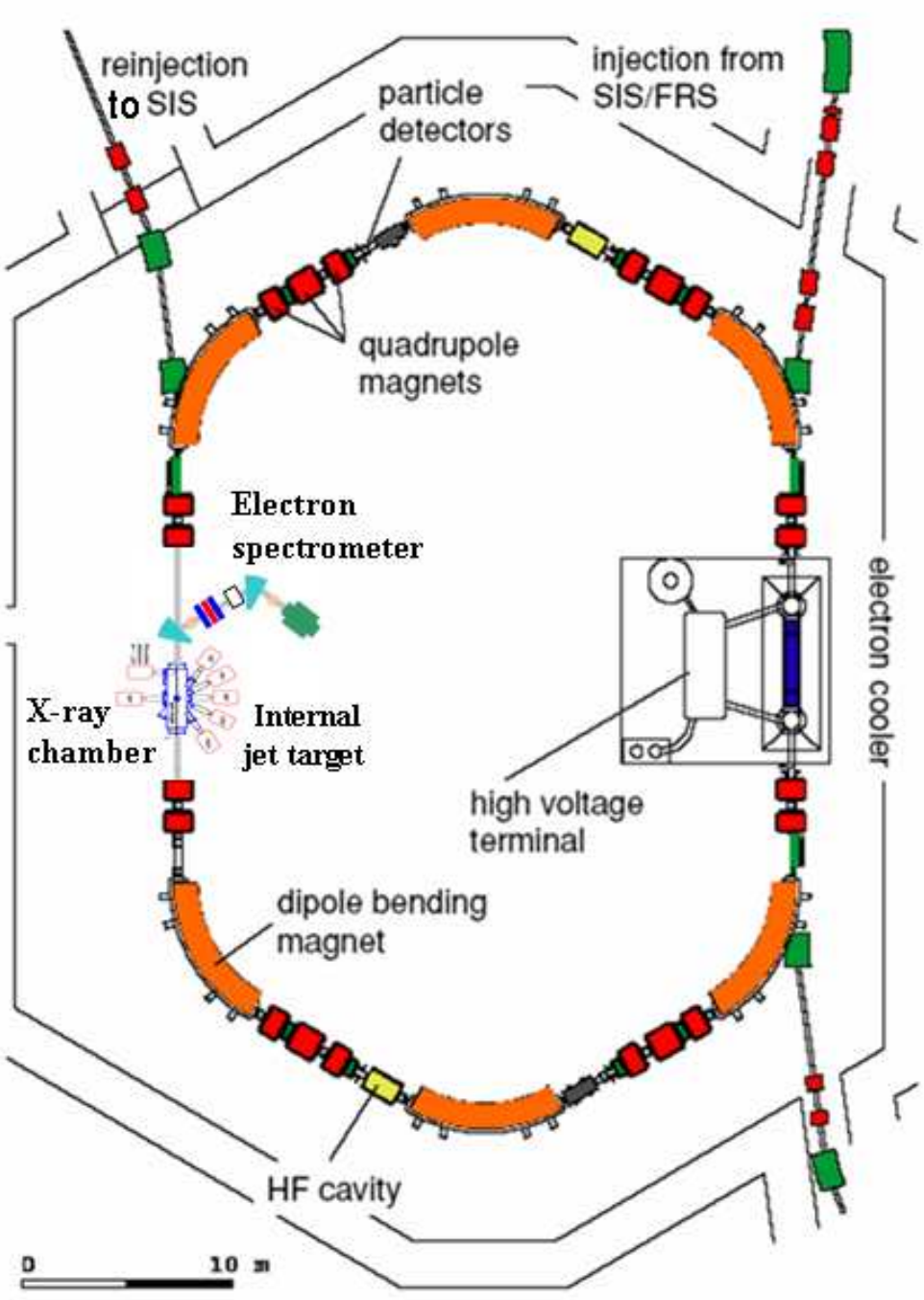

Figure 3.2: Schematic presentation of the storage and cooler ring ESR at GSI-Darmstadt. The layout depicts the beam guiding system (dipole bending magnets, quadrupoles and hexapoles) as well as the most important installations for beam handling and diagnostics (kicker, rf cavities, electron cooler). The positions of the internal jet-target, x-ray detection chamber, and the forward electron spectrometer are marked in addition [122, 123].

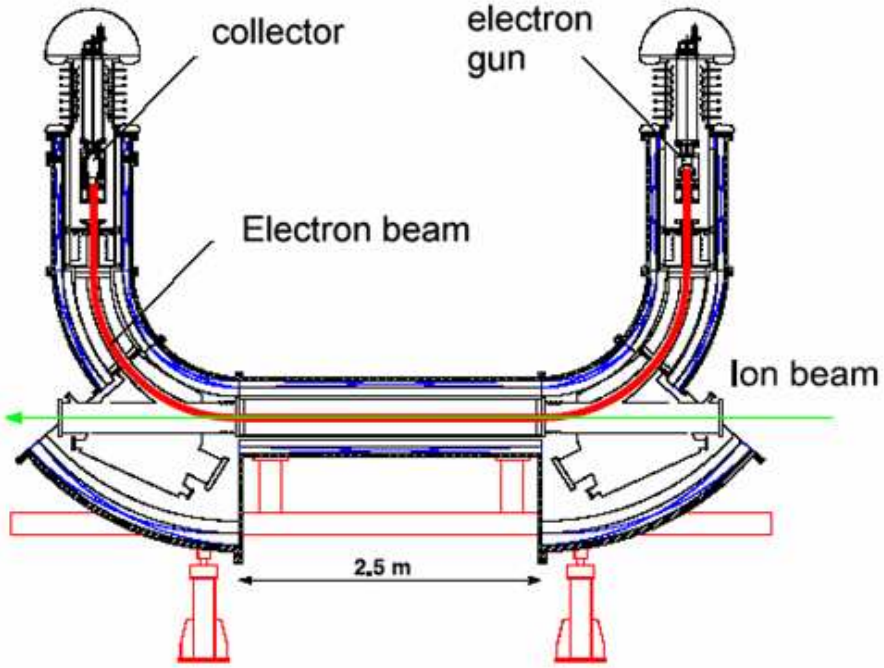

Figure 3.3: Layout of the electron cooler device used at the storage and cooler ring ESR. Electrons produced in the electron gun at a cathode temperature of $\approx 1300\ K$ are guided by a $\approx 0.1\ T$ magnetic field co-propagating over a distance of 2.5 m with the stored ion beam [129].

considered also as a lower limit for lifetimes of the radioactive nuclei to be stored, cooled and experimented with in the ESR. Electron cooling theory [131, 132] gives a $\frac{1}{Z^2}$ and $\frac{1}{I_{cooler}}$ cooling time dependence: $t_c \propto \frac{1}{Z^2 I_{cooler}}$; where Z is the projectile mass, and I_{cooler} is the electron cooler current. For U^{88+} and the parameters of this work, a cooling time of about 1 *sec* is expected [123].

Both the revolution frequency, corresponding to the momentum of the ion beam assuming the beam trajectory is known, as well as the momentum spread can be measured via Schottky-noise detection. The schottky noise is the statistical noise in the beam current. It is due to the fact that the beam is made up of finite number of individual particles which generates microscopic charge-density fluctuations in the ion beam which appear in the form of a fluctuation of the instantaneous beam current around its macroscopic average and also a fluctuation in the revolution frequency of the ion beam [133, 134]. The frequency spread ($\Delta f/f$) of the beam is detected by a capacitive pickup consisting of four plates surrounding the ion beam. The resulting signal is recorded by a spectrum analyzer. And finally, the relative longitudinal momentum spread ($\Delta p/p$) is obtained from the measured relative frequency spread through the relation:

$$\frac{\Delta p}{p} = \frac{1}{\eta}\frac{\Delta f}{f} \tag{3.1}$$

where the frequency dispersion η is a machine parameter which depends directly on the relativistic parameter γ (*for the ESR* $\eta = 0.3$ *at* $\gamma = 1.6$)[130, 135]. As an example, a Schottky frequency spectrum of an uncooled ion beam in comparison with a cooled one is given in figure 3.4 [136].

The cooling technique also leads to more brilliant beams, i.e. to small beam sizes with typical diameters of less than 5 *mm*, this factor is in particular important for precise measurements at the jet target, where a control over geometrical factors and possible doppler corrections is required for precision measurements.

The effective number of stored particles per second available for experiments averaged over a time cycle of one day has been improved significantly within the last years from about 10^3 at 1992 to 10^6 at 1994. For high-Z ions, like uranium, more than 10^8 ions can meanwhile be stored routinely by using single

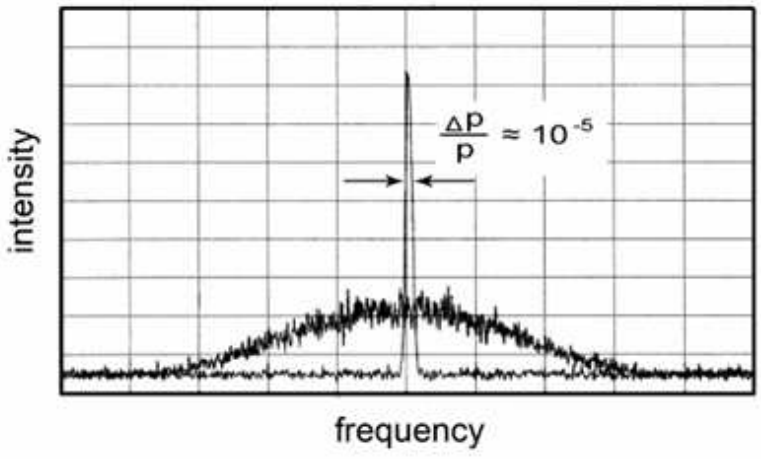

Figure 3.4: Schottky frequency spectrum for a circulating beam of U^{92+} ions at 295 *MeV/u*. The broad distribution refers to the non-cooled beam, measured directly after injection into the ESR. The narrow distribution reflects the momentum profile of a continuously cooled ion beam [136].

pulse from the SIS synchrotron. This number is still below the upper limit of particles which can be stored in principle. The limits are due to the space charge potential of the stored ion beams and restrict the number of stored ions e.g. for the case of bare uranium at 556 *MeV/u* to 9.3×10^9 and at 50 *MeV/u* to 4.4×10^8 [122, 123].

Another feature of the ESR is the possibility to store and cool simultaneously more than one charge state of an ion, e.g. two for Kr-, three for Au-, and even four for U- ions [120]. A further unique feature of the ESR is the deceleration capability. The beam, in general highly ionized ions stored and cooled at high energy, can be decelerated down to few *MeV/u* far below the production energy of ionic species which allows one to investigate charge exchange process for highly-charged ions in a completely new energy domain. For this purpose, the electron cooler has to be switched off and the coasting beam must be rebunched and decelerated while simultaneously ramping down the magnetic fields. At the final stage of beam handling, the electron cooler has to be switched on again. Using this procedure, bare uranium ions were successfully decelerated from 400 *MeV/u* to a minimum energy of 3 *MeV/u*,

Specific energy	3.0-556 ($^{238}U^{92+}$)	MeV/u
Number of ions	10^8	$sec.^{-1}$
Magnetic rigidity	0.5 - 10	Tm
Electrostatic rigidity	10 - 2550	MV
Ring circumference	108.36	m
Mean radius	17.246	m
$\Delta p/p$ range	0.1 - 0.001	%
$\Delta\beta/\beta$	0.01	%
Transverse emittance range	5π - 0.1π	$mm.mrad$
Beam diameter	3-5	mm
Cooling time	0.2 (for U^{92+})	$sec.$
Life time	100 (for U^{92+} at 20 MeV/u)	$sec.$
Target density	10^{14}-10^{17}	$mol.cm^{-3}$
Target thickness	0.3 - 300	$ng.cm^{-2}$
working pressure	10^{-11}	$mbar$
Backing temperature	300	$^\circ C$
Frequency range	0.85 - 5	MHz
Schottky pick up	3	

Table 3.2: The major parameters of the ESR.

the minimum energy of the ring, in about 1.5 *sec* [137]. In our measurement, the deceleration feature of the ESR was not used since the correct beam energy (90 MeV/u) was directly delivered from SIS and the beam was not to be decelerated.

The most severe source of beam losses in the ESR are charge changing collisions -mainly electron capture and, to a smaller extent, electron loss- between highly charged ions and residual gas molecules. The most critical process, electron capture at low energies, requires an ultrahigh vacuum (UHV) system of $\approx 10^{-11}$ $mbar$ pressure. One important technical complication due to this low pressure is the necessity of in situ baking of the system at 300 °C including all equipment for beam cooling and in-ring experiments [123]. The major parameters of the ESR are listed in table (3.2).

3.3 The Internal Supersonic Jet-Target of the ESR

In order to produce high-density targets and at the same time maintain the UHV in the ring, the ESR is equipped with a supersonic gas jet target which has become a standard device to perform in-ring experiments. In figure (3.5), a schematic sketch of the gas jet is shown [138]. The jet is produced by expanding a gas through a Laval nozzle of 0.1 *mm* in diameter. To meet the ultrahigh vacuum (UHV) requirements of the ESR ($\approx 10^{-11}$ *mbar*), the actual set-up consists of an injection and a dump section, both separated by skimmers in four stages of a differential pumping system. The pass of the free jet in the UHV of the interaction chamber is 70 *mm*. For a detailed description of the design and principle of operation of the target set-up see [138, 139].

In order to operate the target with very different gas species at optimum performance, the distance of the nozzle to the first skimmer can be adjusted 3-dimensionally via remote control. This allows one to achieve a density variation by up to a factor of 10 for all the various target species available for experiments [139]. Under experimental conditions, the typical distance between the nozzle and the first skimmer amounts to 30 *mm* for light gases and 60 *mm* for heavy gases.

The input pressure can be varied from 100 *mbar* to 20 *bar*, depending on the nozzle geometry and the gas species used. Target gases currently available are: H_2, N_2, CH_4, Ar, Kr and Xe. For the expensive noble gases such as krypton or xenon, a recycling system is used, which cleans and recompresses the gas. The typical gas-jet target density amounts to about 10^{12} *particle/cm*^{3} [138], which should be compared with a typical density of a solid state target of about 10^{21} *particle/cm*^{3}. The 10^{-11} *mbar* UHV-pressure in the surrounding chamber corresponds to residual gas density of about 10^5 *particle/cm*^{3} and contributes only 10^{-5}% to the total target density.

A further most important parameter of the target is its geometrical diameter of about 5 *mm*. This follows from the geometry of the skimmer design and has been confirmed experimentally by using a photomultiplier to measure the counting-rate of photons from the interaction point at different positions of the

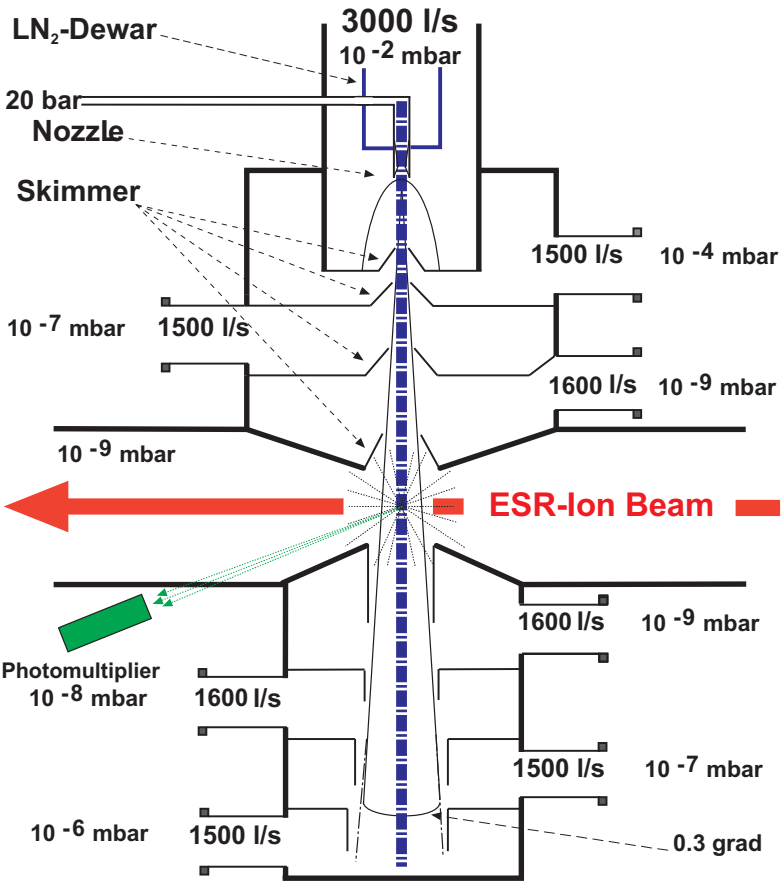

Figure 3.5: Schematic graph of the ESR internal gas-jet target [138, 139].

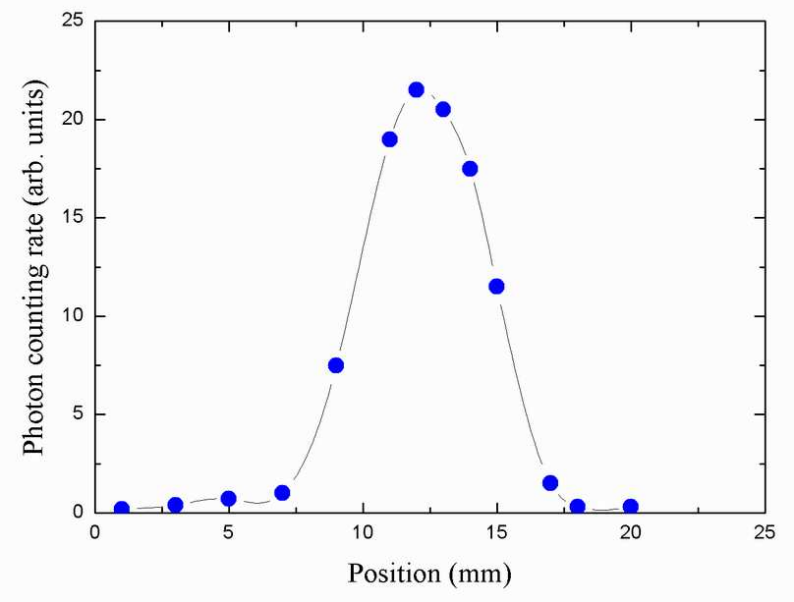

Figure 3.6: Normalized photon counting rate measured as a function of the ESR ion beam position [138].

ESR ion beam. Figure (3.6) shows an example of the photon counting-rate in normalized units as function of the position of a 370 MeV/u U^{92+} ion-beam interacting with a N_2 target (*target density* 2×10^{12} cm^{-3}). The measured function corresponds to a gas-jet diameter of 5 mm and an ion beam diameter of approximately 1 mm [138].

In experiments at the jet target, one must account for the partially dramatic effect of the atomic charge exchange processes in the target zone on the beam lifetime. This is particularly true when dealing with high-Z targets or with decelerated ions [140]. In general, the lifetime of a cooled ion beam is determined by the charge-exchange cross sections of the ions interacting with the residual gas and, as mentioned earlier, the radiative recombination rate in the electron cooler. However, if the gas-jet target is used, the lifetime of a beam is essentially determined by electron capture or loss processes occurring in the gas jet volume [140]. The cross section σ for the latter processes are related to the lifetime τ of the stored beam by the relation:

$$\frac{1}{\tau} \;=\; \lambda \;=\; \rho\sigma f \tag{3.2}$$

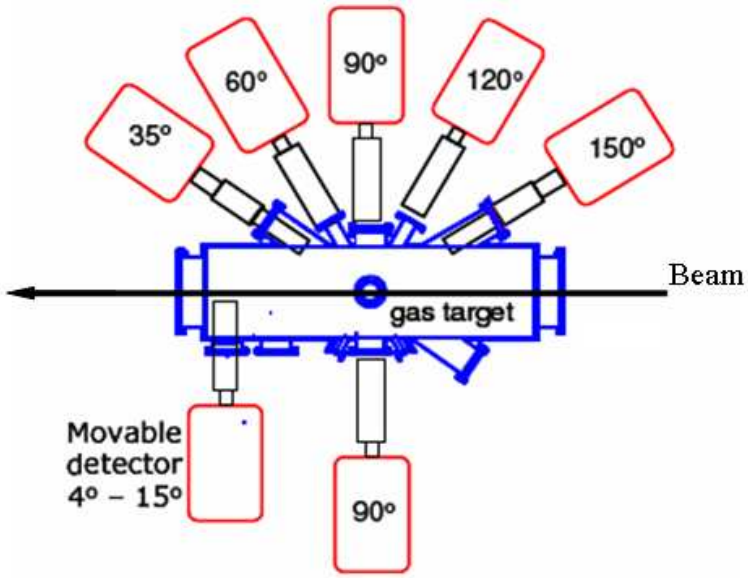

Figure 3.7: Layout of the experimental arrangement at the internal jet-target. X-ray detectors view the target interaction zone at observation angles in the range between ≈4°, and 150°. The movable detector allows to cover detection angles close to zero. All detectors are separated from the UHV system of the storage ring either by 50 μm thick stainless steal or by 100 μm thick Be windows [141].

where λ denotes the charge exchange rate, ρ is the areal density of the gas-jet target in units cm^{-2}, and f is the revolution frequency of the circulating ion beam.

The jet target is equipped with a specially designed experimental scattering chamber (*see figure* 3.7) which allows measuring simultaneously the X-ray emission at different observation angles. This setup is especially suited for angular distribution studies of atomic photon emission precesses involving high-Z projectiles. The accessible angles are ≈ 4°, 35°, 60°, 90°, 120°, and 150° with respect to the beam axis [141, 142]. All detectors are separated from the UHV system of the ESR by a thick (50 μm) stainless steel or (100 μm) Beryllium windows.

The basic principle of charge exchange experiments at the ESR gas-jet target is shown on figure (3.8), where ions after an electron capture or ionization are deflected by the first ring dipole magnet downstream of the jet target zone towards particle detectors. For this purpose, position sensitive multi-wire

proportional counters (MWPC) are mounted horizontally inside and outside of the central trajectory which allows one to measure accurately the position of the up- or down-charged ions on the detector with a detection efficiency close to 100% [143]. It is noteworthy that this works only in the case of high Z projectiles. The radius r of the trajectory of an ion moving in the magnetic field B of the dipole magnet is related to its charge state q as

$$r = \frac{p}{qB} \tag{3.3}$$

where p is the momentum of the ion. This leads to the result

$$\frac{\Delta r}{r} \propto \frac{\Delta q}{q} \tag{3.4}$$

which in turn implies that at small $\Delta q/q$, i.e. high Z, the trajectories for the charge exchanged projectiles, $(q-1)$ and $(q+1)$ are slightly deflected and several charge states can emerge from the dipole magnet towards the particle detectors while for large $\Delta q/q$, i.e. low Z, the charge exchanged projectiles, $(q-1)$ and $(q+1)$ are highly deflected and never get to the MWPC but hit the wall at both sides inside the ring dipole magnet.

3.4 The Extended Reaction Microscope

Recoil-ion and electron momentum spectroscopy (RIMS) is a rapidly developing technique that has been developed [110, 111, 112, 144, 145] to provide an efficient and precise experimental tool to explore the correlated dynamics of collision-induced atomic many-particle reactions in a kinematically complete fashion by measuring simultaneously the final-state vector momenta, and thus angle and energy, of all involved collision fragments: recoil ions, scattered projectiles and ionized electrons.

In the recent past, essentially since less than two decades, the field of RIMS was revolutionized from the experimental point of view by the invention of the many-particle momentum imaging and projection machines, the so-called reaction microscopes [144]. Historically, reaction microscopes have emerged from recoil ion momentum spectroscopy. Since the first recoil-ion momen-

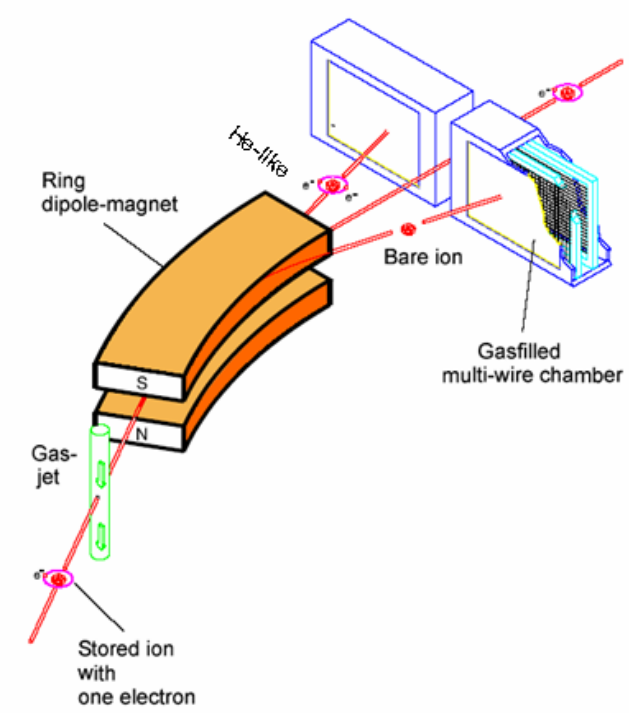

Figure 3.8: Principle of charge-exchange experiments at the internal jet target of the ESR storage ring illustrated for the case of stored H-like ions. The primary beam of stored ions at charge-state q crosses a perpendicularly oriented molecular or atomic supersonic gas beam. The ring dipole magnet serves as a magnetic spectrometer for changes of the magnetic regidity, here electron capture (q-1) and ionization (q+1) [143].

tum measurements by Ullrich and Schmidt-Böcking [107, 146, 147, 148], reaction microscopes are continuously developed through the integration of target preparation, projection techniques and detector development [149, 150, 151] which leads to today's reaction-microscopes developed by Moshammer *et al* [111, 152] and Ullrich *et al* [153].

Reaction microscopes have made it possible to measure the vector momenta of several fragments as ions, electrons, molecular ions with large solid angles, often reaching one hundred per cent of 4π, exceeding those of conventional methods by many orders of magnitude, at extreme precision: momentum resolutions typically around a few per cent of an atomic unit ($a.u.$) and energy resolutions below 1 meV for slow electrons [144].

Reaction microscopes are based on extracting recoil ions and electrons created in the interaction volume between a localized gas target with small momentum spread (*see section* 3.5.1) and the ion beam and project them onto large area position-sensitive channel plate detectors equipped with structured anodes for position decoding. By measuring the times of flight and the impact positions of the recoil ions and electrons on the detectors, their trajectories can be reconstructed and the complete starting momentum vectors can be calculated.

As mentioned previously (*section* 2.5), as a result of the ionization of n_T target electrons and n_p projectile electrons, always there will be $N = n_T + n_p + 2$ fragments in the final state for ion impact (2 *stands for the two parent nuclei*) and a total of $n = n_T + n_p$ electrons released to the continuum. Due to momentum and energy conservation, the collision kinematics is fully determined if $3N - 3$ linear independent scalar momentum components are measured in kinematically complete experiments. For example, in the case of simultaneous target and projectile single ionization (n_T=1, n_p=1, $N = 4$) fully differential cross sections can be extracted if 9 independent momentum components are measured.

Recoil ions are detected in reaction microscopes with near 4π solid angle detection efficiency by means of an electrostatic field, while an additional weak homogenous magnetic field is required in the case of electrons for efficient detection. The magnetic field is generated by a pair of Helmholtz coils

and superimposed along the reaction microscope axis and used to effectively confine the motion of electrons in space and to force them to travel on spiral trajectories from the reaction volume to the detector.

In the various reaction microscopes used so far for charged particle impact, collision energies available are below $\approx 4\ MeV/u$ and mapping both the fast high energy electrons resulting from projectile ionization and the slow low energy electrons resulting from target ionization onto the same detector still results in an acceptable momentum resolution (*see section* 3.5.7). However, for collision energies above $\approx 4\ MeV/u$; $E_{electron} \approx 2\ keV$, it is not practical to map the fast and the slow electrons onto the same detector. To extend the near 4π electron imaging to the projectile continuum, an independent magnetic spectrometer was necessary, for high energy experiments, which guides fast electrons emitted into a narrow cone around the beam direction onto a position sensitive detector and which allows to reconstruct the initial momenta of fast electrons emitted in ionization and capture processes.

Presently, we have implemented a magnetic forward electron spectrometer in the ESR at GSI which is dedicated to 0° electron spectroscopy in collisions of stored ions with gaseous and cluster targets at the supersonic jet target region (*for details see section* 3.6). When jointly operated with the reaction microscope, the forward electron spectrometer will expand the possibilities of the reaction microscope for kinematically complete experiments with relativistic ions in the ESR. It is planned to implement a reaction microscope in the ESR in the close future, until then we used the forward electron spectrometer to study charge transfer to continuum cusps and their relation to the electron-nucleus bremsstrahlung. At the same time, the reaction microscope was commissioned using ionization studies at the UNILAC (*see section* 3.5).

Using the combination of the forward electron spectrometer with the reaction microscope (*see figure* 3.9) in the future will make significant contributions to our understanding of the dynamics of ion atom collisions. The interplay between both instruments will enable for the first time fully differential measurements for:

1-Single and multiple ionization of target and projectile in collisions of relativistic highly-charged ions with atoms.

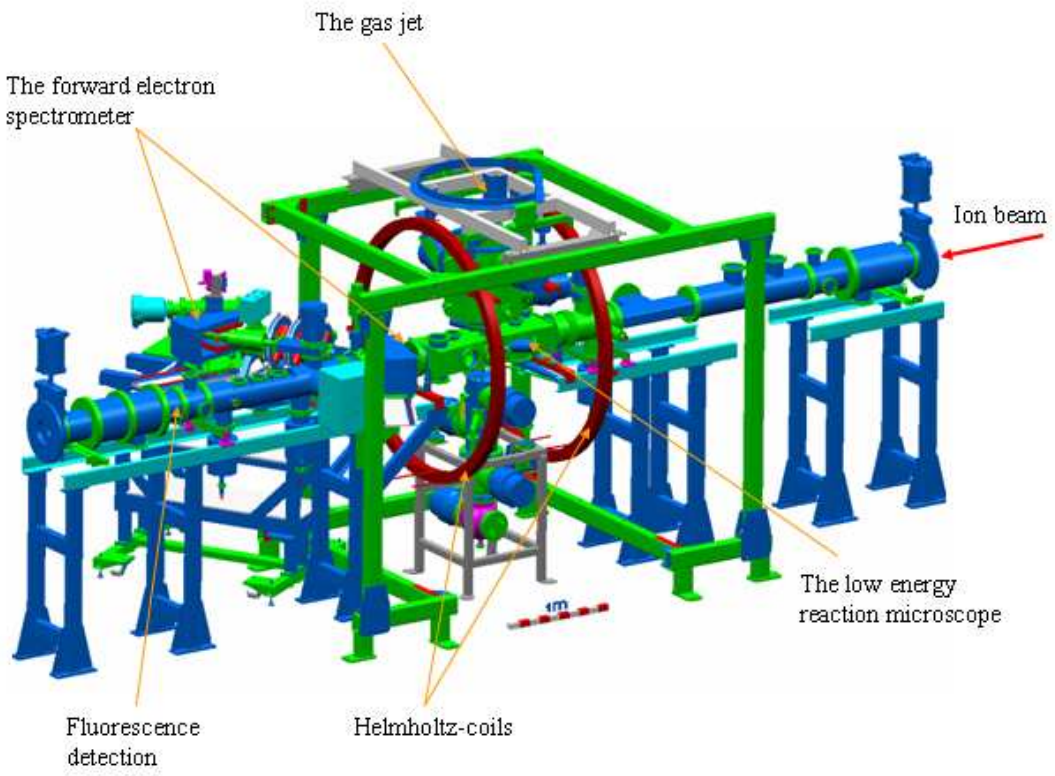

Figure 3.9: Schematic drawing of the extended reaction microscope in the supersonic jet target zone of the ESR storage ring at GSI [154].

2- Electron impact ionization and excitation (e,2e) of projectile ions in arbitrary charge states.
3- Recoil ion and electron momentum spectroscopy at relativistic energies.
4- Emission of electron-nucleus bremsstrahlung via inverse kinematics using cusp electron x-ray coincidence.

In the following sections we give a detailed description of the main parts of the extended reaction microscope.

3.5 Reaction Microscope for Recoil Ions and Low Energy Electrons

In the literature, vertical and longitudinal extraction reaction microscopes were used to investigate electron and ion-impact reactions, laser induced fragmentation, and the interaction of photons with atoms and molecules. The GSI longitudinal reaction microscope used in this work is described schematically in figure (3.10). A well collimated beam of localized gas target, atoms or molecules provided by a supersonic gas jet is crossed with a projectile beam of any kind. The cross-over defines the effective interaction target volume. The interaction target volume will be defined as the geometrical overlap volume between the target and the projectile beams. An electric extraction field parallel to the beam direction is applied in the target zone in order to guide ionized electrons from the small interaction target volume towards a position-sensitive detector. The same electric field will guide recoil ions along the projectile beam in the opposite direction and project them onto another position-sensitive detector in the opposite side.

The extraction field is generated by two parallel 5 mm thick ceramic plates each 220 mm long and 200 mm wide. The two plates are placed 70 mm from each other. Each plate has a hole 16 mm in diameter for the incoming and outgoing atomic beams. Each ceramic plate is plated with two burned-in resistive layers on the side facing the opposite plate. Two resistive areas on each plate are provided. A 5 mm outer rim with a specific resistance of about 20 $k\Omega/cm$ and the inner area with 14 $M\Omega/cm$. By adjusting the potentials with a maximum 5 kV due to resistive heating at the four corners of each plate the ions can be easily steered in the transverse, longitudinal, or any other direction [152]. A further advantage of this configuration is that the offset downward velocity of the ions from the gas jet (*see equation* 3.15) can easily be compensated by steering the ions back upward to the center of the channel-plate detector by applying a weak upward electric field. This can be done easily by setting the voltages at the upper and lower plates slightly asymmetric. For example, instead of using -40 V on both plates, we have used in our experiment a voltage of -42.2 V at the upper plate and a voltage

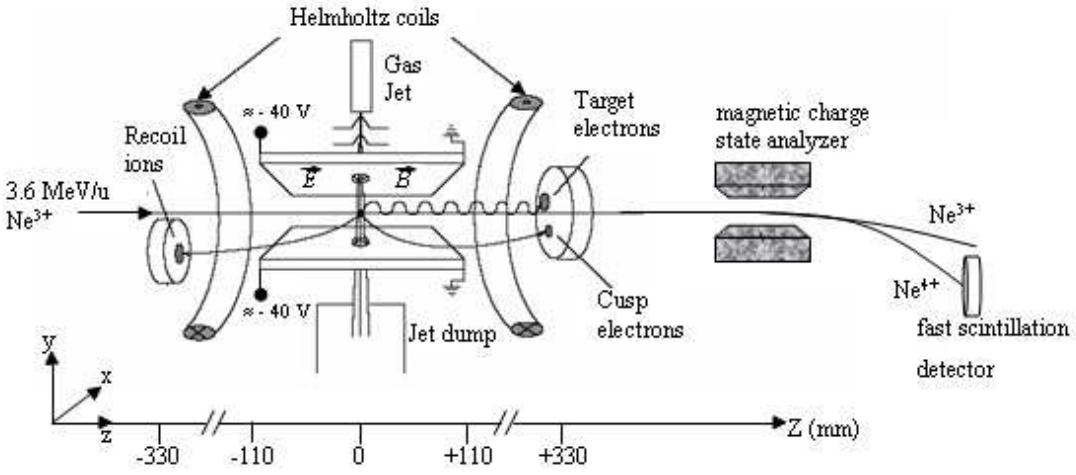

Figure 3.10: Schematic drawing of the GSI reaction microscope as have been used for the study of 3.6 (MeV/u) $Ne^{3+} + Ar \Rightarrow Ne^{4+} + Ar^{q+} + e^-_{fast} + e^-_{slow}$

of $-41.7\ V$ at the lower plate which generates an upward electric field of $\approx 0.07\ V/cm$.

The extraction region is followed on either side by a field-free drift region. Therefore, slight field inhomogeneities appear at the transition from the acceleration region into the field-free drift region causing lens effects in the mapping of recoil ion transverse momenta. The effect of this extraction field inhomogeneity is that principally the ion time of flight does not depend on the longitudinal momentum $p_{||}$ alone but becomes a function of both the longitudinal momentum $p_{||}$ and the transverse momentum $p_{\perp}$. Thus, the ion momentum resolution can be optimized by improving the electric field homogeneity over the spectrometer volume traced out by the ion trajectories. However, since recoil ions already gained the full extraction potential at the transition they are rigid enough to pass this region with only minor deflection. The trajectories of typical collision induced recoil ion transverse momenta of less than 2 $a.u.$, however, are only about 3 mm away from the central trajectory with $p = p_{jet}$ at the end of the potential plates [152]. Thus, these lens effects are estimated to be extremely small and do not measurably decrease the momentum resolution of $\Delta p_{\perp} = 1.54\ a.u.$ in the transverse direction and their influence on the recoil ion time of flight (*longitudinal momentum information*) is very small

compared to the uncertainty $\Delta p_{||} = 0.4\ a.u.$ resulting from other sources. For the detailed discussion of the momentum resolution see section (3.5.7).

Further improvement of the recoil-ion transverse momentum resolution can be achieved by using a grid in front of the detector to shield the field-free drift region from the postacceleration field (*typically* 1 kV/mm) in front of the ion detector which will in turn reduce the field inhomogeneities at this transition region. The individual pores of the grid may act as strong lenses restricting the achievable position resolution for such low-energy ions to the mesh width. Field inhomogeneities expected around the plate-holes due to the close lying ground of skimmer, chamber, and jet-dump have been reduced to negligibly small values by applying correction potentials (~ 20 *volt*) at the outer part of both plate holes.

In order to eliminate the influence of the target extension on the longitudinal momentum resolution, the drift path length was chosen to be 220 mm, twice the acceleration length of 110 mm. The exact ratio of 1 to 2 between the length of acceleration and drift region assures that ions starting with the same initial longitudinal momentum but at slightly different positions in the interaction target volume arrive at the same time at the detector. This is called time-focusing condition [155]. This way, the uncertainty in the determination of the longitudinal momentum due to the finite target extension along the beam is reduced so drastically that it is completely negligible. Similarly, in order to eliminate the influence of the target extension on the transverse momentum resolution a position-focusing have been developed. This position-focusing means that ions starting at different positions in the target zone are focused onto a single spot on the detector while the displacement on the detector is still proportional to the initial momentum. To achieve position-focusing a weak electrostatic lens is implemented into the acceleration region, preferably as close as possible to the reaction-zone while the detector is placed in the focal point of the lens. In general, the implementation of a lens requires a longer drift region compared to a spectrometer with homogeneous fields. Adapting position-focusing, the resolution is no longer limited by the source extension but by the imaging properties of the spectrometer. For more details about position-focusing see [108, 155]. Such focusing conditions are indispensable

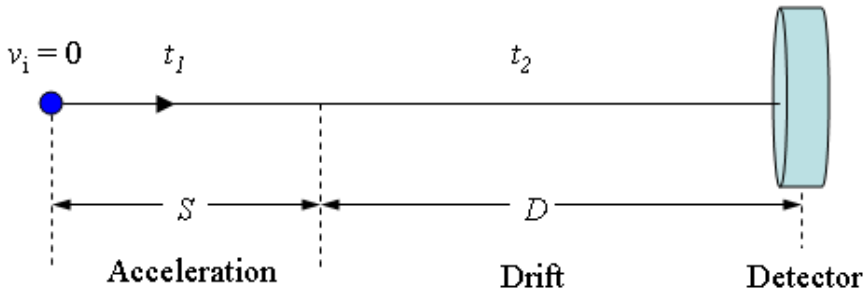

Figure 3.11: Geometrical representation of the acceleration and drift regions of the path of the recoil ions in the reaction microscope.

since one wants to resolve recoil ion energy differences of far below 1 meV, where the typical width of the target of 1 mm would already corresponds to 30 mV difference in the starting potential [156, 157]. The relation between the length of the drift region and the acceleration region has been derived as follows: the time of flight (t_s), in which an ion with zero initial longitudinal momentum can cross the acceleration distance of length (S)(*see figur*e 3.11), is given by

$$t_s = \sqrt{\frac{2S}{a}} \tag{3.5}$$

where a is the acceleration of the ion. And the time of flight (t_d) it needs to cross the drift region of length (D) is given by

$$t_d = \frac{D}{\sqrt{2Sa}} \tag{3.6}$$

Therefore, the total time of flight (t) of the ion till it reaches the detector is the sum of these two times of flight, i.e.

$$t = t_s + t_d = \sqrt{\frac{2S}{a}} + \frac{D}{\sqrt{2Sa}} \tag{3.7}$$

Now, the time of flight of the ions which start from different positions in the interaction target volume with the same initial longitudinal momentum should be independent on the start position. This means

$$\frac{\partial t}{\partial S} = 0 \tag{3.8}$$

The differentiation leads to a condition for the ratio of acceleration to drift distances

$$D = 2S \tag{3.9}$$

which is the actual situation chosen for the GSI reaction microscope used in this work ($D = 2S = 220\ mm$). No electrostatic fields are applied in this reaction microscope for the position-focusing of the transverse momentum components.

For atomic reactions involving outer-shell ionization of target atoms (*present work*) characterized by impact parameters in the order of outer-shell radius, recoil-ions emerge with kinetic energies of some meV or below [158] corresponding to a momentum transfer of few atomic units. Therefore, extraction fields of a few V/cm are generally sufficiently high to achieve a 4π solid angle collection efficiency with typical detector sizes of about 50 mm diameter. However, emitted electrons have usually considerably larger kinetic energies making it much harder to collect them. Most of them simply miss the detector. In order to achieve a high acceptance together with a good resolution for both electrons and recoil-ions in coincidence, a weak homogenous magnetic field is superimposed along the reaction microscope axis and used to effectively confine the electron motion in space perpendicular to the beam direction and force them to travel on spiral trajectories from the reaction volume to the detector. This technique has already been widely used in the last few years [111, 153, 152, 159].

The magnetic field needs to be homogenous around the target area including the recoil and electron detectors. It is generated by a pair of large Helmholtz coils. By adjusting the distance between the coils equal to their radius a sufficiently homogeneous magnetic field can be achieved in a quite large spatial region. The Helmholtz coils used in our reaction microscope are 2 m in diameter and each contains 16 *turns*. By varying the current in the coils, the magnetic field can be adjusted to confine electrons up to a certain momentum perpendicular to the field, 1.8 *a.u.* in the present work with 80 mm diameter electron detector. In the course of the present work, the coil current values are

in the range (0 - 100 A) which correspond to magnetic filed values in the range (0 - 14 *Gauss*). Under the operating conditions of the present experiment, a magnetic field B of 11.5 *Gauss* was used (I = 80 A). This field results in an electron revolution time T of

$$T = 2\pi \frac{m_e}{e\ B} = \ 31\ nsec. \tag{3.10}$$

which is the same for all electrons regardless of their energy. In equation (3.10), m_e and e are the electron mass and charge respectively. With an active MCP detector area of 80 *mm* diameter this will yield 4π solid angle for electrons up to an energy of about 45 eV. The magnetic field is slightly tilted horizontally by 10.5° with respect to the direction of the ion beam to guide electrons of zero initial transverse momentum out of the projectile ion path onto the detector. This way, electrons emitted with zero transverse momentum hit the detector close to the middle of its active area.

In the course of commissioning the reaction microscope for implementation into the ESR, we have begun to use, first at low collision energies, the reaction microscope for kinematically complete investigations. Here, we present a study of the simultaneous target and projectile ionization for the collision of Ne^{3+} ion beam with an argon target. In such a process, electrons ionized from the target will appear in the laboratory frame with low energy as slow electrons, while electrons ionized from the projectile will have very small energy in the rest frame of the projectile but will appear in the laboratory frame with high energy as fast electrons corresponding to electrons moving with the projectile velocity.

3.6 (MeV/u) $\ Ne^{3+} + Ar \Rightarrow Ne^{4+} + Ar^{q+} + e^-_{fast} + e^-_{slow}$

The experiment was performed using a 3.6 MeV/u stripped and charge state analyzed Ne^{3+} beam from the UNILAC of GSI. The beam was collimated to a size of about 1.2 $mm \times 1.1$ mm ($horizontal \times vertical$) in the target region. The charge state was analyzed after the collision and ionized Ne^{4+} projectiles were recorded by a fast scintillation detector at a rate of up to 1 *MHz*. A double stage supersonic jet provided a well localized argon target (*see experimental*

results in section 3.5.8).

The whole reaction microscope is constructed to be UHV (*Ultra High Vacuum*) compatible in order to be implemented in the ESR storage ring (*bakeable up to 300 °C*). A detailed description of the main parts of the reaction microscope is given in the following subsections.

3.5.1 The Target

High resolution recoil ion momentum spectrometry requires a very low initial momentum spread ($\Delta p < 1$ *a.u.*) of the target, which became possible with the use of supersonic gas-jet targets. For example, when the argon gas is treated as mono-atomic ideal gas, atoms are point-size, gas is low-density, elastic collisions are the only interactions, the average thermal energy per atom at room temperature (≈ 300 *K*) according to thermodynamics is

$$E_{therm} = \frac{3}{2}kT = 39\ meV \tag{3.11}$$

where (k: Boltzmann constant 8.617×10^{-5} eV/K), which corresponds to a momentum per atom of

$$p_{therm} = \sqrt{2mE_{therm}} = 14.4\ a.u. \tag{3.12}$$

this means that the argon atom at room temperature has already such a large initial momentum spread that typical momenta of the recoil argon ions gained in the atomic collisions, typically less than 3 *a.u.* [17, 111] are covered by the argon thermal motion. For this reason, the measurement of the momentum of the recoil ion was not seriously exploited as an alternative high-resolution spectroscopy technique in ion-atom collisions before the development of supersonic gas-jets [160].

Supersonic jets provide a dense, well localized and internally cold gas targets which makes them ideally suited for recoil ion momentum measurements. In supersonic gas-jets, a gas under high pressure is allowed to expand through a very narrow nozzle into a vacuum chamber. During the expansion the gas cools down from the temperature of the gas source ($T_\circ$) to some temperature $T \ll T_\circ$. Ideally, this expansion causes the free enthalpy

$$H = E_{therm} + kT_\circ = \frac{5}{2}kT_\circ \tag{3.13}$$

of the gas to be converted into directed kinetic energy and thereby the gas flow is accelerated to a supersonic speed [161]. After the expansion, an atom of mass m_R will have a momentum in the expansion direction = jet direction of

$$p_{jet} = \sqrt{5km_RT_\circ} \tag{3.14}$$

and a velocity of

$$v_{jet} = \sqrt{\frac{5kT_\circ}{m_R}} \tag{3.15}$$

Ideally, all atoms have this velocity with negligible relative velocity with each other. In practice, atoms have velocity distribution around this mean velocity caused by self-scattering and by collisions of the target gas atoms with the residual gas atoms. The width of the velocity distribution around the mean velocity is described by the speed ratio S which reflects the actual quality of the jet and is defined as the mean jet velocity divided by the thermal spread in velocities, the FWHM of the velocity distribution. The speed ratio for an ideal mono atomic gas is given by [162, 163]

$$S = \frac{v_{jet}}{\sqrt{2kT/m_R}} = \sqrt{\frac{5T_\circ}{2T}} \tag{3.16}$$

where T is the leftover internal jet temperature after the expansion which goes towards zero in the ideal case. For all gases at a fixed gas source temperature $T_\circ$ that is sufficiently high to avoid cluster formation the speed ratio is found to vary approximately with source stagnation pressure $p_\circ$ and the nozzle diameter d according to [164]

$$S \propto (p_\circ d)^{1/2} \tag{3.17}$$

Typical values for the speed ratio are in the range $5 \leq S \leq 100$ which corresponds to a final temperature in the range $7.5\ mK \leq T \leq 30\ K$ at a gas source temperature of $T_\circ = 300\ K$ [165].

Several stages with differential pumping are used to handle the enormous gas-load and to maintain a good vacuum in the reaction chamber. The region in front of the nozzle where the expansion is still supersonic is called the zone of silence. A typical value for the spatial extension x_s of this region beyond the aperture is given by [162]

$$x_s = \frac{2}{3}\sqrt{\frac{p_\circ}{p_s}}\, d \tag{3.18}$$

with p_s being the pressure downstream of the nozzle. To extract a geometrically well defined atomic beam with an unperturbed motion a small skimmer aperture must be placed behind the nozzle inside the zone of silence. For more optimization, additional skimmers can also be placed between the different pumping stages. This method was first proposed by Kantrowitz and Grey [166].

In our experiments, a 2-stage supersonic gas jet (*figures* 3.12 and 3.13) is used to produce a geometrically well defined and localized argon target. This supersonic gas jet was produced by allowing the argon gas at a pressure of 10 *bar* and at room temperature ($T_\circ$= 300 K) to expand downward through a 30 μm nozzle into a first vacuum chamber. The nozzle is made of stainless steel and is mounted on a translational stage, which allows for the adjustment of the nozzle position in the plane perpendicular to the atomic beam axis. The nozzle was positioned always at the position that maximizes the pressure at the dump section. After the expansion, the atoms move with a momentum of p_{jet} = 18.6 *a.u.* (*equation* 3.14) which corresponds to an energy of $E_{jet} = p_{jet}^2/2m_R$ = 65 meV and a mean downward velocity of argon atoms of v_{jet} = 560 m/sec (*equation* 3.15). Using the experimental speed ratios measured for various ($p_\circ d$) values by Braun *et al* [167], A speed ratio of about 30 is estimated [165] for the parameters of our jet system. This implies an internal temperature near 0.83 K (*equation* 3.16) which corresponds to an average thermal energy per atom of only 0.11 meV and a momentum spread of $\pm$ 0.76 *a.u.* for argon. The inner jet fraction then passes through a narrow 0.3 mm diameter cone-shaped skimmer into a second vacuum chamber. The pressure in this stage is about 1.1×10^{-5} $mbar$(*see figure* 3.14). The inner jet fraction passes through a second 0.6 mm diameter skimmer into the collision chamber yielding an atomic beam

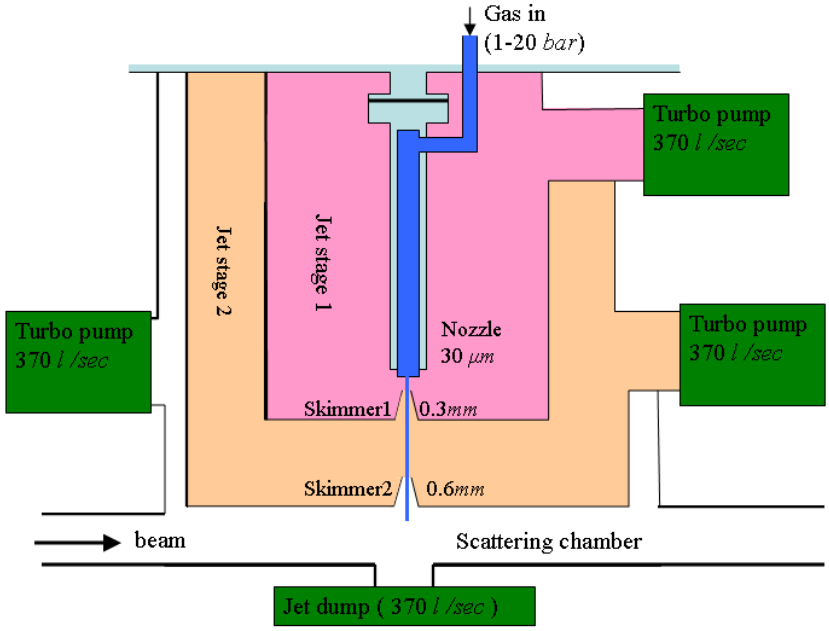

Figure 3.12: Schematic drawing of the 2-stages gas-jet used with the GSI reaction microscope.

with a diameter 3.2 *mm* at the intersection point with the projectile beam. The collision chamber is maintained at a pressure of 1.4×10^{-7} *mbar*(*see figure* 3.14). The target density at the intersection point in the target chamber is estimated to be about 2.6×10^{11} *particle/cm*^{3} which should be compared to the residual gas density of $\approx 10^9$ *particle/cm*^{3} (*background contributes only* $\approx 1\%$ *to the total target density*). Finally, the gas jet leaves the scattering chamber through an opening on the opposite side of the target chamber into a jet dump pumped by a separate turbo pump to reduce the argon residual gas pressure.

3.5.2 The Electron Detector

For time of flight (TOF) electron spectrometry with simultaneous vector momentum identification in our reaction microscope, a position sensitive detector (PSD) which combines good position resolution (*typically 0.1 mm*) with good time resolution (*typically 1 nsec.*) for singly arriving particles at high particle flux and for particle showers (*multi-hits*) was essential. For this purpose we have constructed a micro channel plate (MCP) detector with delay line po-

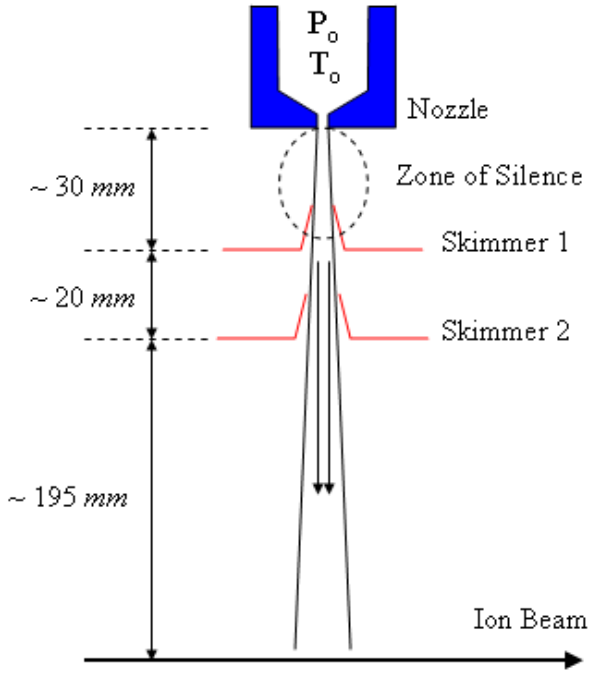

Figure 3.13: Schematic drawing of the gas-jet dimensions.

sition encoding anode (*figure* 3.15). For a more complete overview on MCP detectors see [151, 168]. The concept of such design is to decode the position and arrival time of a particle by electronic pickup of the particle-triggered electron avalanche exiting the MCP stack on a specially designed delay line anode.

The following brief description shall give an overview of the detector used in our reaction microscope and its advantages and limitations

The Micro Channel Plates

Three rimless channel plates of 80 *mm* diameter and 1.5 *mm* thickness are used in the electron detector, supported by a pair of partially metallized ceramic rings. Microscopically, a MCP consists of a dense stack of millions of individual electron multiplier tubes, each having a diameter of typically 10 μm. The distance between the tubes is only a little bit bigger than the tube diameter. The inside of the tubes is covered with a semi-conducting layer that tends to emit secondary electrons under the bombardment of primary energetic particles (*electrons or recoil ions in our case*). By biasing the MCP electrodes

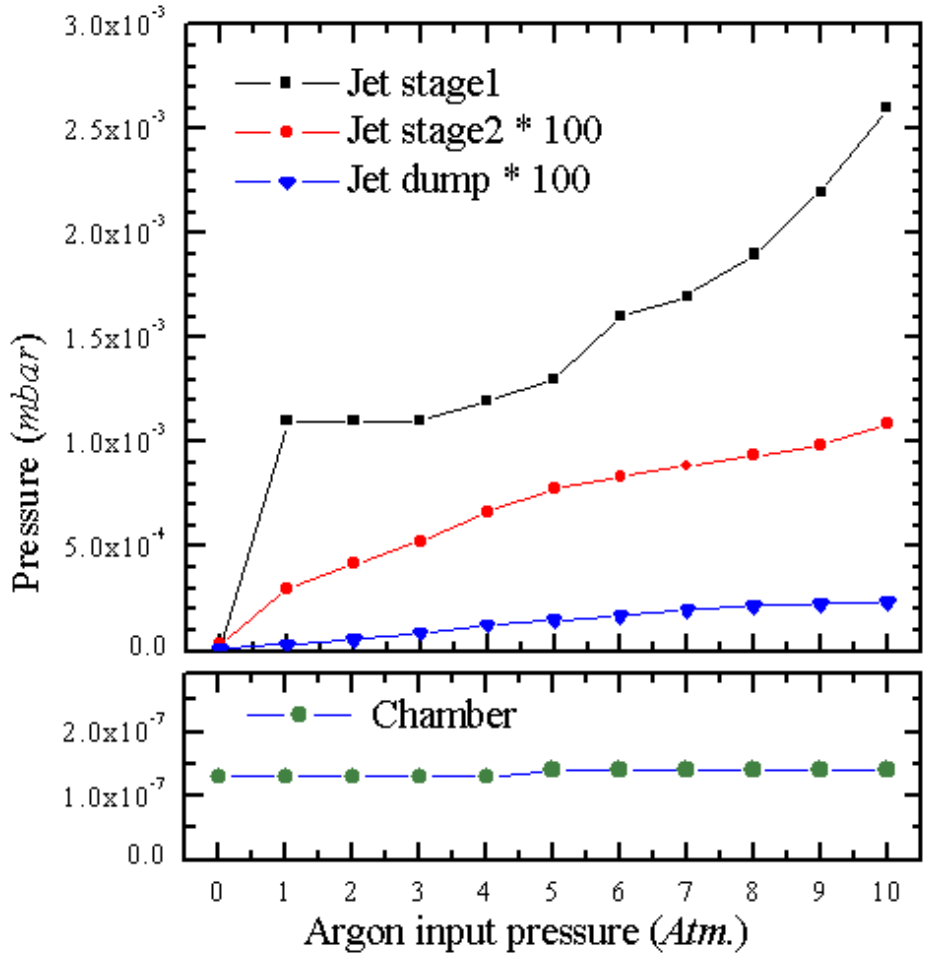

Figure 3.14: The measured pressure profile of argon at the different stages of the jet. The residual gas offset is subtracted. Values for the pressure in jet stages 1 and 2 are multiplied by 100. Note the increase in jet-dump pressure with increasing pressure in jet stages 1 and 2 while the corresponding pressure in the target chamber (*lower part*) remains unchanged.

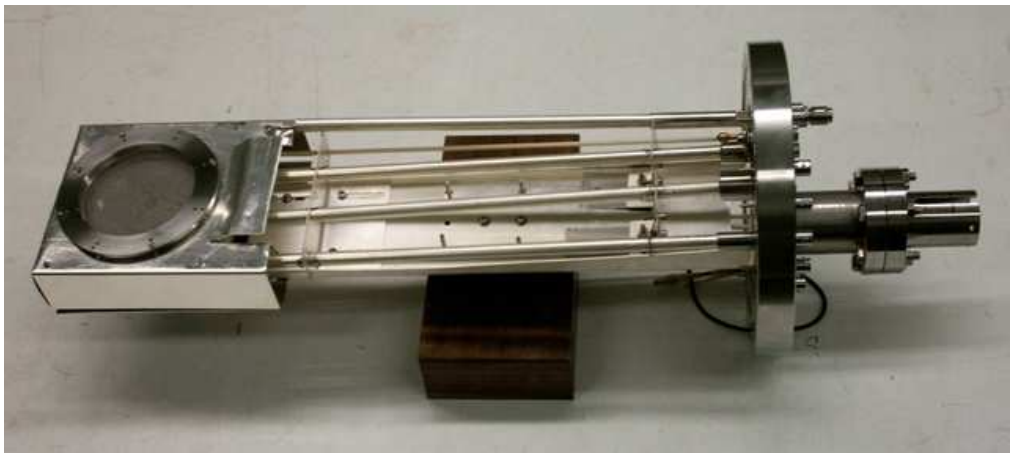

Figure 3.15: The position sensitive electron detector with a delay line position encoding

with a high voltage (*typically* 1 kV), each of the secondary electrons gains enough kinetic energy to liberate more electrons when it hits the wall. An avalanche of electrons is forming along the tube and finally exiting the pore. The duration of a single MCP pulse is of the order of $10^{-9} sec$ and it may appear that a single MCP channel could deliver around 10^9 distinguishable pulses per second. But, the firing of a MCP channel represents a sudden discharge and the channel needs a certain time to recover (*recharging in the channel wall*). Typically, the recharge time is about $10^{-2} sec$ which means that the maximum pulse rate which can be delivered by a single MCP channel is therefore of the order of $\leq 10^2\ s^{-1}$.

The MCP's of the electron detector used in this work are arranged in a Z stack configuration (*figure* 3.16) which is a commonly used method of obtaining high gain ($10^6 - 10^7$) output pulses. In Z stack configuration, channel axes are biased at a small angle ($\sim 8°$) to the MCP input surface and the plates are oriented with respect to each other so that the channels slope in opposite directions which provides sufficiently large directional change so as to inhibit positive ions produced at the output of the rear plate from reaching the input of the front plate (*ion feedback*). The Z stack configuration also exhibits high saturated gains because of the multiplicity of channels excited in the back MCP by a single channel in the front MCP.

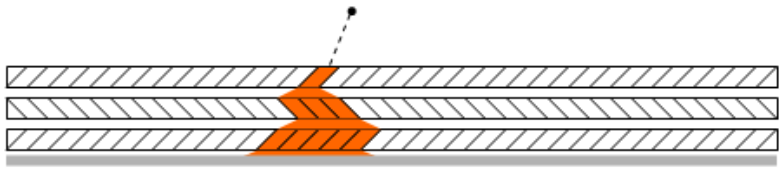

Figure 3.16: Schematic drawing of 3 MCP's assembly in a Z-stack configuration

The MCP's of the electron detector used in this work are operated with a relative bias voltage $\sim 2.4\ keV$. The bias voltage is applied slowly (*50 V/sec*) in order to avoid damage to the electronic modules connected. A grid is mounted in front of the first MCP and a small bias negative voltage (-20 *V in this work*) is always put on the grid to repel stray electrons which are mostly very slow electrons. The grid is made from stainless steel wire 0.03 *mm* in diameter with mesh size 0.478 *mm* which corresponds to 88% geometrical transmission. Due to the presence of the electric field which penetrates through the grid, we expect the optical transmission of electrons to be larger than this value.

The Delay Line Anode

A delay line anode, (*first suggested by Sobottka* [150]), manufactured by **roentdek** [169] was chosen as a read out for our detector because commercial CCD systems lack the timing information whereas other electronic MCP readout schemes usually suffer from low acquisition rate and complicated read out electronics. The delay line method allows to exploite simultaneously: high position resolution, high speed and high timing precision (*see section* 3.5.7). The delay line method can also cope with particle showers (*multi-hits*) if combined with multiple stop/start time to digital converters (TDC). Coincidence technique also can be easily implemented.

The delay line anode used in our detector is composed of two crossed double wire planes spirally wound over a copper plate in both x- and y-directions where they are held with ceramic holders fixed on the edge of the copper plate in order to isolate the wires from one another and from the copper plate (*figure* 3.17). The distance is about 1 *mm* between wire planes and 1 *mm* between the copper plate and the near wire plane [151]. Each wire plane consists of a pair of wires with nearly 0.5 *mm* distance to separate them from each other. By a potential

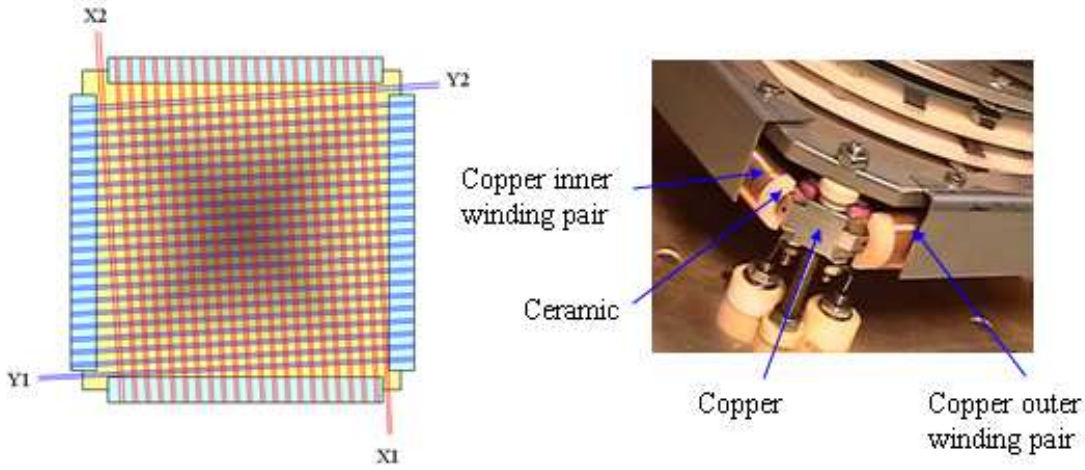

Figure 3.17: Delay-line anode for multi channel-plate position read out. The inner and outer winding pair are for X and Y encoding. The two wires of each pair are on different potential such that the electrons are collected on one of them.

difference of (50 - 100) volts between the two wires, the electron avalanche produced by an electron hitting the channel plates is collected by one of the wires. The wire pair acts as a lecher cable. At both ends of the double wire spiral, the signals are processed by a differential amplifier. Both wires pick up the same capacitively coupled noise, but their signals differ by the real electrons from the charge cloud collected by the more positively biased wire.

The principle of this design is to measure the delay that a signal experiences traveling on the spiral transmission line. A signal induced somewhere on the delay line from a single charge cloud will propagate towards the four ends. Each signal produced is picked up for further processing from the four anode contacts, two for each dimension and from the MCP contact. For each dimension, the corresponding ends of the delay line are located on the opposite corners of the array and the respective position is directly proportional to the time difference (t_1 - t_2) between the arrival times at the two ends of the line measured with respect to a time zero which is in our case the moment when an electron hits the MCP stack and gives rise to a signal at the MCP. The time sum ($t_1 + t_2$) is a constant for all positions and equals the transmission time of a signal over the whole delay-line anode, after subtracting additional

cable delays.

The absolute position resolution of the delay line is limited by the timing accuracy of the TDC, while the relative position resolution is only limited by the digital range of the TDC and not by the signal to noise ratio.

The four wire pairs from both delay line ends of each dimension are connected from the corner contacts of the anode to a CF35-12-pin-feedthrough flange by a pair of parallel wires 0.1 *mm* in diameter running inside a double-hole ceramic rod of 1.4 *mm* separation between the holes. this geometry corresponds to a lecher cable with impedance

$$Z = \frac{120}{\sqrt{\epsilon}} \ln(\frac{D}{r}) \approx 140\ \Omega \tag{3.19}$$

where ϵ is the dielectric constant of the material between the two wires (*ceramic*), r is the wire radius, and D is the wire separation. We have found that this specific geometry of the anode signal transmission lines will result in the best impedance matching and will produce the cleanest anode signal shapes.

The read out of the delay-line anode signals requires differentially amplifying and constant fraction timing circuits. For this purpose a **roentdek** [169] type **DLATR6** module matched to our anode from the same manufacturer is used. The **DLATR6** module consists of a 6-fold differential amplifier with integrated constant fraction discriminator (CFD) circuit for each amplifier channel. The **DLATR6** module is connected to the delay line signals via the CF35-feedthroughs by a special 8 pin cable.

The Transmission Lines

The design criteria of the reaction microscope requires the electron detector to be able to move away from the measuring location when no experiment is performed or during the beam optimization process before starting the data acquisition. This technical problem is solved by mounting the detector inside a movable spring bellow carried by a holder controlled electrically by a special motor. From the geometry of the reaction microscope, this requires the MCP's to be $\sim$40 *cm* away from the vacuum feedthroughs. For this reason, the front and back faces of the MCP's are connected to the impedance matched vacuum feedthroughs via specially designed transmission coaxial lines consisting of two 40 *cm* long coaxial stainless steel pipes of inner and outer diameters of 3 and 9

mm respectively with the space between them filled with ceramic (Al_2O_3) pipe of inner and outer diameters of 5, and 8 *mm* respectively. Such a design was chosen to be UHV compatible (*bakeable*) and the dimensions were determined using the formula:

$$Z = \frac{60}{\sqrt{\epsilon}} \ln(\frac{R}{r}) \tag{3.20}$$

where Z is the impedance of a coaxial cable, ϵ is the dielectric constant of the material between the inner and outer pipes, R and r are the outer and inner radii of the coaxial cable respectively. The inner pipes of the coaxials are connected to the MCP's using special metal spring clamps inserted between the ceramic rings at positions with metallization contact pad. This design fits with the requirements of ultra high vacuum (UHV) and proved to give the best match of impedance and minimum reflections in the MCP's timing signals (*see figure* 3.18). The shape of the produced timing signals characterized by a FWHM of about 6 *nsec* and a rise time of 5 *nsec* is an analog measure of the ability of the used fast amplifier (*see section* 3.6.4) to respond to fast MCP input signals. The amplifier response is primarily due to a delay in voltage caused by the stray capacitance and inductance in the amplifier until the steady state is reached. The voltages of the anode and the grid are also supplied using the same kind of coaxial conductors.

It is noteworthy that, the timing signal from the MCP of the electron detector is used throughout our work as a common start signal for the TDC, the electron-recoil TAC, and the electron-projectile TAC.

3.5.3 The Recoil Ion Detector

A channel plate detector with wedge-and-strip position encoding has been used in the reaction microscope for the detection of the position and arrival times of recoil ions. A detector with wedge-and-strip read out is shown in figure (3.19). The typical period of the structure is 1.4 *mm*. The electron cloud of about $10^6 - 10^7$ electrons created by avalanche amplification in the channels are accelerated onto a high resistivity germanium layer evaporated onto a 1.5 *mm* ceramic plate [170]. The image charge is picked up on the backside of the

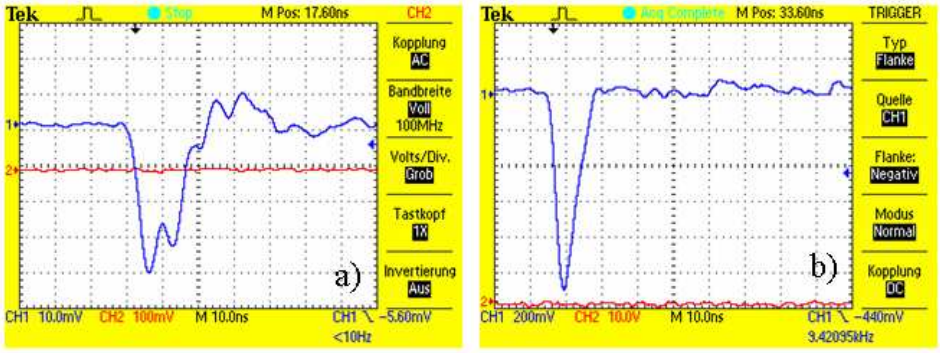

Figure 3.18: Oscilloscope traces of two pulses out of the MCP of the electron detector before(a) and after(b) using the special coaxial transmission lines of 40 *cm* length.

ceramic plate by the three areas of the wedge-and-strip structure. The area of the wedges and stripes grows linearly with the X and Y position, respectively. A proper adjustment of the resistivity and the thickness of the ceramic plate assures that the image charge covers more than one structure. This is essential to allow for a determination of the centroid of the charge cloud. For detailed description of wedge and strip readout see [149].

A stack of two circular micro channel plates of 40 *mm* active diameter (66 *mm outer detector diameter*) arranged in chevron stack and supported by a pair of ceramic rings are used in the detector. The MCP's are mounted 40 *cm* away from the vacuum feedthroughs for the same reason given for the electron detector (*section* 3.5.2) and similar transmission lines are used. The MCP's are operated with a relative bias voltage $\sim 2.05\ keV$ which is applied slowly (50 *V/sec, as in the case of the electron detector*) in order to avoid damage to the electronic modules connected.

The charge signals of the wedge, strip, and meander structures serve to determine the position of the recoil ion; are amplified by charge sensitive preamplifiers and main amplifiers and finally recorded by analog to digital converters (ADC). By normalizing the wedge and the strip signal to the total pulse height one obtains the position of the centroid of the charge cloud (*equations* 3.21 *and* 3.22). The position resolution of the detector is mainly determined by the signal to noise ratio of the three signals. Therefore a good pulse-height resolution and high gain is desirable. For our detector, a position resolution of

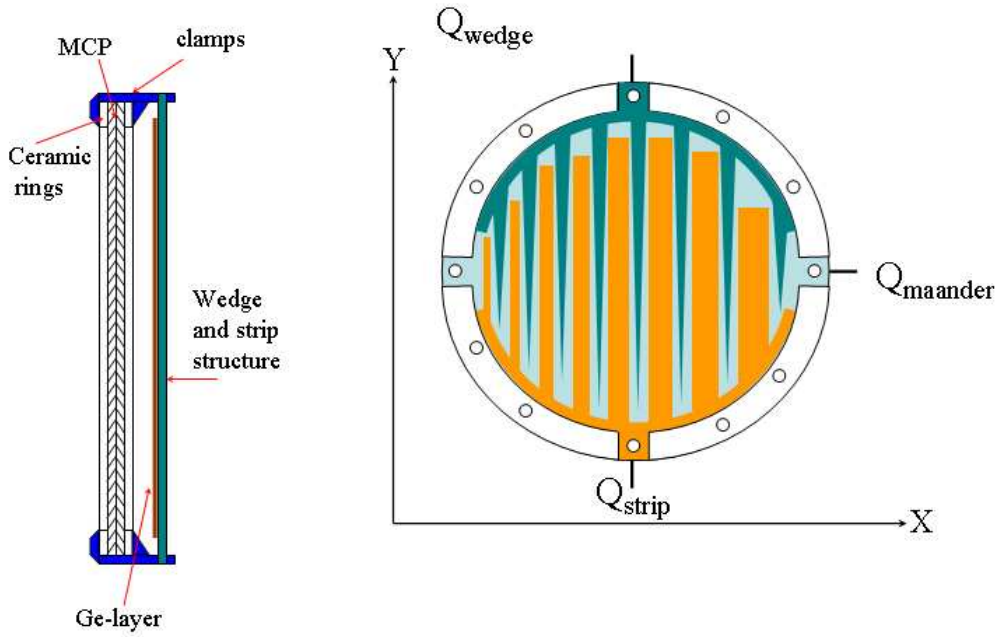

Figure 3.19: Channel plate detector with wedge-and-strip read out

1 *mm* is estimated [17]. The timing information in the detector is picked up from the front side of the channel-plate stack and used as a stop signal for the electron-recoil time to analog converter (TAC). The time resolution is limited only by the electronics used usually to 0.5 *nsec*.

$$X \propto \frac{Q_{strip}}{Q_{strip} + Q_{wedge} + Q_{maander}} \tag{3.21}$$

$$Y \propto \frac{Q_{wedge}}{Q_{strip} + Q_{wedge} + Q_{maander}} \tag{3.22}$$

3.5.4 The Multi-Hit System

In heavy ion induced ionization, more than one electron can be ionized from the target or the projectile simultaneously. A "multi-hit" is an event where more than one particle, here electron, arrives on the MCP in a time period shorter than the read-out time. While the MCP itself responds to such an event with distinct charge clouds for each hit, the delay line detector and the delay line wire system used in our electron detector can in principle detect and

separate the signals of two electrons impinging on the detector in a very short time difference within the limited time resolution of the system if they hit at different positions. Whether the TOF and position for both fragments can be determined depends only on the electronics used.

The LeCroy 3377 multi-hit TDC module we are using for this purpose represents the nucleus of our multi-hit system. This multi-hit TDC has 32 channels and can process 16 hits per channel separated by at least 10 *nsec* in time with a time resolution of 0.5 *nsec*. If two electrons hit the detector within 30 *nsec*, i.e. the total signal processing time on the delay line, the x- and y-delay line signals of the two particles interfere with each other. However, the sum of the corresponding arrival times for each ion on opposite ends of a delay line is constant for a true event because the delay line has always a constant length for each signal pair. This information can be used in the analysis program to sort the signals of all the particles according to their arrival time and thus their position on the detector can be identified.

The delay-line electron detector and the delay-line wire system used in the GSI reaction microscope can in principle detect and separate the signals of two electrons impinging on the detector in a very short time difference (≤ 10 *nsec*) if they hit at different positions.

3.5.5 Detection of Recoil Ions in the Reaction Microscope

Recoil ions created at the intersection point of the gas jet with the ion beam are extracted by a uniform electrostatic extraction field of 1.92 *V/cm* provided over 22 *cm* along the beam (*total voltage applied* $U = -42.2$ *V; potential at the intersection point* $= -21.2$ *V*). After 11 *cm* of acceleration, recoil ions drift over a field free region of 22 *cm* length; this geometry fulfills the condition of time focusing (*equation* 3.9). Recoil ions are then post accelerated onto the channel plates ($\Delta V = -2050$ *V over* 2 *mm*). The electron avalanche exiting the MCP is then detected by the two dimensional position sensitive detector (*wedge and strip anode*) of 40 *mm* active diameter. This detector is mounted directly beneath the straight path of the projectile beam (*see figure* 3.10).

The recoil ion TOF spectrum (*see figure* 3.20) contains two important pieces of information. First, different ion species and different charge states can be distinguished because they appear as well separated peaks in the TOF spectrum due to the dependence of the flight-time on the mass to charge ratio ($TOF \propto \sqrt{\frac{m}{q}}$). Second, the shape of these individual peaks reflects the different starting longitudinal momenta folded with the electronic time resolution function.

To illustrate this, we assume that ions of a certain mass and charge but with zero initial longitudinal momentum appear after a flight-time t_o at the detector. Then, for those ions which emerge with an initial velocity vector pointing toward the detector the measured TOF will be shorter than t_o and vice versa. Since the extraction field in the reaction microscope is homogenous, it is possible to assign to each channel in the TOF spectrum the corresponding recoil-ion momentum parallel to the beam direction using the relation [144]:

$$p_{||} = \frac{qU}{S}(t_o - t) \tag{3.23}$$

where t is the actual TOF and S is the distance over which the ion of charge q is accelerated to an energy of qU. This relation is valid for ions as long as their initial kinetic energy is small compared to qU.

The momentum components perpendicular to the beam axis can be determined from the position distribution (*see figure* 3.20) of counts on the channel-plate ion detector. The transverse recoil ion momentum vector ($p_\perp$) is given by:

$$p_\perp = \sqrt{p_x^2 + p_y^2} \tag{3.24}$$

where p_x and p_y are given in the case of no position-focusing (*present case*) by:

$$p_x = \frac{m\triangle x}{t} \tag{3.25}$$

$$p_y = \frac{m\triangle y}{t} \tag{3.26}$$

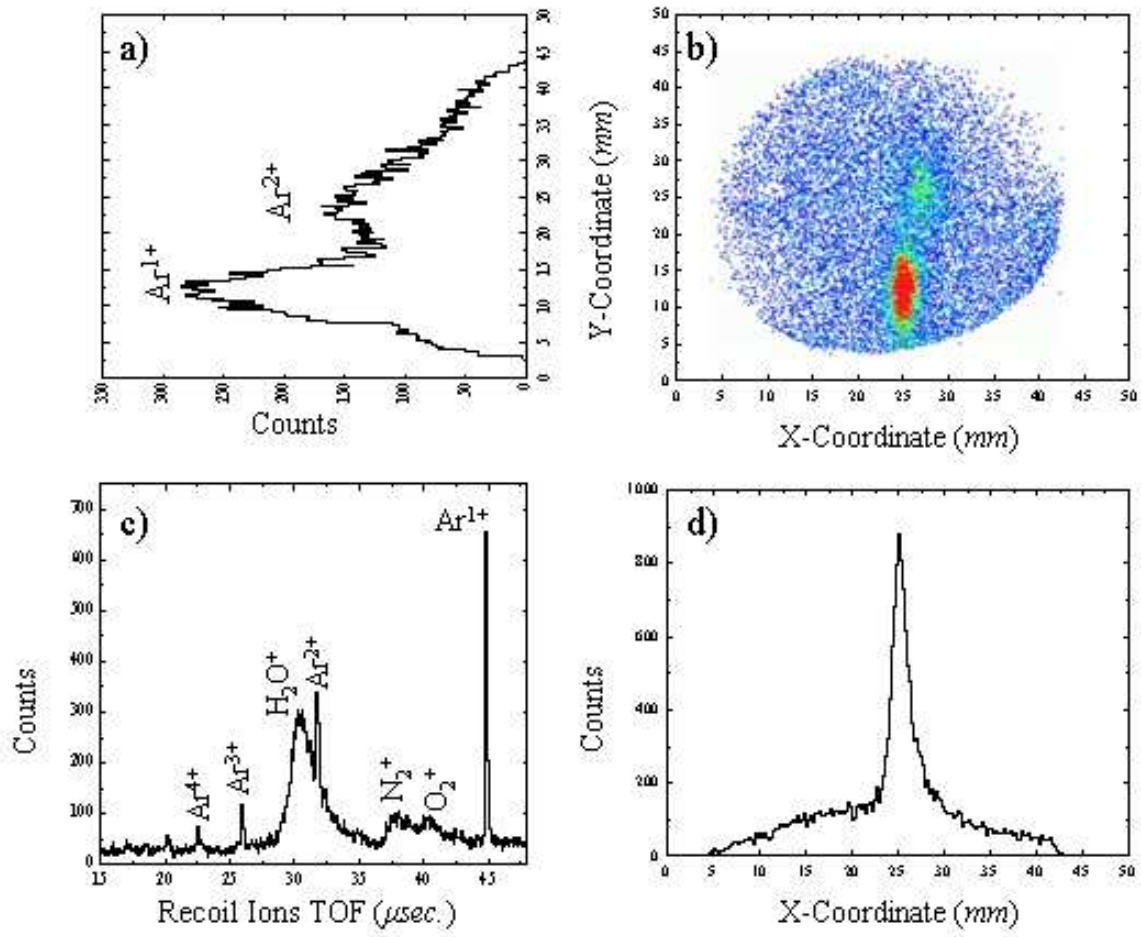

Figure 3.20: Measured spectra for time-of-flight and position of impact coincident with Ne^{4+} for the collision of Ne^{3+} with argon gas target. The start signal of a time to analog converter (TAC) was generated by the detection of an electron by the electron detector, while the stop signal was generated by the detection of an argon recoil ion (Ar^{q+}) by the recoil ion detector. Here, we emphasize that the relative location of Ar^{2+} ions on the 2D spectrum with respect to the location of Ar^{1+} ions is in excellent agreement with that predicted mathematically from the parameters of our measurement.

Ion	Time of flight (TOF) ($\mu sec.$)	Cyclotron time (T) ($msec.$)
Ar^{1+}	45.7	2.48
Ar^{2+}	32.2	1.24
Ar^{3+}	26.3	0.83
Ar^{4+}	22.8	0.62

Table 3.3: Measured times of flight and cyclotron cycle for different argon charge states.

where $\triangle x$, $\triangle y$ are the horizontal and vertical displacements on the detector of the position of impact of the ion with respect to the position where an ion with zero initial transverse momentum would hit the detector. Usually, the downward velocity component of atoms leaving the jet (560 *m/s previously mentioned*) will result in a downward displacement of the zero point. In practice the zero point in the direction of the jet is simply given by the center of the peak, since the momentum distribution is rotationally symmetric around the ion beam.

In conclusion, from both, longitudinal and transverse momentum information for each detected ion, the trajectory can be reconstructed and the initial momentum vector can be calculated unambiguously. Figure (3.20) shows the measured recoil ion spectrum coincident with outgoing Ne^{4+} projectiles obtained by the GSI reaction microscope for the collision of 3.6 MeV/u Ne^{3+} projectile beam with argon gas target. Beside the main peaks of the different detected charge states (*up to* Ar^{4+}) of argon, one can recognize in the time spectrum the quite broad peaks of O_2^+ , N_2^+, and H_2O^+ originating from ionization of the residual gas.

As a result of the presence of the uniform magnetic field of the Helmholtz coils, recoil ions will move on spiral trajectories from the reaction volume to the detector. The cyclotron time of a recoil ion is defined as the time needed for one complete cycle in the applied magnetic field B, which is given by $T = 2\pi\frac{m}{qB}$. Table (3.3) contains the measured times of flight (TOF) in the entire apparatus and the cyclotron times for the different argon charge states.

Since recoil ions are accelerated to a high longitudinal momentum p_z by the electric field, the cyclotron time for recoil ions of more than 620 μsec for

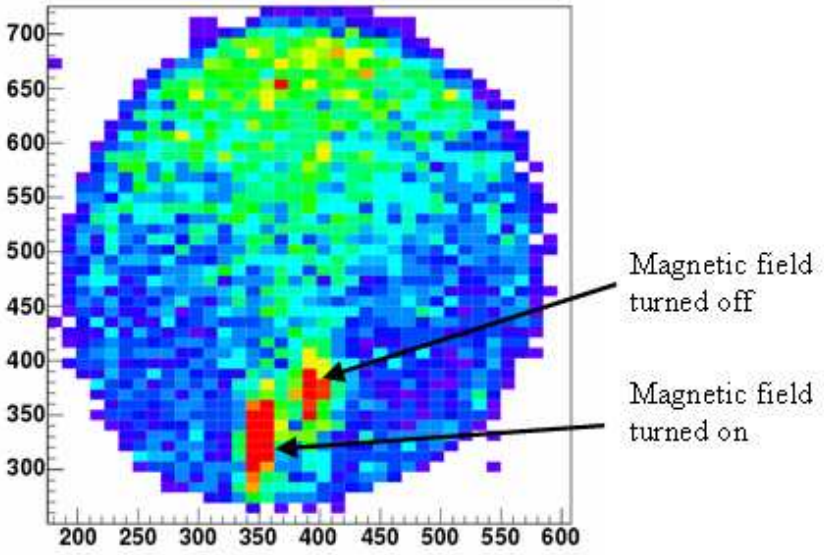

Figure 3.21: The small shift in the position of impact of Ar^{+1} ions as a result of the magnetic field of the Helmholtz coils. The relative location of both peaks with respect to each other can not here be described quantitatively sice they were collected during test measurements at different settings of the vertical electric field.

different argon charge states under the above conditions is usually much longer than their flight-times (*table* 3.3), indicating that the ion trajectories are only weakly affected by the magnetic field of the Helmholtz coils. It basically results in a slight rotation ($\approx 6^{\circ} for Ar^{1+}$ *in the present work*) of the ion image on the recoil-detector, which can be easily compensated by a corresponding back-rotation of the whole ion position distribution on the detector by few degrees. The shift in position of Ar^{1+} ions due to the presence of the magnetic filed is illustrated in figure (3.21) where it shows at the same spectrum the positions of impact of Ar^{1+} ions on the detector with and without the magnetic filed.

3.5.6 Detection of Electrons in the Reaction Microscope

In fast ion-atom collisions, two different types of electrons are produced as a result of the collision: low-energetic (*slow*) electrons originating from the ionization of the target atom and high-energetic (*fast*) electrons originating from

the ionization of the projectile ion. Slow electrons can be detected in the reaction microscope by a projection technique analogous to the one discussed for ions. Again, the position and time of flight (TOF) information allows an unambiguous reconstruction of the initial electron momentum vector. Electrons emerging from the collision are accelerated parallel to the beam direction into the direction opposite to the recoil ions by the same electric field which accelerates the recoil ions. Under the effect of the small homogenous magnetic field of the Helmholtz coils, electrons travel on spiral trajectories from the reaction volume towards another 2D position sensitive micro channel plate electron detector mounted at about 33 *cm* flight path with its center at the same horizontal level as the ion beam; the center of the detector with 80 *mm* diameter is horizontally displaced by 7 *cm* with respect to the beam axis to provide space for the incoming ion beam to pass the electron detector without interfering. In addition, this detector is mounted inside a movable feed-through (*spring bellow*) controlled by a linear electric drive which enables the detector to be moved far away from the beam line during the beam-focusing stage before starting the experiment. This will prevent the beam from hitting directly the detector which may destroy the MCP.

The same considerations as those for the recoils can be applied to reconstruct the longitudinal momentum of electrons from the electron TOF. However, because of their high initial kinetic energies, the approximate equation used for ions (*equation* 3.23) could not be used because the condition of validity that the initial kinetic energy is small compared to qU is not satisfied.

In the transverse direction perpendicular to the field axis, the electrons are affected by the Lorentz force of the applied homogeneous magnetic field given non-relativistically by :

$$\vec{F} = e(\vec{v} \times \vec{B}) \tag{3.27}$$

where $\vec{v}$ is the electron's velocity, e is the electron's charge, and B is the strength of the applied magnetic field. As a result, electrons travel along a circle with a cyclotron frequency

$$\omega = \frac{2\pi}{T} = \frac{eB}{m_e} \tag{3.28}$$

where m_e is the electron mass, and T is the cyclotron time needed for one complete cycle given by $T = 2\pi\frac{m_e}{eB}$ which is the same for all electrons regardless of their velocity. Under the operation conditions of our experiment, a cyclotron time of 31 *nsec* is calculated. The radius of the electron's circular path R reflects the magnitude of its transverse momentum and is related to it as

$$p_\perp = e\ B\ R \tag{3.29}$$

With a magnetic field set to 11.5 *Gauss* all trajectories of electrons with transverse momentum up to 1.8 *a.u.* are confined to a cylinder with a radius of 1.9 *cm*, independent of the electric field strength and independent of the spectrometer geometry. Hence, a detector with 8 *cm* diameter is sufficient to achieve a 4π solid angle collection efficiency for all electrons with transverse momentum of less than 1.8 *a.u.*, i.e. in the range of typical electron transverse momenta measured in the present experiment.

Electrons detected and collected by the electron detector are either high energetic fast electrons resulting from the ionization of N^{3+} projectiles with energy distribution centered around 1.975 *keV*, or low energetic slow electrons resulting from the ionization of argon gas target atoms with energies less than 100 *eV*.

Under the operation conditions of our experiment, the average total time of flight was about 161 *nsec* for slow electrons which corresponds to 5.2 complete cycles and about 12.6 *nsec* for fast electrons which corresponds to 0.4 complete cycles.

The time of flight of electrons was measured by means of coincidence with the ionized projectiles Ne^{4+}. The start signal of a time to analog converter (TAC) was generated by the detection of an electron, while the stop signal is generated by the delayed signal of the charge analyzed projectiles Ne^{4+}. The measured time of flight spectrum for both slow and fast electrons is shown in figure (3.22)

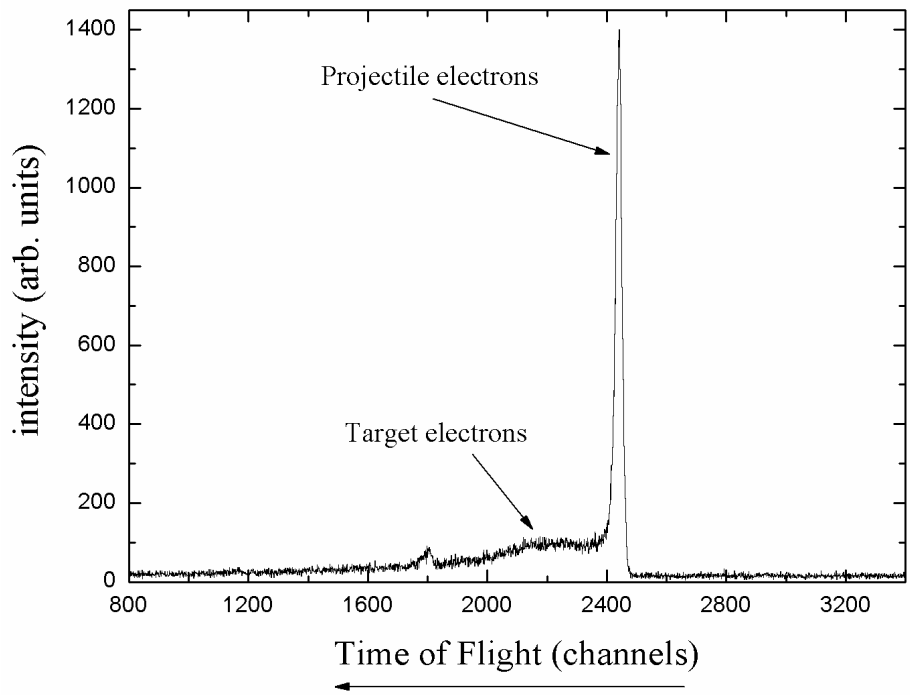

Figure 3.22: Electron time of flight spectrum for the ionization of Ne^{3+} measured in coincidence with Ne^{4+} projectiles.

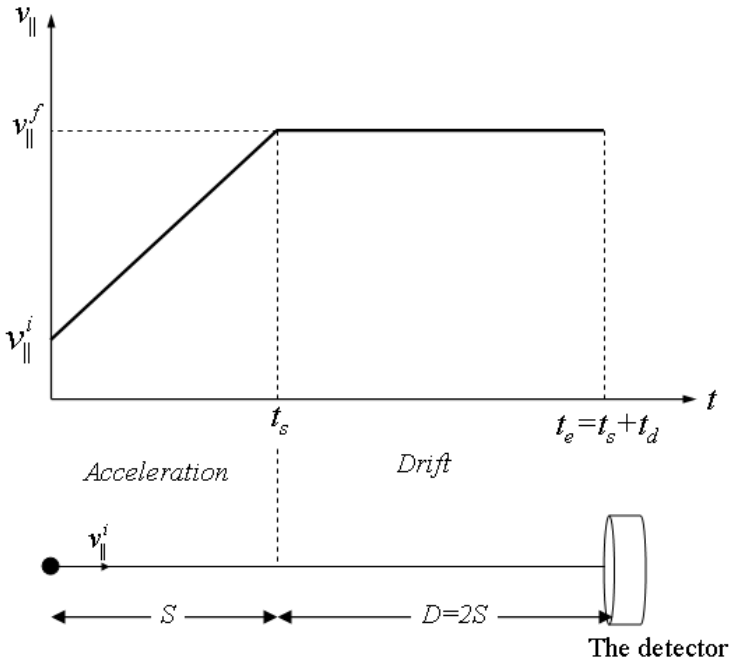

Figure 3.23: Geometrical representation of the acceleration and drift regions of the ideal path of electrons in the reaction microscope for ideally parallel field lines at the end of the potential plates. No shielding grid is used.

Calculation of the longitudinal momentum of electrons

The methods described in the following paragraphs are adapted from [165]. Electrons emerging from the collision are accelerated parallel to the beam direction for a distance of $S = 11\ cm$, then they drift over a field free region of $D = 2S = 22\ cm$ length towards the MCP detector (*see figure* 3.23). The total time of flight (t_e) of a certain electron is a function of the longitudinal component of its initial velocity ($v_{||}^{i}$) and can be written as a sum of the two times of flight of the electron in the acceleration (t_s) and drift (t_d) regions.

$$t_e(v_{||}^{i}) = t_s(v_{||}^{i}) + t_d(v_{||}^{i}) \tag{3.30}$$

the time of flight of the electron in the acceleration region (t_s) can be related to its acceleration a through the relation

$$S = v_{||}^{i} t_s + \frac{1}{2} a t_s^2 \tag{3.31}$$

where a is given by

$$a = \frac{eU}{m_e S} \tag{3.32}$$

substituting this value of a in equation 3.31 and rearranging, we find that t_s satisfies the quadratic equation

$$t_s^2 + (\frac{2m_e S v_{||}^i}{eU})t_s - \frac{2m_e S^2}{eU} = 0 \tag{3.33}$$

with the solution

$$t_s = (\frac{S\sqrt{2m_e}}{eU}\ )[\ \sqrt{\frac{1}{2}m_e {v_{||}^i}^2 + eU} - \sqrt{\frac{1}{2}m_e {v_{||}^i}^2}\ ] \tag{3.34}$$

After using the mathematical identity $x-y = \frac{x^2-y^2}{x+y}$ with $x = \sqrt{\frac{1}{2}m_e {v_{||}^i}^2 + eU}$ and $y = \sqrt{\frac{1}{2}m_e {v_{||}^i}^2}$, we can write the final form of t_s as

$$t_s = \frac{S\sqrt{2m_e}}{\sqrt{\frac{1}{2}m_e {v_{||}^i}^2 + eU} + \sqrt{\frac{1}{2}m_e {v_{||}^i}^2}} \tag{3.35}$$

Now, the longitudinal component of the electron's velocity at the end of the acceleration region ($v_{||}^f$) is related to its acceleration a through the relation

$$v_{||}^f = v_{||}^i + at_s \tag{3.36}$$

with the help of equations (3.32) and (3.34), this can be written as

$$v_{||}^f = \sqrt{\frac{2(\frac{1}{2}m_e {v_{||}^i}^2 + eU)}{m_e}} \tag{3.37}$$

in the drift region, the electron will maintain the same constant velocity $v_{||}^f$ and will cover the distance in a time t_d given by

$$t_d = \frac{D}{v_{||}^f} = \frac{2S}{v_{||}^f} \tag{3.38}$$

using the result of equation (3.37), t_d can be written as

$$t_d = \frac{S\sqrt{2m_e}}{\sqrt{\frac{1}{2}m_e v_{||}^{i\,2} + eU}} \tag{3.39}$$

substituting equations (3.35) and (3.39) in equation (3.30) we get

$$t_e(v_{||}^i) = S\sqrt{2m_e}\Big[\ \frac{1}{\sqrt{\frac{1}{2}m_e v_{||}^{i\,2} + eU} + \sqrt{\frac{1}{2}m_e v_{||}^{i\,2}}} + \frac{1}{\sqrt{\frac{1}{2}m_e v_{||}^{i\,2} + eU}}\ \Big] \tag{3.40}$$

this expression can be written in a simpler form with the substitutions

$$X = \sqrt{\frac{\frac{1}{2}m_e v_{||}^{i\,2}}{eU}} \qquad and \qquad \tau = \frac{t_e\sqrt{eU}}{S\sqrt{2m_e}} \tag{3.41}$$

which converts equation (3.40) into the form

$$\tau = \frac{1}{X + \sqrt{1+X^2}} + \frac{1}{\sqrt{1+X^2}} \tag{3.42}$$

which can be solved for X in terms of τ. The program "Mathematica" [171] was used [165] for this purpose and the result is written as

$$X = \alpha + \frac{\beta}{\tau} - \gamma\tau + \delta sin(\tau) \tag{3.43}$$

where $\alpha = -0.0430786$, $\beta = 1.50802$, $\gamma = 0.473918$, $\delta = 0.255789$

Finally, with the help of equation (3.41), the initial longitudinal momentum of the electron ($p_{||} = m_e v_{||}^i$) can be calculated from

$$p_{||} = X\sqrt{2m_e eU} \tag{3.44}$$

which enables to calculate the initial longitudinal momentum of the electron ($p_{||}$) by knowing its absolute time of flight. Values of the longitudinal momentum of the electron calculated using this result were proved to be in agreement with values produced by simulations made using SIMION [172] for the case of ionization of helium by carbon projectiles [17, 165].

Calculation of the transverse momentum of electrons

The methods described in the following paragraphs are adapted from [165]. To calculate the electron's transverse momentum vector, both pieces of information, position and TOF, are required. This can be illustrated with the help of figure (3.24) which represents the projection of an electron trajectory onto the electron detector surface, i.e. onto a plane perpendicular to the magnetic field axis. The origin, point $[X_o, Y_o]$, represents the point of intersection of the ion beam with the gas-jet. In practice this zero point is simply given by the center of the target electrons distribution on the 2D electron spectrum since the momentum distribution of target electrons is rotationally symmetric around the magnetic field axis. An electron, which is emitted at the origin with initial transverse momentum $p_\perp^i$ under a certain angle φ with respect to the positive x-axis travels on a spiral trajectory, corresponding to a circle of radius R in the transverse plane, before it hits the detector at the point $[X_1, Y_1]$ with a certain displacement r from the center.

The radius R is a direct measure of $p_\perp^i$ (*see equation* 3.29) while the angular displacement ωt_e depends only on the electron TOF. From simple geometrical considerations one gets

$$sin(\frac{\omega t_e}{2}) = \frac{\frac{r}{2}}{R} \tag{3.45}$$

If the electron performs more than one complete turn, ωt_e has to be replaced by $(\omega t_e - 2\pi N)$ where N (*number of full turns*) is the next lowest integer of the ratio $(\frac{\omega t_e}{2\pi})$. Using $\omega = \frac{2\pi}{T}$ in equation (3.45) and rearranging we get

$$R = \frac{r}{2|sin(\frac{t_e}{T}\pi)|} \tag{3.46}$$

with the help of equation (3.29) and $B = \frac{2\pi m_e}{eT}$, we end up with

$$p_\perp = \frac{\pi r m_e}{T sin(\frac{t_e}{T}\pi)} \tag{3.47}$$

Thus, the magnitude of the transverse momentum $p_\perp$ can be calculated from the distance between the point of detection and the origin

$$r = \sqrt{(X_1 - X_o)^2 + (Y_1 - Y_o)^2} \tag{3.48}$$

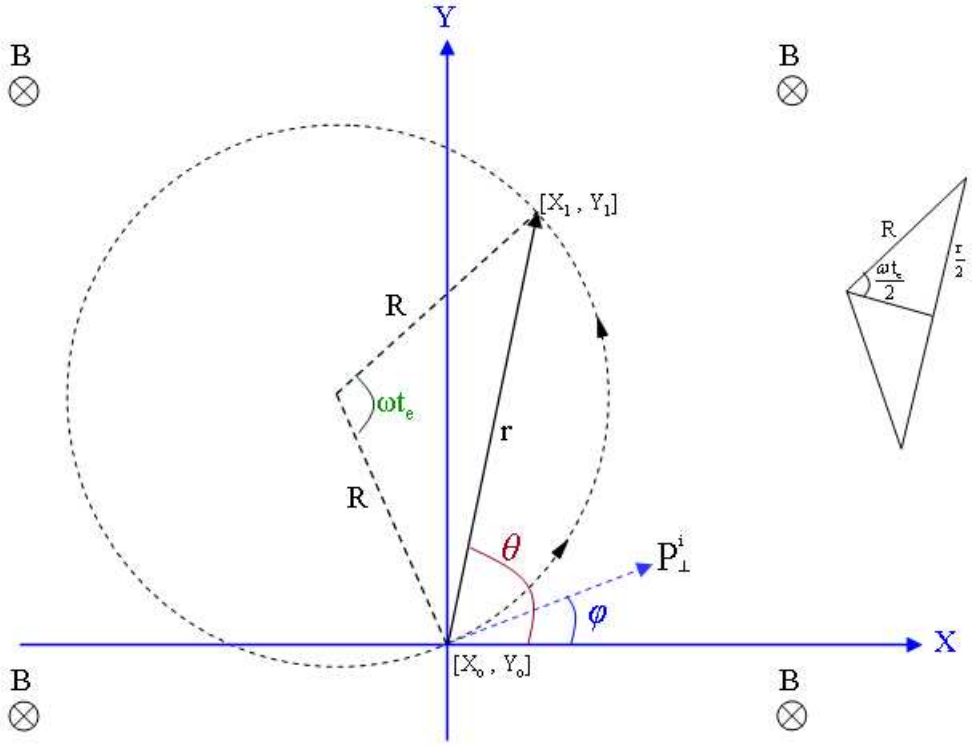

Figure 3.24: Projection of an electron trajectory onto a plane perpendicular to the magnetic field. The radius R is given by equation (3.29). Point $[X_o, Y_o]$ represents the point of intersection of the ion beam with the gas-jet.

in cylindrical coordinates, and the electron time of flight t_e. Still, the assignment of measured quantities and initial momentum is unique, as long as the denominator in equation (3.46) is larger than zero. Whenever electrons perform exactly N complete turns they hit the detector at the origin $[X_o, Y_o]$ (*see figure* 3.24) independent of their initial transverse momentum or, in other words, all electrons with flight-times equal to a multiple integer of the cyclotron time are focused onto the same spot on the detector and no momentum information is obtained.

The emission angle φ can be related to the angle of detection $\theta = \arctan\left(\frac{Y_1 - Y_o}{X_1 - X_o}\right)$ with the help of figure (3.24) as follows: the angle γ between the emission angle φ and the direction of the point of detection θ is equivalent to $\frac{\omega t_e - 2\pi N}{2}$; γ increases by 180^o with every complete turn. This can be expressed in terms of the modulus function (*The modulus function mod[x,y] returns the remainder after x is divided by y*) as

$$\gamma = mod[\ (\frac{180 t_e}{T}), 180\ ] \tag{3.49}$$

then the angle φ can be expressed also in terms of the modulus function as

$$\varphi = mod[(\theta - \gamma), 360] \tag{3.50}$$

with the knowledge of r and φ, the transverse momentum vector is determined and can be expressed in terms of its components

$$p_{\perp x} = p_\perp \cdot cos(\varphi) \tag{3.51}$$

$$p_{\perp y} = p_\perp \cdot sin(\varphi) \tag{3.52}$$

3.5.7 Momentum Resolution

The methods described in this entire section follow closely references [17, 165]. The actual momentum resolution which can be reached for electrons and recoil ions in the reaction microscope depends on the different parameters of the microscope and the data acquisition system. In the following two subsections, the momentum resolution achieved in the GSI reaction microscope is discussed.

Momentum Resolution for Recoil Ions

The resolution of the measured recoil-ion momentum in the reaction microscope depends mainly on the momentum spread of the target gas, the position resolution of the used detector and, to a smaller extent, the size of the interaction target volume. As mentioned earlier (*section* 3.5.1), the estimated speed ratio for our jet system is about 30 which means an internal temperature near 0.83 K which corresponds to an average thermal energy per atom of only 0.11 meV. This is equivalent to a momentum spread in the jet direction of $\Delta p_y^{thermal} = \pm\ 0.76\ a.u.$ for argon. The momentum spread of the target gas in the plane perpendicular to the jet direction, the x- and z-directions as indicated in figure (3.10), depends on the distance between the nozzle and the skimmer and the diameters of both. For the gas-jet used in our reaction microscope, a momentum spread of $\Delta p_x^{thermal} = \Delta p_z^{thermal} \approx \pm\ 0.12\ a.u.$ was estimated [165] in the case of helium which can be scaled to a momentum spread of $\Delta p_x^{thermal} = \Delta p_z^{thermal} \approx \pm\ 0.38\ a.u.$ for argon as it scales with the square root of the atomic mass ($p \propto \sqrt{m}$).

In our experiment, the ion beam was collimated to a cross section of about 1.2 $mm \times 1.1\ mm$ ($horizontal \times vertical$) and the position resolution of the detector used (*wedge & strip anode*) is about 0.5 mm [17, 165] which leads to a combined uncertainty in the position of

$$\Delta X \approx \sqrt{1.2^2 + 0.5^2} = 1.30\ mm \tag{3.53}$$

$$\Delta Y \approx \sqrt{1.1^2 + 0.5^2} = 1.21\ mm \tag{3.54}$$

which will in turn result in a momentum uncertainty of

$$\Delta p_x^{position} = \frac{m\Delta X}{t} = 0.95\ a.u. \tag{3.55}$$

$$\Delta p_y^{position} = \frac{m\Delta Y}{t} = 0.88\ a.u. \tag{3.56}$$

where the channel width in the time of flight

$$\Delta t = \frac{time\ window\ of\ the\ TAC}{no.\ of\ channels\ in\ the\ ADC} = \frac{50\ \mu sec}{3840} = 13\ nsec \tag{3.57}$$

represents the upper limit in the relative error in the determination of the recoil ion (Ar^{1+}) time of flight of $\frac{\Delta t}{t} \leq \frac{13\ nsec}{45.7\ \mu sec} = 0.03\%$ since one can determine the centroid of a peak in the time spectrum with more precession than the channel width by fitting. This error is relatively small and can be ignored in the calculation of the uncertainty of the transverse momentum components. Now, the total uncertainty in both transverse directions is given by:

$$\Delta p_x^{total} = \sqrt{0.38^2 + 0.95^2} = 1.02\ a.u. \tag{3.58}$$

$$\Delta p_y^{total} = \sqrt{0.76^2 + 0.88^2} = 1.16\ a.u. \tag{3.59}$$

and the entire uncertainty in the transverse momentum is

$$\Delta p_\perp = \sqrt{1.02^2 + 1.16^2} = 1.54\ a.u. \tag{3.60}$$

In the longitudinal direction, along the projectile direction, (*i.e. z-direction*), in addition to the previously mentioned thermal spread of the target gas, the momentum resolution is also a function of the spectrometer parameters. According to equation (3.23), the longitudinal momentum resolution is a function of the relative error in the time of flight ($\Delta t/t = 2.8 \times 10^{-4}$), the relative error in the length of the acceleration distance ($\Delta S/S = 0.5\ cm/11\ cm = 0.045$), and the relative error in measuring the applied potential ($\Delta U/U = 0.1\ V/42.2\ V = 0.002$)

$$\Delta p_z^{spec.}/p_z^{spec.} = \sqrt{(2.8 \times 10^{-4})^2 + 0.045^2 + 0.002^2} = 0.045 \tag{3.61}$$

for example, for a recoil ion with 3 *a.u.* of longitudinal momentum

$$\Delta p_z^{spec.} = 3 \times 0.045 = 0.135\ a.u. \tag{3.62}$$

and the entire longitudinal momentum resolution can be given by

$$\Delta p_{||} = \sqrt{0.38^2 + 0.135^2} = 0.40\ a.u. \tag{3.63}$$

From the previous discussion, one can see that the factors contributing most to the recoil ion momentum resolution are the target gas used, the thermal

spread of the target gas, and the beam size, which means that the momentum resolution can be improved by pre-cooling the target gas and focusing the ion beam to the smallest possible size. In a recent experiment [165], a helium target was used and better momentum resolution, $\Delta p_{\perp} = 0.44$ *a.u. and* $\Delta p_{||} = 0.13$ *a.u.*, for helium recoil ions was achieved.

Momentum Resolution for Electrons

The momentum resolution for electrons does not depend on the thermal spread of the gas jet because of their high speed compared to the speed for the recoil ions. In addition, the calculation of the electron's longitudinal momentum resolution is more difficult since the electron's longitudinal momentum is related nonlinearly to its time of flight (*section* 3.5.6). The smaller the longitudinal momentum of the electron and the larger the time of flight, the better the momentum resolution and vice versa. For a target electron with $p_{||} < 0.5$ *a.u.*, a momentum resolution of only $\Delta p_{||} \approx 0.02$ *a.u.* was estimated for our reaction microscope, while a momentum resolution of $\Delta p_{||} \approx 0.08$ *a.u.* is estimated in the case of an electron having $p_{||} < 3$ *a.u.*. These values were estimated using error propagation rules together with equations (3.41, 3.43, *and* 3.44) using ($\Delta t_e = 1$ *nsec*, $\Delta S/S = 0.5$ *cm*/11 *cm* = 0.045, and $\Delta U/U = 0.1$ *V*/42.2 *V* = 0.002).

In the case of the projectile electrons with their high energy the effect of the accelerating potential can be neglected and the longitudinal momentum of the electron depends linearly on the time of flight ($p_{||} = m_e \frac{flight\ distance(33\ cm)}{t_e}$). The time resolution of 0.5 *nsec* of the TDC used (Lecroy 3377) results in a longitudinal momentum resolution of $\Delta p_{||} \approx \pm 0.48$ *a.u.* for the projectile electrons having 12 *a.u.* of longitudinal momentum.

The resolution power for the transverse momentum of an electron depends strongly on its time of flight t_e and the displacement r of its point of detection on the detector from the center of its circular trajectory (*equation* 3.47). The best transverse momentum resolution is achieved at maximum dicplacements ($when\ t_e = (n + \frac{1}{2})T,\ n = 0, 1, 2, ...$) while at $r = 0$ ($when\ t_e = nT,\ n = 1, 2, 3, ...$) no momentum information can be obtained. This means also that, for electron transverse momenta, a smaller magnetic filed will be favorable and

allow the electron to move with larger radius and thus give better momentum resolution. For example, the radius of the circular trajectory of an electron with 0.5 *a.u.* of transverse momentum under the 11.5 *Gauss* magnetic field as in the course of the present work will be ≈ 5 *mm*. The displacement of the electron from the center varies between $r = 0$ and $r = 10$ *mm*. The estimated momentum resolution at the maximum displacement in this case is $\Delta p_\perp \approx 0.09$ *a.u.* estimated with the help of error propagation rules together with equations (3.10 *and* 3.47) using $\Delta t_e = 1$ *nsec*, $\Delta B/B = 0.05$ *Gauss*/11.5 *Gauss* $= 0.0043$, and $\Delta r/r = 0.5$ *mm*/10 *mm* $= 0.05$.

In the case of the projectile electrons, the time of flight has a narrow distribution around the average of 12.6 *nsec* which corresponds to 0.4 complete cycles (*see section* 3.5.6). This means that all projectile electrons will hit approximately at the same displacement from the center and the momentum resolution is independent of the initial electron momentum, which is estimated to be $\Delta p_\perp \approx 0.43$ *a.u.* in our case.

From the previous discussion, we see that using smaller extraction potentials will result in longer flight times and thus better momentum resolution. Similarly, smaller magnetic fields will result in larger radius of the spiral trajectory of electrons and thus better momentum resolution. But, it is noteworthy that, the same factors that improve the momentum resolution will, at the same time, reduce the spectrometer acceptance (*detection efficiency*) for the slow and fast electrons, target and projectile electrons. In the present experiment, a simultaneous detection of target- and projectile-electrons was carried out, which required the use of compromise values for the electric and magnetic extraction fields. In a recent experiment [165], only target electrons were detected and better momentum resolution was achieved ($\Delta p_{||}^{e-target} = 0.01$ *a.u.* at $p_{||} = 0.5$ *a.u.* , $\Delta p_{||}^{e-target} = 0.06$ *a.u.* at $p_{||} = 3$ *a.u.* and $\Delta p_\perp^{e-target} = 0.02$ *a.u.* at $p_\perp = 0.5$ *a.u.*).

At higher beam energies (> 4 *MeV/u*), projectile electrons will have higher and higher speeds and it becomes hardly possible to map the slow- and fast-electrons onto the same detector, i.e. a small magnetic field of the Helmholtz coil will not be enough to guide fast electrons towards the detector. To extend the 4π detection efficiency of the reaction microscope to higher electron ener-

gies, a separate spectrometer with independent extraction parameters should be used, which was the motivation for building our magnetic spectrometer to be combined with the reaction microscope in the close future to enable the simultaneous detection of target- and projectile-electrons and the detection of recoil ions at high beam energies with good momentum resolution.

3.5.8 First Results From the Present Reaction Microscope

We have used the present reaction microscope to perform a study of the simultaneous target and projectile ionization. The experiment was performed using a 3.6 MeV/u ($v_p = 12$ $a.u.$) stripped and charge analyzed Ne^{3+} beam from the UNILAC. A well localized argon target was provided by the double stage supersonic jet. The charge state was analyzed after the collision and Ne^{4+}, the up charged projectiles, were recorded by a fast scintillation detector (*more details in section* 3.5).

$$3.6\ (MeV/u)\quad Ne^{3+} + Ar \Rightarrow Ne^{4+} + Ar^{q+} + e^-_{fast} + e^-_{slow}$$

Energy distribution of slow (*target*) electrons

The electron-projectile time spectrum of figure (3.22) was calibrated before the measurement and each channel can be transformed to the corresponding electron time of flight according to

$$TOF(nsec) = \frac{2896.67 - channel\ number}{0.76389} \tag{3.64}$$

The electron time of flight obtained for each channel is converted into the corresponding electron momentum (*according to the discussion of section* 3.5.6) from which the electron energy can be calculated ($E = p^2/2m$).

The resulting single differential electron emission cross sections (*integrated over all emission angles*) for the argon single ionization ($d\sigma/dE$) are displayed in figure (3.25). A possible maximum is observed at electron energies of about 8 eV. The differential cross section decreases rapidly above the maximum and

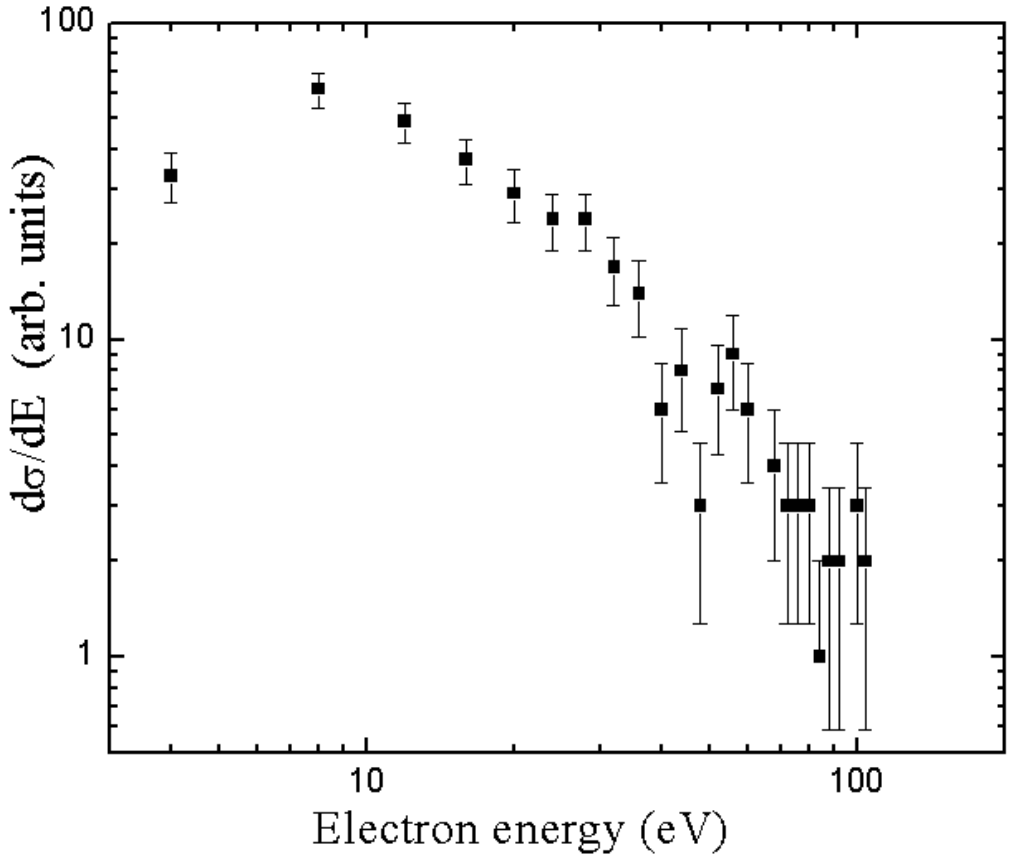

Figure 3.25: Single differential electron emission cross section for argon single ionization ($d\sigma/dE$) in collisions with 3.6 MeV/u Ne^{3+}. The relative statistical error in the cross sections is represented by the error bars while the uncertainty in the electron energy is directly related to the momentum resolution discussed in details in the text (*section* 3.5.7).

falls off by a factor of 10 at $E_e \approx 60\ eV$. A similar behavior has been observed for the pure single target ionization in 3.6 MeV/u Ni^{24+} on He collisions [111] and for 1 MeV/u O^{8+} on He collisions [173].

Longitudinal momentum distribution of slow electrons and recoil ions

Figure (3.26) shows the longitudinal momentum distributions for Ar^{1+} recoil ions and low energy electrons ionized out of argon during simultaneous single ionization of the projectile ($Ne^{3+} \rightarrow Ne^{4+}$). The low energy electron

emission is not nearly isotropic as expected for the present small perturbation with a Sommerfeld parameter $q/v = 0.25$ but unexpectedly exhibits the same strong forward asymmetry for low energy emission as observed for pure single ionization in strong perturbation by the 3.6 MeV/u Ni^{24+} projectile with a Sommerfeld parameter $q/v = 2$ [111]. The slow electron longitudinal momentum distribution has a peak at a small positive value of longitudinal momentum and electrons are emitted predominantly in the forward direction, i.e. the direction of the outgoing projectiles.

The calibration of the recoil-ion TOF, i.e. the absolute determination of the longitudinal recoil-ion momenta has been performed utilizing the momentum conservation in the longitudinal direction (*in atomic units*):

$$p_{||}^{R} = \frac{Q + E_e^p + E_e^T}{v_p} - p_{||}^{e} \tag{3.65}$$

where Q is the total energy loss of the projectile, v_p is the incoming projectile velocity of 12 *a.u.*, $p_{||}^{e}$ is the longitudinal momentum of the target-electron, and E_e^p and E_e^T are the continuum energies for the projectile- and target-electrons respectively. At large projectile velocities and for small ionization potentials (0.57 *a.u. for Ar*) as well as continuum electron energies (*typically about* 1 *a.u.*), the first two terms are negligibly small and equation (3.65) reduces in good approximation to

$$p_{||}^{R} + p_{||}^{e} \approx 0 \tag{3.66}$$

Since the longitudinal momenta of the recoil-ion and the electron are measured in each single event, the sum-momentum (*left hand side of equation* 3.66) should result in a sharp peak. For this reason, the time of flight of the ion with zero initial longitudinal momentum, $t_\circ$ in equation (3.23), is chosen in our case to be the one which minimizes the sum-momentum $p_{||}^{R}+p_{||}^{e}$. The resulting recoil ion longitudinal momentum distribution shown in figure (3.26) has a peak at a small negative value of longitudinal momentum leading to the conclusion that recoil ions are emitted predominantly back to back with respect to the direction of emission of slow electrons. These two distributions are related through the conservation of momentum of the slow electron, recoil ion, projectile, and the projectile electron (*equation* 3.67). This behavior is similar to that found

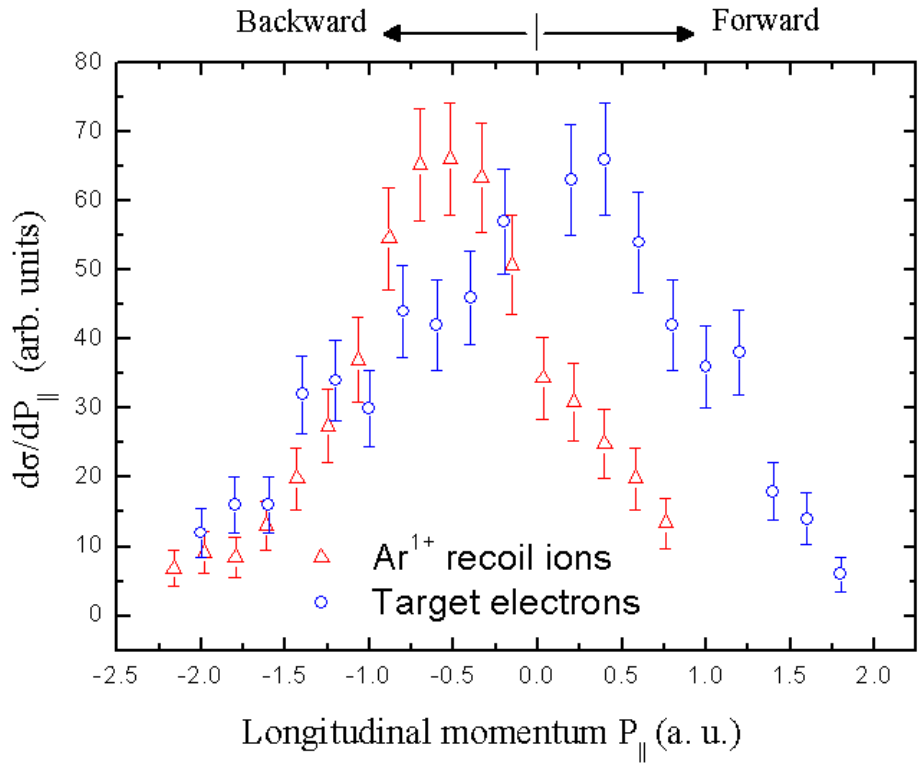

Figure 3.26: The longitudinal momentum distributions for Ar^{1+} recoil ions and low energy electrons ionized out of the target during simultaneous single ionization of the projectile. The relative statistical error in the cross sections is represented by the error bars while the uncertainty in the longitudinal momentum is discussed in details in the text (*section* 3.5.7).

for the pure single target ionization in the collision of 3.6 MeV/u Ni^{24+} projectile and He target by the CTMC (*Classical-Trajectory Monte Carlo*) theory [111] and by the CDW-EIS (*Continuum Distorted Wave–Eikonal Initial State*) theory [174]. Moreover, the half width (*FWHM*) of the electron distribution (1.81 *a.u.*) is clearly larger than that of the corresponding recoil distribution (1.32 *a.u.*) and appears to mirror the momentum fraction inferred for the projectile electron.

The ionization of the Ne^{+3} projectile is a result of the interaction between a projectile electron with the argon nucleus (e-N) or with an argon electron (e-e). The two different mechanisms can be distinguished according to their different kinematics. If (e-N) interaction leads to the ionization of the Ne^{+3}

projectile, the argon nucleus plays the active role, whereas the argon electrons remain at rest and act as spectators and can only be ionized due to second order process. In this case, the momentum transferred to the recoil argon ion is expected to be bigger than the one transferred to any target electron. If (e-e) interaction leads to the ionization of the Ne^{+3} projectile, an argon electron plays the active role, whereas the recoil argon ion stays at rest and acts as a spectator. In this case, the energy of the active argon electron relative to the Ne^{+3} projectile ($E_e = \frac{1}{2} m_e v_p^2$) has to be larger than the lowest ionization potential of the Ne^{+3} ion. Here, the momentum transferred to the argon electron is expected to be bigger than the one transferred to the recoil argon ion.

Calculations [87] indicate that the (e-e) interaction dominates the cross section for projectile ionization at large impact parameters since the nuclear potential of the target, which might cause ionization of the projectile in an (e-N) interaction, is effectively screened by the target electrons. The condition of simultaneous projectile and target ionization emphasizes the small impact parameter region so that for q/v=0.25 the electron nucleus (e-N) and the electron-electron (e-e) channels both contribute with similar strength to the simultaneous projectile and target ionization.

Longitudinal momentum distribution of Ne^{4+} projectiles

For the inspection of the projectile longitudinal momentum change, the sum of the low energy electron and the recoil ion longitudinal momenta is drawn (*figure* 3.27). The resulting distribution is a sharp peak with its center close to zero. According to the conservation of momentum (*equation* 3.67) this sum represents also the longitudinal momentum change for the projectile and the projectile-electron

$$p_{||}^{R} + p_{||}^{e-target} = -(\Delta p_{||}^{p} + \Delta p_{||}^{e-proj}) \tag{3.67}$$

it follows that recoil and low energy electron longitudinal momentum change is compensated by the momentum change of the projectile and of the projectile-electron.

The sharp distribution (*small momentum change of the projectile and the projectile electron*) indicates that the longitudinal momenta of the argon atom fragments (*the slow electron and the* Ar^{1+} *recoil ion*) are much larger than the net momentum transfer to the argon atom by the projectile. The atom seems to dissociate in the strong, long-ranging projectile potential. This means that, the slow electron longitudinal momentum is not balanced, as might be expected, by the longitudinal momentum change of the projectile or the longitudinal momentum change of the projectile electron but mainly by the backward recoiling of the Ar^{1+} ion, i.e. no participation of the projectile momentum which only provides energy to the electron.

The measured width (FWHM) is 1.31 *a.u.* and thus 6 times larger than that found for pure single target ionization at the same collision velocity using He target [111]. The difference is partly due to the larger momentum spread ($\pm$ 0.38 a.u.) of the Ar target in the longitudinal direction, i.e. the z-direction, compared to that of He ($\pm$ 0.05 a.u.) and partly due to the momentum distribution for the electrons ionized out of the projectile which is assumed to be comparable or larger than that measured for the ionized target electrons because the Compton profile of electrons in Ne^{3+} ($E_B \approx 106\ eV$) is larger than that for Ar ($E_B \approx 16\ eV$) . The collision system will be revisited with more detailed investigation of the (e-e) channel.

3.6 The Imaging Forward Electron Spectrometer

As mentioned earlier, in order to perform forward electron spectroscopy at high near relativistic energies, it was necessary to build an independent magnetic spectrometer to guide fast electrons emitted into a narrow cone around the beam direction onto a position sensitive detector and which allows reconstructing the initial momentum of the fast electrons. The design criteria for the construction of the instrument were:

a) Separate electrons from the flood of secondary products with minimum interference with the circulating ESR beam.

b) Analyze electrons emitted in a direction near 0° close to the beam over a

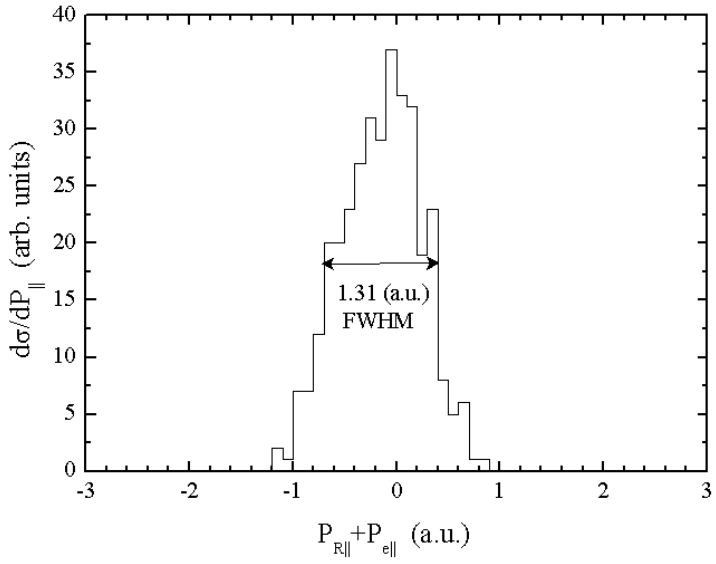

Figure 3.27: The sum of the low energy electron and recoil ion longitudinal momenta.

wide range of momenta including $v_{elec.} = v_{proj.}$ up to specific projectile energies of 400 MeV/u.

c) In the non-position sensitive mode a momentum resolution $\Delta p/p = 10^{-3}$ is desired.

d) In the position sensitive mode, permit reconstruction of the collision plane of the ionization event in the target zone after momentum analysis of electrons.

The "MIRKO" code [175] was used for beam trajectory calculations and simulations to achieve an accepted mapping of the electrons from the target zone onto the 2D position sensitive detector (*see figure* 3.28). The design chosen is a dipole-quadrupole triplet-dipole type and covers a solid angle of 4×10^{-4} sr. A schematic of the electron spectrometer is shown in figure (3.29). A 60° magnetic dipole of bending radius 200 mm, with an aperture of vertically 100 mm and horizontally 250 mm as required by the ESR beam optics, is mounted 940 mm from the target zone and immediately downstream of the target chamber is followed by a magnetic quadrupole triplet of 80 mm aperture and a second 60° magnetic dipole identical to the first one. This is followed by a pair of horizontal momentum defining slits, then a 2D position

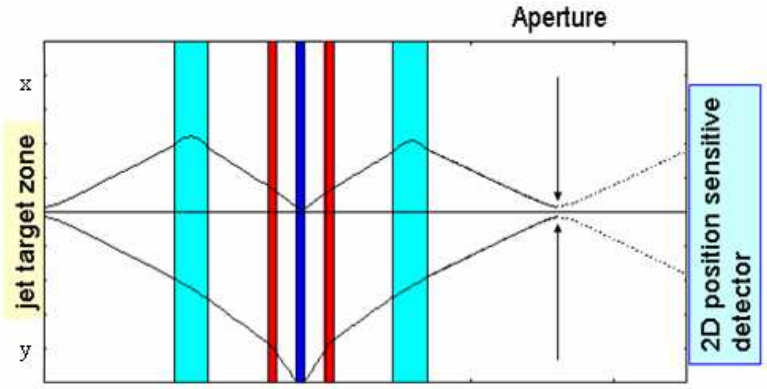

Figure 3.28: Trajectory of electrons in the spectrometer following MIRKO simulations.

sensitive multi-hit capable electron detector mounted in the focus (131.5 *cm downstream*) of the second dipole magnet 40 *cm* downstream of the momentum defining slits.

It deserves attention that the first 60° dipole magnet of the spectrometer which transports the electrons out from the beam line also may deflect the circulating ion beam. The deflection angle for the ion beam was calculated to be small enough that it can easily be corrected by the two nearest horizontal correction elements installed in front of the next main dipole magnets. Moreover, if small angular misalignments in the target section (*of order* 0.1 *mrad*) are acceptable, the ring can even be operated without the horizontal ion beam correctors [176].

Two correction coils are mounted vertically at both sides of the electron beam line just downstream of the quadrupole triplet to compensate for the small vertical deflections experienced by the electron beam in the earth magnetic field. The current in the correction coils is supplied by an independent power supply and can be remote-controlled from the outside of the ESR ring during the experiments.

The above mentioned geometry of the spectrometer restricts the geometrical solid angle acceptance to $\Delta\Omega/4\pi = 1.8 \times 10^{-4}$ which corresponds to a cone of half opening $\approx 1.5°$. The electron energy acceptance of the spectrometer can be discussed with the help of figure (3.30) which represents the electron

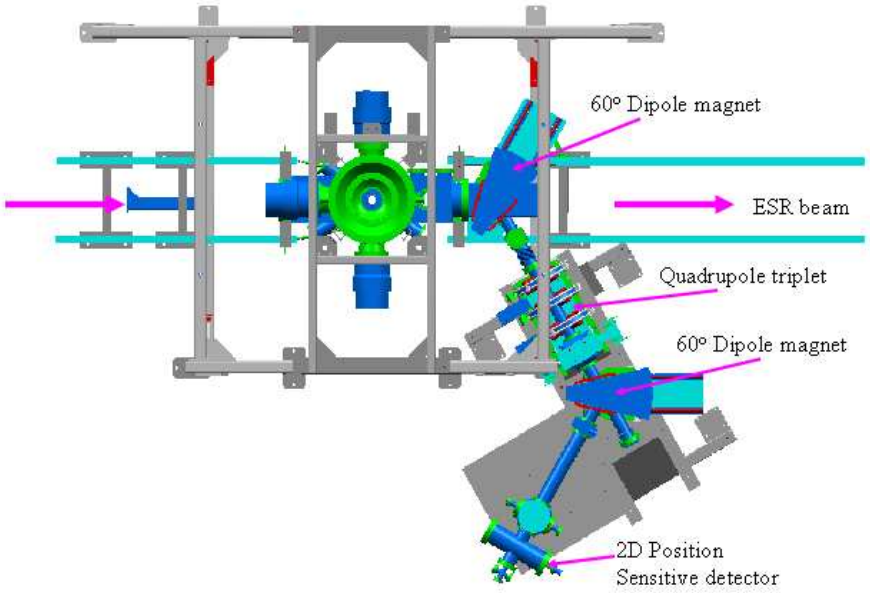

Figure 3.29: A schematic drawing of the forward electron spectrometer in the ESR storage ring.

detection angle in the lab system as function of the electron emission angle in the projectile system at beam energy 90 MeV/u (*present work*) for a set of electron emitter frame energies of 1, 10, 40, 50, and 100 eV. The spectrometer is set to record electrons emitted within a cone of half angle $\approx 1.5°$ centered on the forward direction which means -according to the figure- that all electrons with emitter-frame energies up to almost 40 eV will be mapped onto the detector with the entire azimuth (4π *detection efficiency*).

The spectrometer can be operated in different modes. In the telescopic mode, with magnification $|M_x| = |M_y| = 1$, the spectrometer maps the azimuthal distribution of electrons emitted by the projectile in the target zone below the jet and image it onto the 2D position sensitive detector. In this mode angular distributions of autoionizing states and anisotropies of electron capture to continuum (ECC) and electron loss to continuum (ELC) can be measured, e.g. angular distributions of autoionizing Rydberg states of the projectile up to very high n > 100 near the continuum threshold are now accessible in high resolution due to relativistic kinematics.

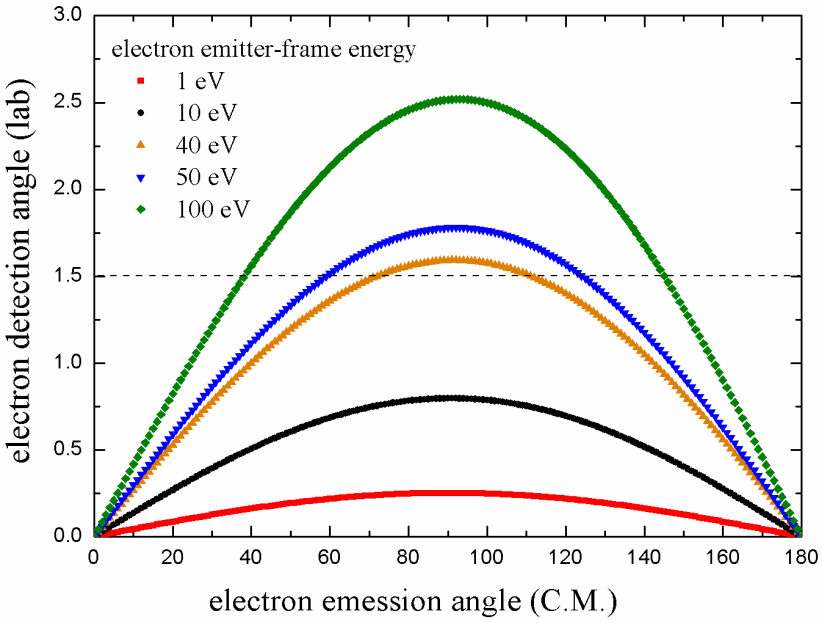

Figure 3.30: Electron detection angles as function of electron emitter-frame emission angles at 90 MeV/u for electron emitter-frame energies 1, 10, 40, 50, and 100 eV.

3.6.1 Commissioning of the Spectrometer

In relativistic collisions a large flood of secondary products can be generated in the beam tube besides electrons ionized from the collision partners. The characteristics of the low energy spectrum of these secondary particles produced in the ESR target zone and emitted into the forward direction has never been determined and is currently not known [154]. As the current 2D position sensitive detector in the spectrometer is not measuring the energy of the detected particles, it was imperative to show first that the spectrometer is suppressing the intense beam-induced background and is only transmitting electrons of selected momenta onto the detector. During the commissioning phase of the spectrometer we have replaced the 2D position sensitive detector temporarily with an energy analyzing Si(Li) detector for independent analysis of the energy of electrons and for identification of other particles potentially transmitted through the spectrometer. The Si(Li) detector was attached to the spectrometer in the focus of the second dipole magnet. The reaction studied in this step of the commissioning phase was the collision of

$$(392\ MeV/u)\ U^{89+}(1s^2 2s^1) + N_2 \ \rightarrow\ U^{90+}(1s^2) + e_{cusp} + target\ fragments$$

The spectrometer was tuned to a current for which, according to optics calculations, it only passes electrons with the momentum of a cusp electron, i.e. electrons moving at the same velocity as the projectiles, where the cusp energy E_{cusp} is given by

$$E_{cusp} = (\frac{m_e}{M_{proj}})E_{proj} = 215\ keV \tag{3.68}$$

Particles exiting the spectrometer traverse the 25 μm Iron (Fe) exit window of the spectrometer and the 100 μm Beryllium (Be) entrance window of the Si(Li) detector.

The energy spectra of the Si(Li) detector for all detected counts (*singles*) and for counts detected in coincidence with the up-charged U^{90+} projectiles (*loss channel*) were found to exhibit a peak at an energy of 125 keV (*figure* 3.31). The observed shift of the measured peak energy from the anticipated energy of 215 keV for electrons to 125 keV is due to the energy loss expected for electrons passing through the Iron window ($\Delta E \approx 37\ keV$), the air gap between the two windows ($\Delta E \approx 6\ keV$), and the Beryllium window ($\Delta E \approx 48$ keV). We could verify from the resulting spectra that the spectrometer very efficiently suppresses the flood of secondary products generated in the collision and we emphasize that almost all electrons appear in coincidence with the charge changed U^{90+} projectiles. This means that a nearly background free identification of cusp electrons can be achieved.

Additionally, a measurement of the 0° binary encounter electron emission was performed also during this commissioning phase of the spectrometer using the same detector configuration as above. The collision studied is (132.8 MeV/u) U^{89+} + N_2 . Count rates exceeding 2500 s^{-1} were seen and the resulting spectrum (*figure* 3.32) exhibit a peak maximum at electron momentum p=174 *a.u.* in close agreement with $p = 173$ *a.u.* found from 2-body relativistic kinematics. The width of the peak $\Delta p/p = 7.5\%$ ($FWHM$) reflects the momentum resolution of the instrument which depends on the operational mode and the image aperture which was left completely open during commissioning

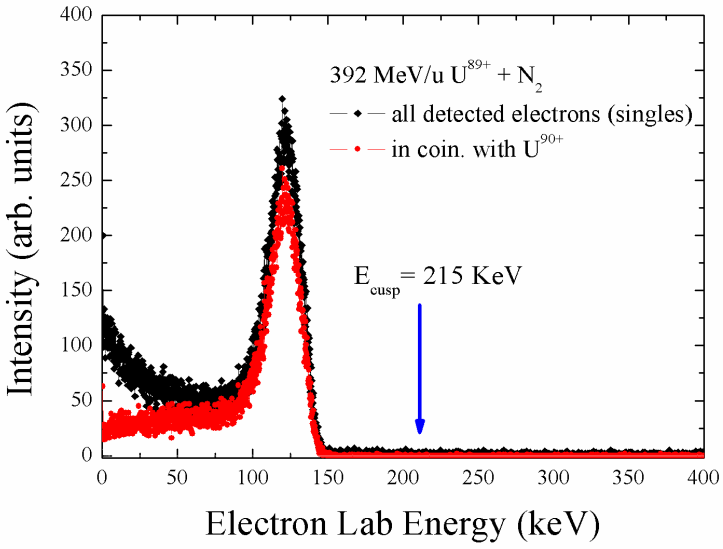

Figure 3.31: Comparison of energy spectra of cusp electrons detected with the Si(Li) detector behind the D-QT-D magnetic forward electron spectrometer.

runs.

In summer 2004, the electron spectrometer was equipped with a 2D position and time sensitive detector with multi-hit capability. In a first experiment with the 2D position sensitive electron detector we have measured forward electron emission from Li-like (98.2 MeV/u) $U^{89+} + N_2$ for electron energies between 16 keV and 280 keV, e.g. from well below the Cusp ($at \approx 54\ keV$) to beyond the Binary Encounter. The spectrometer was operated in a quasi multi scaling mode: for each measurement cycle in intervals [p_{min}, p_{max}], the two dipole magnetic field values (B_{min} *and* B_{max}), the corresponding quadrupole lens currents, the correction coil current, and the number of steps from B_{min} to B_{max} used to execute one cycle are set in correspondence to minimum and maximum momentum of electrons to be transmitted from the target zone to the 2D electron detector. After each measurement for a pass momentum p_n (*between* p_{min} *and* p_{max}) with a certain number of fillings of the ESR with beam extracted from SIS all spectrometer parameters are stepped to the next filling p_{n+1}. This stepping was initiated manually every time before a new series of fillings of the ESR is requested.

Electrons were detected in coincidence with the single projectile electron

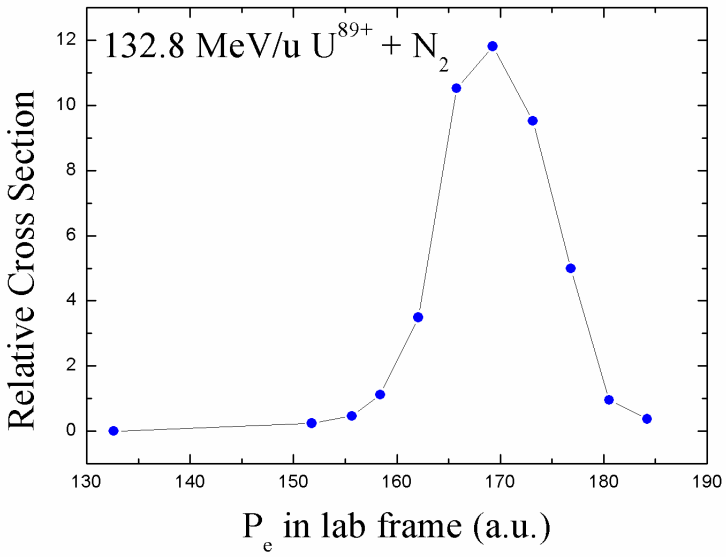

Figure 3.32: 0° binary encounter electron spectrum for 132.8 MeV/u U^{89+} + N_2.

loss channel U^{90+}. The spectrum is dominated by electrons ionized from the projectile into its low energy continuum by interactions with either the target nucleus or the target electrons. Figure (3.33) shows the resulting electron loss to continuum cusp. The observed width of the cusp $\Delta p/p = 19\%$ $(FWHM)$ is very large compared to the 1.9% theoretical momentum resolution of the spectrometer found using the MIRKO software. Apparently, this large width is caused by inappropriate settings of the focusing lens of the spectrometer.

3.6.2 The Electron Detector

A two dimensional position and time sensitive multi-hit capable electron detector with micro channel plate (MCP) and delay line anode configuration identical to that used in the reaction microscope (*see section* 3.5.2) was constructed and used for electron detection in the forward electron spectrometer. The electron detector is mounted 131.5 *cm* downstream of the second dipole magnet behind the momentum defining slits. The detector is mounted inside a spring bellow carried by a movable holder that runs on special rails (*figure* 3.34) to enable it to move away from the measuring position when required.

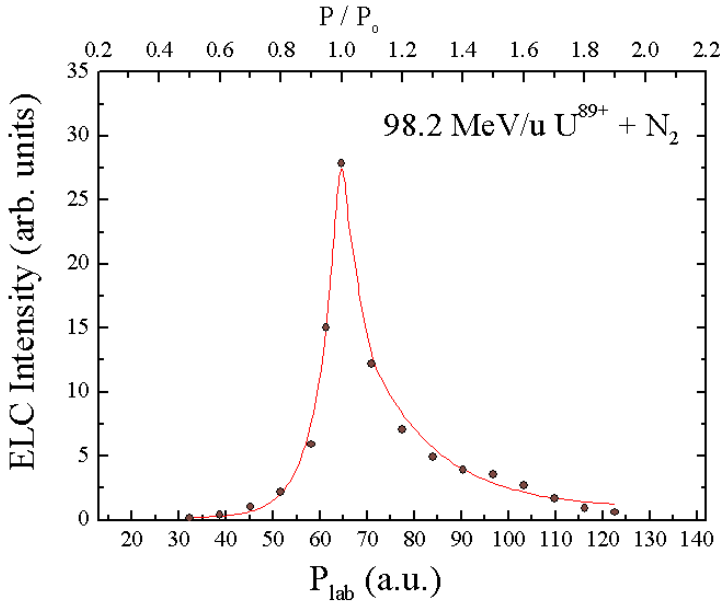

Figure 3.33: ELC cusp coincident with U^{90+} in (98.2 MeV/u) U^{89+} + N_2. The distribution is peaked at electron longitudinal momentum $p \approx 64.56$ a.u. corresponding to electrons traveling with the projectile velocity. The observed width of the cusp is $\Delta p/p$ = 19% ($FWHM$). The electron relative momentum ($p/p_\circ$) scale appears at the top of the figure.

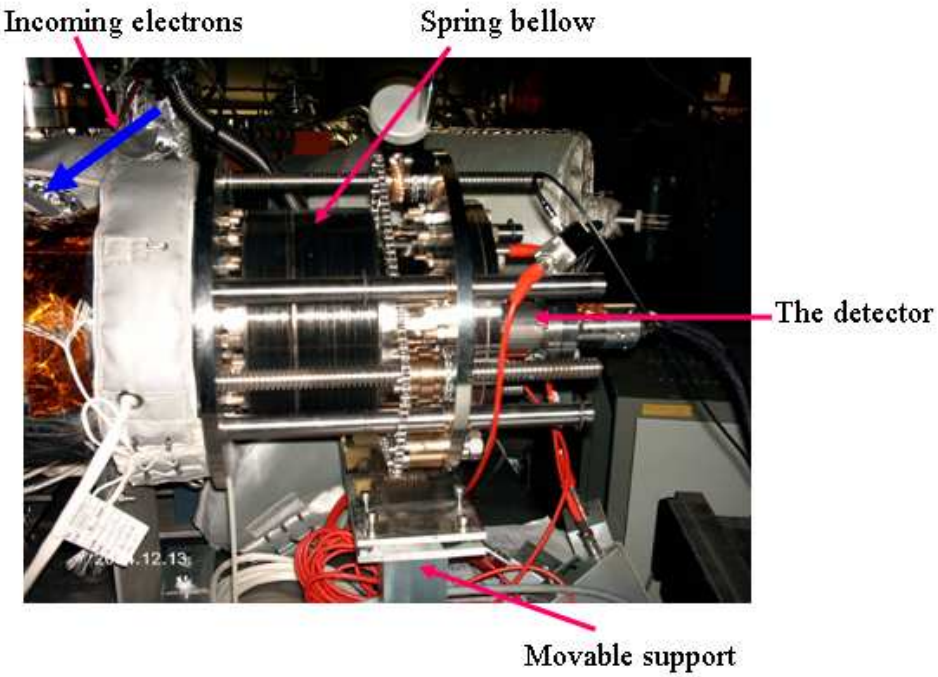

Figure 3.34: The electron detector mounted in the ESR inside a spring bellow carried by a movable holder.

3.6.3 The X-ray Detector

For the detection of photons, we have used in our experiment an *Eurisys* n-type planar germanium Ge(i) semiconductor detector mounted at an observation angle of 90° with respect to the beam direction (*see figure* 3.7). The primary advantage of semiconductors over other detectors is the small average energy needed to create charge carriers (*electron-hole pairs mentioned later*). For the same radiation energy, the number of electron-hole pairs created is approximated to be almost an order of magnitude greater in semiconductors than in gases [177].

The Ge semiconductor detectors are commonly used for measuring the X-ray spectra. However, the spectrum obtained with a Ge detector is an absorption spectrum since Ge is efficient as a photon absorber. In general, the germanium detector, similar to other semiconductor detectors, is a large reverse-biased p-n junction diode. At the junction between the p-type and n-type material, the migration of electrons from the n-type material and holes from the the p-type material gives rise to a region of net zero charge. This region is the depletion region. The net positive charge on one side of the junction, and the net negative charge on the other side, sets up an electric field gradient across the depletion region. Any photon interacting with the germanium crystal through any process like Compton scattering, Photoelectric effect, Pair production, ...etc, will produce electron-hole pairs in the depletion region, which will then be swept to the edges of the detector because of the electric field gradient, constituting an electric current. The photon energy required to create an electron-hole pair in Ge is approximately 3 eV, thus an incident photon, with an energy of several hundred keV, produces a large number of such pairs, leading to good detection efficiency and low statistical fluctuations.

The major characteristics of the Ge(i) detector we have used are listed in table (3.4). The Ge(i) detector is usually operated at a temperature of around 77 K, in order to reduce noise from electrons which may be thermally excited across the small band gap in Ge (0.67 eV) at room temperature. This is achieved through thermal contact of the Ge crystal with a dewar of liquid nitrogen.

Photons entering the Ge(i) detector traverse the 200 $\mu g/cm^2$ Beryllium

Operating high voltage	-3000 *volt*
Polarity	NEGATIVE
Measured resolution	0.75 keV at 122 keV
	and 1.75 keV at 1332 keV
Measured relative efficiency	7.8% at 1332 keV
Crystal external diameter	50 mm
Crystal length	20.5 mm
Crystal surface area	20 cm^2
Crystal distance from cap	5 mm
Crystal dead layer	$\leq$ 0.5 μGe
End cap diameter	80 mm
End cap length	80 mm
End cap thickness	$\leq$ 0.3 mm
Entrance window	Be (200 $\mu g/cm^2$)
Preamplifier Type	PSC 821

Table 3.4: Characteristics of the Germanium detector used in this experiment.

entrance window of the detector. The attenuation suffered by photons due to the presence of the beryllium window is estimated to be very small and can be neglected according to

$$\frac{I(x)}{I_\circ} = \exp(-\mu x) = 0.999969 \tag{3.69}$$

where $I_\circ$ is the incident beam intensity, $I(x)$ is the outgoing beam intensity, μ is the mass attenuation coefficient ($= 0.28749\ cm^{-1}$ *for Be at* 50 keV), and x is the thickness of absorber ($=1.08 \times 10^{-4}$ *cm for the beryllium window*). In general, beryllium is considered to be nearly 100% transparent for photons having energies more than 5 keV.

Energy calibration of the Ge(i) detector

As a first step before starting the experiment, the Ge(i) detector was calibrated with a radioactive americium ^{241}Am source. ^{241}Am has a half-life of 432.7 years

Line	Origin	Energy (keV)	Relative Weight	Weighted Average Energy(keV)	Channel
A	Np-L$_{\alpha 1}$ (L3 - M5)	13.95	100	13.93	604
	Np-L$_{\alpha 2}$ (L3 - M4)	13.76	11.8		
B	Np-L$_{\beta 1}$ (L2 - M4)	17.75	100	17.51	765
	Np-L$_{\beta 2,15}$ (L3 - N5)+(L3 - N4)	16.84	36.1		
C	Np-L$_{\gamma 1}$ (L2 - N4)	20.78			896
D	^{241}Am (6%)	26.34			1137
E	^{241}Am (94%)	59.54			2558

Table 3.5: Different spectral lines seen in the spectrum of ^{241}Am source used for the energy calibration of the Ge(i) detector.

and decays into neptunium (^{237}Np) through the emission of alpha particles and low energy gamma rays ($\approx 60\ keV$).

In the resulting spectrum (*lower part of figure* 3.35) we recognize the two americium spectral lines (*D and E*) with energies 26.34 keV and 59.54 keV and probabilities of 6% and 94% respectively. In addition the x-ray lines (*A,B, and C*) of neptunium are also recognized. Line A is a mixture of the two unresolved lines Np-Lα1 (L3 - M5) and Np-Lα2 (L3 - M4) with energies of 12.95 keV and 13.76 keV and of relative weight of 100:11.8 respectively. Line B is also a mixture of the two unresolved lines Np-Lβ1 (L2 - M4) and Np-L$\beta 2,15$ [(L3 - N5)+(L3- N4)] with energies of 17.75 keV and 16.84 keV and of relative weight of 100 : 36.1 respectively. Table (3.5) lists the different lines detected with their origin, energy, weight, and channel number. Energy values are taken from [178, 179] while relative probabilities are taken from [180].

A linear fitting of the spectral points (*upper half of figure* 3.35) gives a formula relating each channel number with its corresponding energy as:

$$E(eV) = 23.37 \times channel - 235.94 \tag{3.70}$$

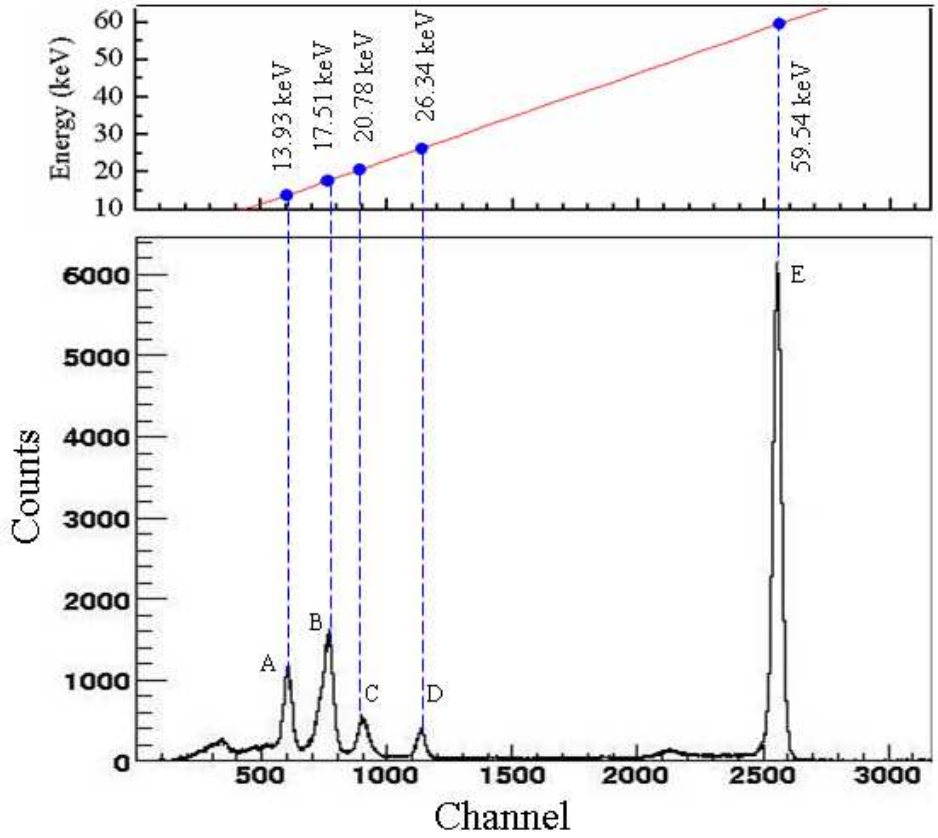

Figure 3.35: The spectrum of the ^{241}Am radioactive source used for calibration as recorded by our Ge(i) detector.

3.6.4 Signal Processing and Data Acquisition System

A block diagram of the electronics used in the present work is shown in figure (3.36). The signals are processed using a standard **NIM** electronics. The four timing signals from the delay-line anode are differentially amplified by means of a **RoentDek** type **DLATR6** module, converted to standard ECL pulses by constant fraction discriminators integrated inside the same module, and then measured by a fast time-to-digital convertor (*LeCroy TDC 3377*) with a time resolution of 0.5 *nsec*.

The time signal from the front of the MCP stack is first de-coupled from the DC-voltage using RC-element (R = 1 $M\Omega$, C = 4.7 nf) and then amplified by means of a fast linear amplifier (*GSI developed* ***FL8000***) then directed to an Ortec type constant fraction discriminator (*Ortec 934*) to be converted to standard NIM signal. The NIM signal is then converted to ECL signal by means of NIM-ECL converter (*GSI developed* EC 8000). The resulting signal is fed into the LeCroy 3377 TDC and is used as the common start signal for all of the TDC channels. The time signals from the Ge(i) detector and the particle detectors for projectile capture and loss, respectively are also fed into the same LeCroy 3377 TDC.

The currents of the Hall probes in the dipole magnets were fed through a 6 $M\Omega$ impedance into two GSI-developed NIM current digitizers (*model* CD 1012), the output signals of the current digitizers are then fed into a scaler (*LeCroy 2551*) to give a direct measure (*when normalized using the electronic clock*) of the electron momentum selected by the spectrometer. In order to measure the charge exchange rates seen by the particle detectors for normalization purposes, the time signals from both particle detectors are fed into the LeCroy 2551 scaler. The time signals of the electron and Ge(i) detectors are also counted with the same LeCroy 2551 scaler.

The energy signal of the Ge(i) detector is first amplified by a main amplifier then fed into an Ortec 442 linear gate stretcher then directed to a Silena 4418/V analog to digital coverter (ADC).

The LeCroy 3377 TDC, the Silena ADC, and the LeCroy 2551 scaler are integrated in a CAMAC crate. The data from the CAMAC crate are read out by the GSI developed CAMAC Processor board **GTBC4**, which was connected

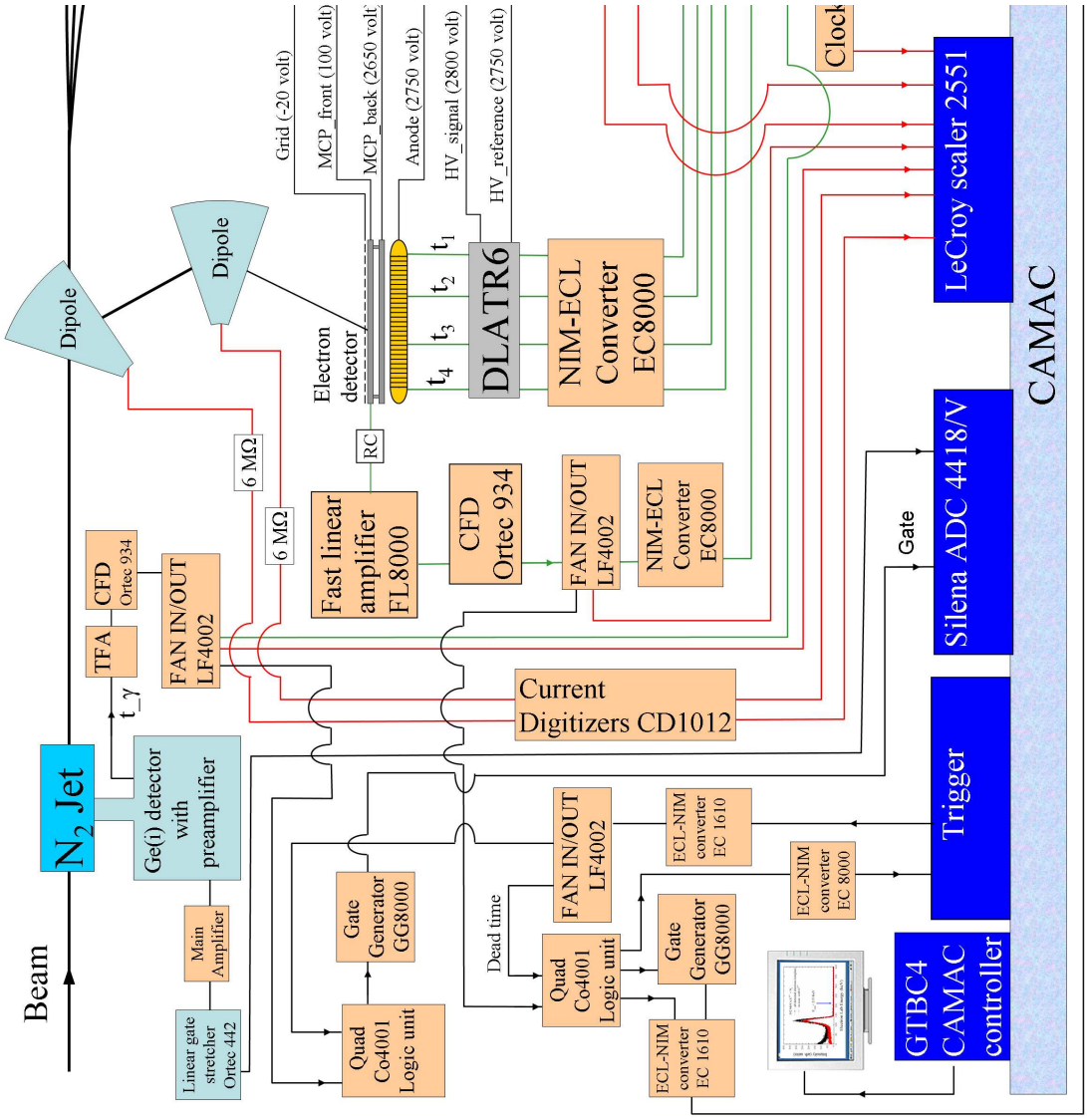

Figure 3.36: A block diagram of the Data acquisition system used in this work.

to a PC via an interface card. By means of The lynx-based data acquisition "MBS" (*Multi Branch System*) software which also has been developed at GSI, we controlled the data acquisition and stored the raw data in a so-called "LMD-file" (*GSI format*) event by event. This allows one to replay the experiment off-line. The on-line and off-line analysis of the raw data is performed using a special software "Go4" [181] which is developed also at GSI. Go4 enables the full data analysis and graphic representation of the analyzed data.

Chapter 4

Results and Discussion

Using our forward electron spectrometer described in the previous chapters, we have studied the forward electron emission and the radiative electron capture to continuum RECC in collisions of 90 MeV/u U^{88+} beryllium-like uranium impinging upon N_2 gaseous target. The 90 MeV/u beam energy is in the range in which the ECC and RECC components of the capture to continuum process have comparable cross sections [7] while the U^{88+} projectile was chosen for two main reasons : On the one hand, a full K-shell is required to prevent the dominant K-REC in the x-ray spectra. On the other hand, a projectile that carries electrons into the collision offers the advantage of a simultaneous study of the electron loss to continuum ELC channel. Additionally, the N_2 target ($Z_t = 7$) is more efficient than H_2 or He in providing larger cross section for RECC and bremsstrahlung since the cross section scales with Z_t (*see section* 2.2.2).

Time coincidences are recorded between electrons emitted in the forward direction and photons emitted at 90^o with respect to the beam direction (*figure* 4.1a), electrons and projectiles having experienced single electron loss U^{89+} (*figure* 4.1b), and electrons and down-charged projectiles U^{87+} (*figure* 4.1c).

The spectrometer was operated as follows: a measurement cycle in the interval [$p_{min} = 0.6p_\circ$, $p_{max} = 1.4p_\circ$] was chosen, where $p_\circ = 61.68$ a.u. is the momentum corresponding to electrons traveling with the projectile velocity at 90 MeV/u, and suitable number of steps to go from p_{min} to p_{max} was determined such that we go in larger momentum steps of $\Delta p = 0.05p_\circ$ in the

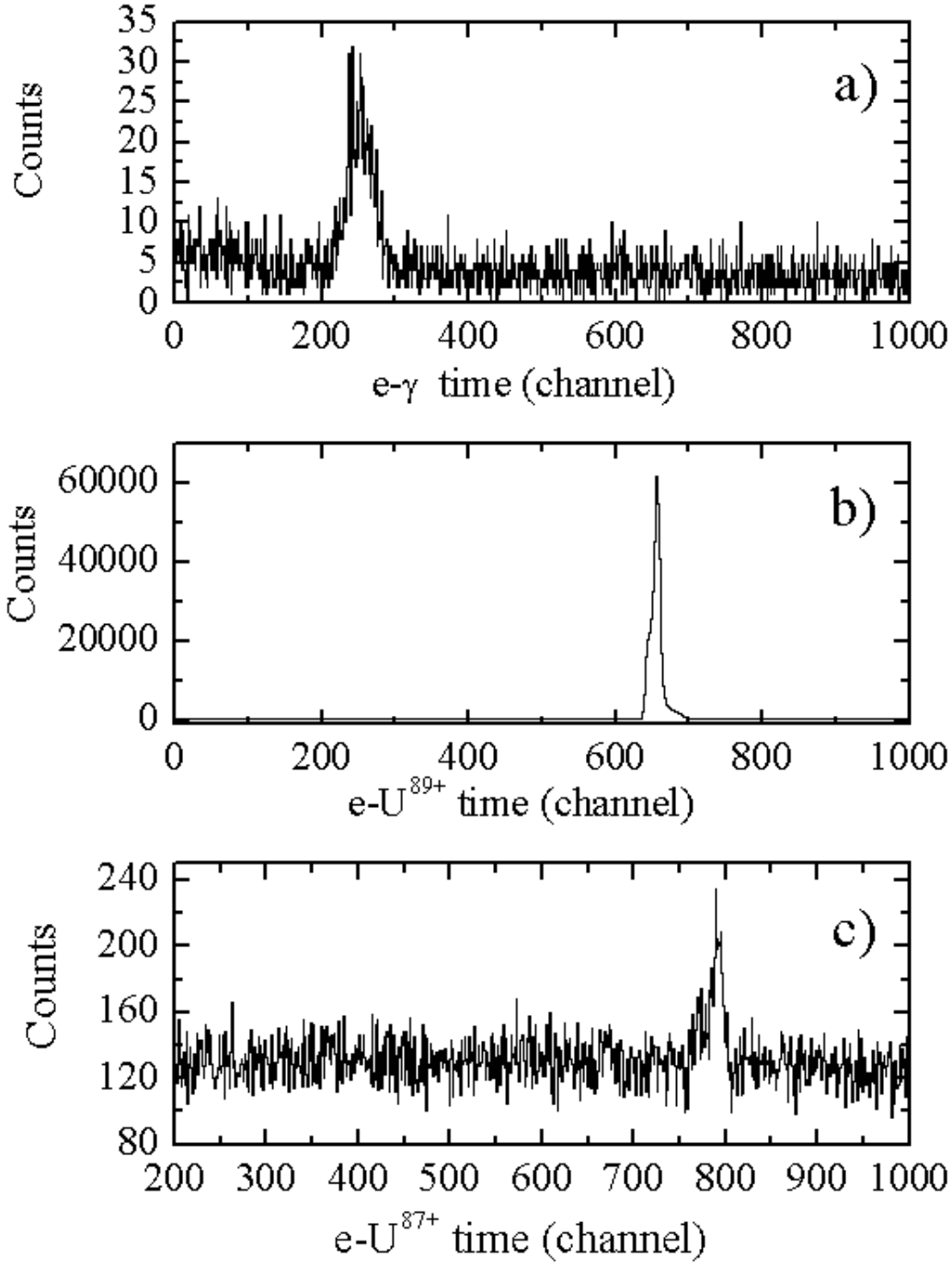

Figure 4.1: Collected time spectra at $v_e = v_{proj}$ for the coincidence between electrons emitted in the forward direction and a) photons emitted at 90^o with respect to the beam direction, b) up-charge projectiles U^{89+}, and c) down-charge projectiles U^{87+}.

energy range far away from the cusp energy and in smaller momentum steps of $\Delta p = 0.025 p_\circ$ in the energy range close to the cusp energy. In each step, a certain value of a pass momentum p_n (*between* p_{min} *and* p_{max}) is chosen for electrons to be transmitted from the target zone to the 2D electron detector. However, these momentum values used during the stepping procedure are only the nominal values given by the ESR software which are replaced during the data analysis by the actual momentum values deduced from the Hall probe currents registered by the LeCroy scaler. For each pass momentum p_n, the spectrometer is tuned by means of the ESR software at the suitable parameters, the two magnetic dipole currents, the quadrupole lens currents, and the correction coil current, for which, according to optics calculations, it only passes electrons centered at the chosen pass momentum p_n. After each measurement for a pass momentum p_n with a certain number of fillings of the ESR, all spectrometer parameters are stepped to the next pass momentum p_{n+1}. This stepping is to be initiated manually every time before a new series of fillings of the ESR is requested.

In order to minimize possible electronic dead time effects, the electron count rate was kept low (<2 *kHz*) and a dead time correction was performed for the number of counts of each step of the measurement cycle by taking into consideration the ratio of the number of electrons detected by the electron detector to that registered by the LeCroy scaler.

The error bars in the presented cross sections are due to statistical errors originating from counting rates. The 98% efficiency of the particle detector will result first in a systematic error of 2% in the ELC relative cross section (*figure* 4.3) corresponding to 4% error in the ECC cross section (*figure* 4.12) and second in a 2% error in the cross section for simultaneous electron capture to continuum and bound states (*figure* 4.9). Other possible sources of systematic error are: the momentum resolution of the spectrometer, the accuracy in the location of the electron detector (*centered* ± 2 *mm from the beam line axis*), the dead time of the micro channel plates, the accuracy in the 90° angle of the Ge(i) detector, the pile-up of photons in the Ge(i) detector, the accuracy in the jet beam location, the volume of overlap between the beam and the jet, the residual gas effect, the electronic dead time, and chance coincidences.

The systematic error resulting from all these sources is expected to be small in comparison with the error resulting from particle detector efficiency and can be neglected in the present measurement where we measure relative cross sections but should be taken into account in the measurement of absolute cross sections in our future work. Compton scattering is not to be expected at the present photon energies ($E_\gamma \approx 50\ keV$).

4.1 Electron Cusp Distribution

Figure (4.2) represents the measured momentum spectrum of all projectile continuum electrons (*singles*) emerging from the target chamber and detected by the electron detector without coincidence conditions applied.

$$U^{88+}(1s^2 2s^2) + N_2 \rightarrow U^{q+} + (N^{q+*}) + e^-_{cusp}$$

The electron yield measured by the electron detector for every pass momentum p_n is normalized to the charge exchange rate seen by the particle detector for projectiles having undergone single electron capture. The resulting electron spectrum shows a nearly symmetric cusp-shaped distribution centered at an electron momentum corresponding to electrons traveling with the projectile velocity in agreement with theoretical and experimental foundings concerning electron transfer to continuum [4, 69].

4.2 Electron Loss to Continuum ELC

Since the projectiles $U^{88+}(1s^2 2s^2)$ carry electrons into the collision, they can be ionized by the excitation of one or more electrons from the initial projectile bound state to a low-lying projectile continuum states just above the ionization limit due to an interaction with either the N_2 nucleus or N_2 electrons. In the course of the present experiment, we have studied the single electron loss to continuum process. This was accomplished by measuring the coincidence between electrons emitted in the forward direction and the up-charged projectiles U^{89+}. Since we are not measuring coincidences between electrons emitted

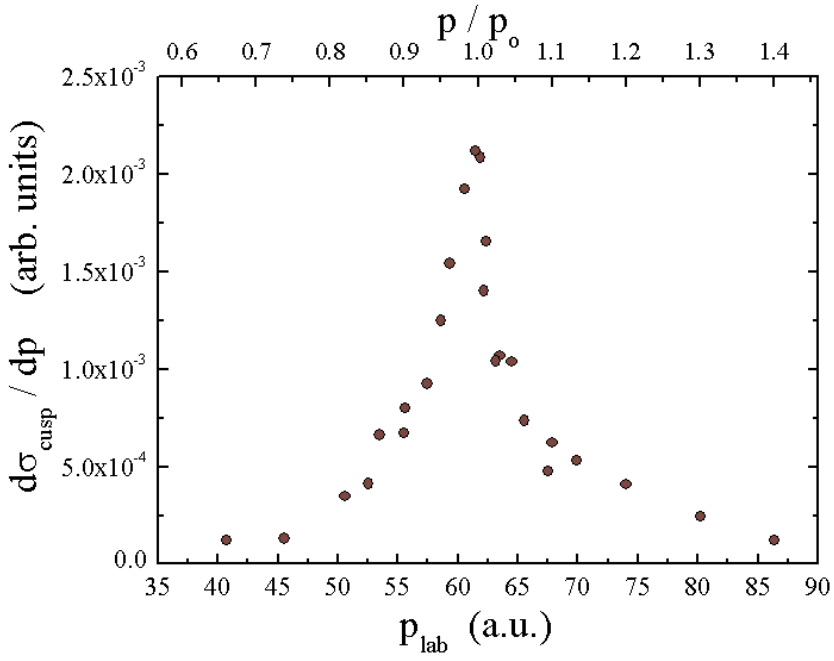

Figure 4.2: Singles electron yield emitted near 0° with respect to the beam direction as a function of longitudinal electron momentum along the beam direction ($p = \beta\gamma/\alpha$) in the laboratory frame for 90 MeV/u U^{88+} ions incident on N_2 gaseous target. The cusp yield is peaked at $p \approx 61.68$ a.u. corresponding to electrons traveling with the projectile velocity. The momentum range covered corresponds to laboratory electron energies between $\sim$22 keV and $\sim$93 keV. The electron relative momentum ($p/p_\circ$) scale appears at the top of the figure.

in the forward direction and U^{q+} $(q = 90, 91, 92)$ projectiles, we are not able in this work to provide experimental results on the multiple electron loss process where two or more electrons are ionized simultaneously from bound projectile states to continuum states.

For 90 MeV/u U^{88+} projectiles, single electron loss to continuum from the projectile originates mostly from the L-shell ($2s$ *orbital*). It was calculated [182] that only in 10% of the times are electrons ionized from the K-shell ($1s$ *orbital*).

$$U^{88+}(1s^2 2s^2) + N_2 \rightarrow [U^{89+}(1s^2 2s^1) + e^-_{cusp}] + N_2$$

The yield of electrons resulting from the single loss to continuum channel for every pass momentum p_n of the measurement cycle was deduced from the area under the time spectrum representing the electron-U^{89+} coincidence (*figure* 4.1b) after fitting and background subtraction using the Jandel Scientific PEAKFIT v4.0 software package. Each value of ELC yield is normalized to the corresponding charge exchange rate seen by the particle detector for projectiles having undergone single electron capture. The resulting electron ELC spectrum (*figure* 4.3) shows a nearly symmetric cusp confirming the symmetry of longitudinal ELC cusps, as it results from the first-Born treatment of Day [79] and Briggs and Day [82]. The width of the peak ($FWHM$) of $\Delta p = 4.5$ $a.u.$ corresponds to the instrumental momentum resolution of the spectrometer of 1.9% folded with the theoretical cusp width.

It also deserves attention that no photons were detected in coincidence with the ELC electrons which leads to the conclusion that ELC is predominantly not accompanied by a simultaneous radiative capture to continuum process. This can be attributed to the difference in nature of collisions resulting in ELC or RECC events: a soft collision with a small momentum transfer $q \geq q_{min} \cong \epsilon_i / v_{proj}$ is enough in the case of ELC while the RECC event is a result of a violent collision with large momentum transfer in the range of that needed for ECC process $q_{min} \cong v_{proj}$ (*see chapter 2*).

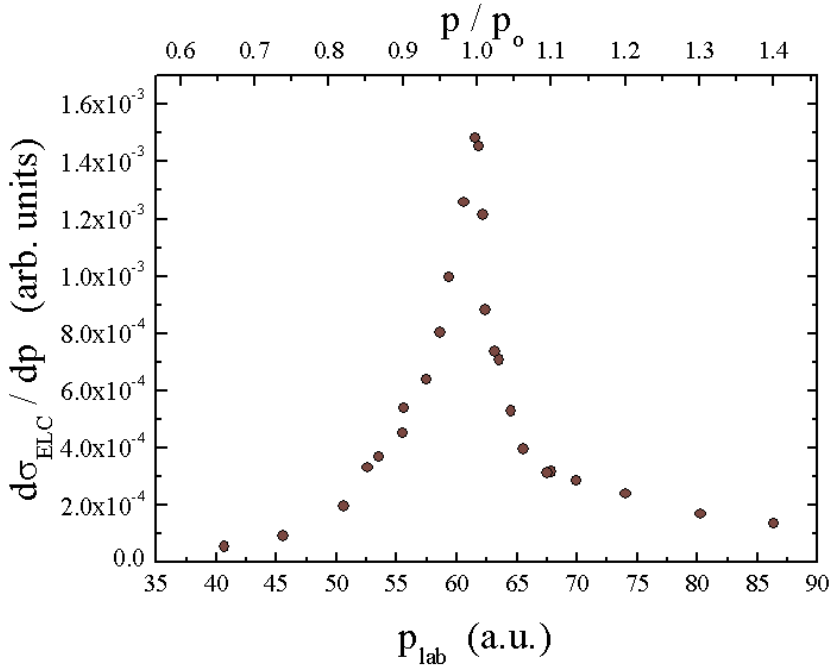

Figure 4.3: Electron yield emitted near 0° with respect to the beam direction coincident with U^{89+} (ELC) as a function of longitudinal electron momentum along the beam direction ($p = \beta\gamma/\alpha$) in the laboratory frame for 90 MeV/u U^{88+} ions incident on N_2 gaseous target. The distribution is peaked at $p \approx 61.68$ a.u. corresponding to electrons traveling with the projectile velocity. The electron relative momentum ($p/p_\circ$) scale appears at the top of the figure.

Transition	$E_{emitter}$ (keV)	E_{lab} (keV)	Transition Probability (s^{-1})	Note
$2p_{\frac{3}{2}} \rightarrow 2s_{\frac{1}{2}}$	4.491	4.095	1.14×10^{14}	L shell internal transition
$4d_{\frac{3}{2}} \rightarrow 3p_{\frac{1}{2}}$ $(\,^3D_1 \rightarrow \,^3P_0)$	6.719	6.127	2.01×10^{14}	Paschen Series
$3s_{\frac{1}{2}} \rightarrow 2p_{\frac{3}{2}}$ $(\,^1S_0 \rightarrow \,^1P_1)$	14.099	12.857	7.04×10^{14}	Balmer Series
$3d_{\frac{5}{2}} \rightarrow 2p_{\frac{3}{2}}$ $(\,^3D_3 \rightarrow \,^3P_2)$	15.849	14.453	3.90×10^{15}	
$3d_{\frac{3}{2}} \rightarrow 2p_{\frac{1}{2}}$ $(\,^3D_1 \rightarrow \,^3P_0)$	19.654	17.922	2.58×10^{15}	
$4d_{\frac{3}{2}} \rightarrow 2p_{\frac{1}{2}}$ $(\,^3D_1 \rightarrow \,^3P_0)$	25.113	22.900	9.33×10^{14}	

Table 4.1: Most probable characteristic transitions for U^{88+} and their transition probabilities.

4.3 X-ray Energy Spectra: Short Wavelength Limit of Electron Nucleus Bremsstrahlung

In figure (4.4) we compare the measured x-ray spectrum at 90° with respect to the beam direction accumulated without any coincidence conditions with the x-ray spectrum coincident with cusp electrons, electrons traveling with the projectile velocity. X-ray energies in the laboratory frame were calculated using the calibration (*equation* 3.70) mentioned previously in chapter 3. In the spectrum, the discrete lines of the characteristic projectile radiation, mainly M and L x-ray emission attributed to the excitation of the U^{88+} projectiles, can be seen together with REC into the L- and M- shells. K-REC as well as characteristic K-shell x-rays of the projectile are not present here due to the occupied K-shell of the U^{88+} projectile. The projectile characteristic lines, as shown, are superimposed over a continuum x-ray spectrum due to the electron-nucleus bremsstrahlung of target electrons in the projectile potential. The most probable projectile characteristic lines leading to the measured spectral lines of figure (4.4) were calculated by Xincheng Wang (*Fudan University, Shanghai*) using the MCDFGME sofware package [183] and listed in table (4.1)

Photons are emitted by uranium ions moving with velocities of about 41%

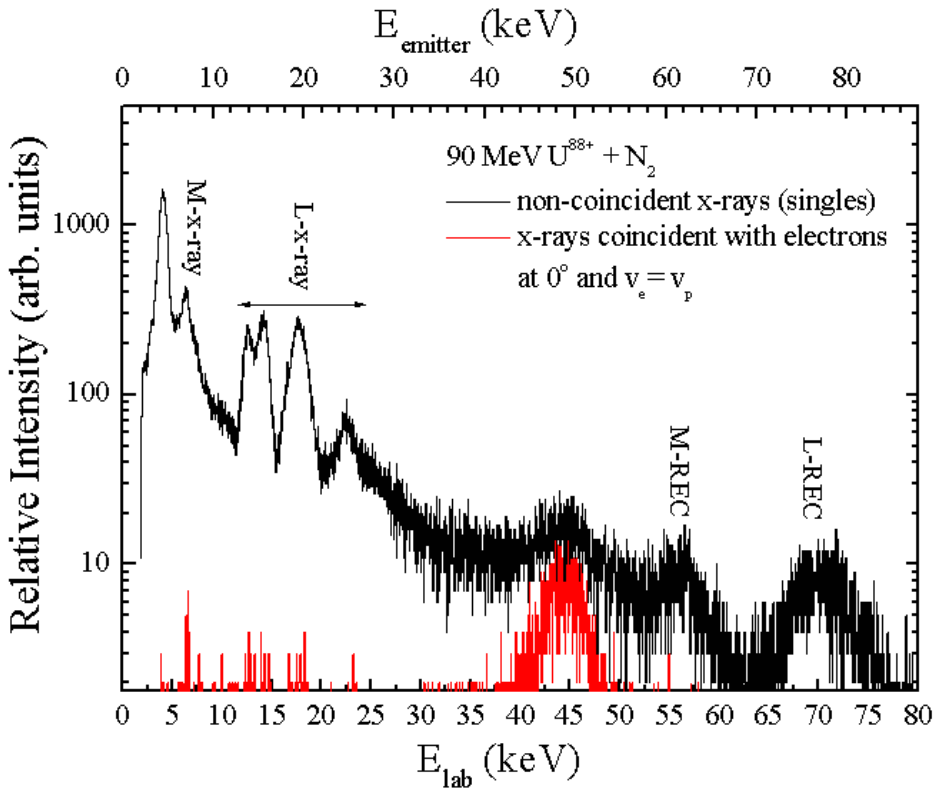

Figure 4.4: X-ray spectrum coincident with RECC electrons (*lower red line*) compared with the singles x-ray distribution (*upper black line*) detected under 90° with respect to the beam axis for 90 MeV/u U^{88+} ions incident on N_2 gaseous target.

of the speed of light, therefore photon energies measured in the laboratory system have to be corrected for the relativistic Doppler shift using [56]

$$E_{emitter} = E_{lab} \times \gamma \times (1 - \beta \cos\theta_{lab}) \tag{4.1}$$

where $E_{emitter}$ and E_{lab} are the photon energies in the emitter and laboratory systems, respectively, θ_{lab} denotes the laboratory observation angle ($90°$*in this work*), β is the speed in units of the speed of light and γ is the relativistic Lorentz factor $\frac{1}{\sqrt{1-\beta^2}}$. The calculated emitter frame energies appear at the upper scale of the spectrum.

The coincident x-ray spectrum, given as the red line of figure (4.4), collected in coincidence with electrons emitted in the forward direction with the same velocity as the projectile $v_e = v_{proj}$ is plotted together with the non-coincident spectrum. While the non-coincident spectrum is dominated by projectile M and L x-ray emission, the coincident spectrum almost exclusively contains x-rays at $E_{lab} \approx 45\ keV$ corresponding to $E_{emitter} \approx 49.4\ keV$ which confirms the interpretation viewed by an observer in the projectile system as the short-wavelength limit of the electron-nucleus bremsstrahlung from $e^- + U^{88+}$ at $(\gamma - 1)mc^2 = 49.4\ keV$ incident kinetic electron energy

In the coincident x-ray spectrum, the observed line width of the x-ray peak is due mostly to Doppler broadening of radiation in the x-ray detector. Our 2000 mm^2 Ge(i) x-ray detector located 140 mm away from the target subtended approximately 9.5° in the laboratory, giving a Doppler width as derived from equation (4.1)

$$\Delta E_{lab} = \frac{E_{lab}\beta \sin\theta_{lab}}{1 - \beta\cos\theta_{lab}}\ \Delta\theta_{lab} \tag{4.2}$$

equal to 3.06 keV for 90 MeV/u U^{88+} ions at $\theta = 90°$ with respect to the beam direction.

In figure (4.5), the experimental coincident x-ray spectrum coincident with electrons emitted in the forward direction with the same velocity as the projectile ($v_e = v_{proj}$) is plotted together with the theoretical results (*full circles*) calculated by Doris Jakubaßa-Amundsen (*LMU München*) for our system obtained from the fourfold differential cross section by integrating over the forward electron acceptance cone and energy resolution of the spectrometer. In

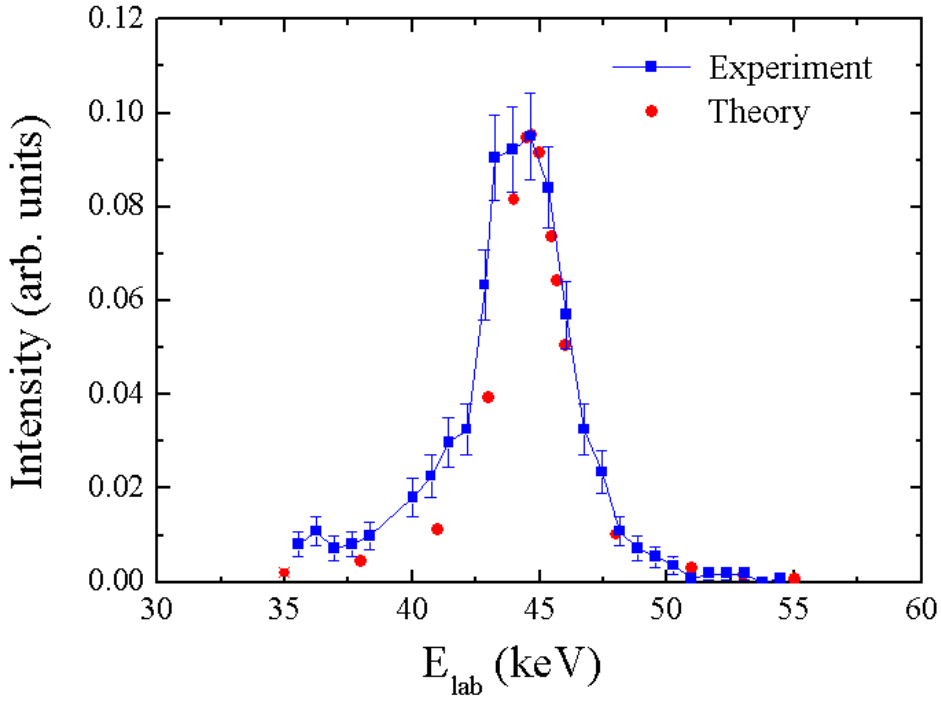

Figure 4.5: Experimental x-ray spectrum (*full squares*) coincident with electrons emitted in the forward direction at the same velocity as the projectile in comparison with theorey (*full circles*) for 90 MeV/u U^{88+} ions incident on N_2 gaseous target.

order to put the obtained relative cross section data on the calculated absolute scale, the measured spectrum is normalized to the theory in the peak maximum. There, the shape of the cross sections are generally found to be in very good agreement with theoretically calculated ones. The FWHM of the measured cross sections of 4.04 keV is in good agreement with the 4.2 keV width expected from a quadratic sum of both the 2.87 keV theoretical peak width and the 3.06 keV Doppler broadening assuming Gaussian contributions

$$\Delta E_{exp} = \sqrt{\Delta E_{Dopp}^2 + \Delta E_{theo}^2} \tag{4.3}$$

4.4 Radiative Electron Capture to Continuum RECC

In order to investigate the double differential cross section ($\frac{d^2\sigma}{dpd\Omega}$) for the RECC process, we have collected x-ray spectra coincident with electrons emitted in the forward direction for a set of electron momenta ($53.5\ a.u. < p_e < 67.5\ a.u.$) corresponding to electron velocities velocities ($50\ a.u. < v_e < 60.5\ a.u.$) close to the projectile velocity of $v_p = 56.24\ a.u.$. The resulting coincident spectra (*figure* 4.6) show that x-ray spectra coincident with electrons at laboratory velocities slightly lower than the cusp velocity contain much lower x-ray intensity than x-ray spectra coincident with electrons at laboratory velocities slightly higher than the cusp velocity. This leads to a strong asymmetry of the differential cross section toward the high energy side of the electron cusp distribution coincident with the RECC process. Relative differential cross sections for RECC were obtained by normalizing the number of counts of each coincident spectrum to the corresponding charge exchange rate seen by the particle detector for projectiles having undergone single electron capture.

Figure (4.7) shows the resulting measured relative double differential cross section DDCS (*full circles*) for radiative electron capture to the projectile continuum RECC :

$$U^{88+}(1s^2 2s^2) + N_2 \rightarrow U^{88+}(1s^2 2s^2) + (N_2^{+*}) + e^-_{cusp} + h\nu$$

which is derived from coincident spectra of figure (4.6). The relative DDCS exhibits a cusp-shaped distribution peaked at electron momentum corresponding to electrons traveling with the projectile velocity. The experimental peak position at $p_e = \gamma v_p = p_\circ$ with its asymmetry is compatible with the theoretical picture given in chapter 2 of this work, for an observer in the U^{88+} projectile frame the incident electron is decelerated from an average momentum $p_\circ$ to a momentum ≈ 0; its total kinetic energy being carried away by the emitted x-ray photon. The electron bounces back from the projectile and thus appears predominantly in the beam direction. Comparison is made with theoretical RECC cross section calculations (*full line*) carried out by Doris Jakubaßa-Amundsen (*LMU München*). The theoretical cross section is ob-

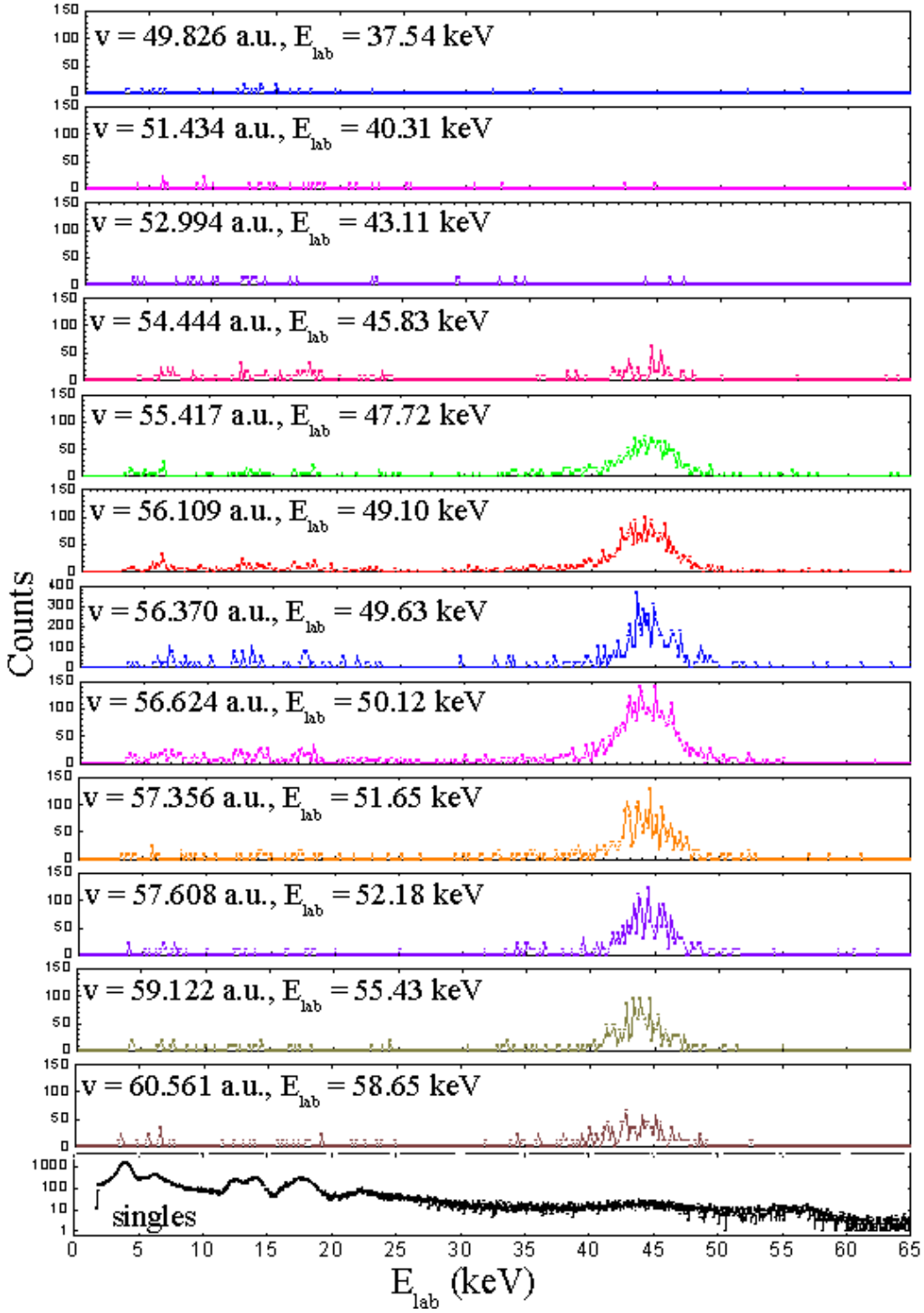

Figure 4.6: X-ray spectra collected in coincidence with electrons emitted in the forward direction for a set of electron velocities in the laboratory frame (*around the cusp velocity of 56.24 a.u.*) for 90 *MeV/u* U^{88+} ions incident on N_2 gaseous target. It is clearly seen that only coincidences with x-rays from the short wavelength limit of the electron nucleus bremsstrahlung appear; it is very apparent that mostly electrons with projectile frame momenta parallel to the incident projectile, having velocities slightly greater than the cusp velocity, are generating coincidence events.

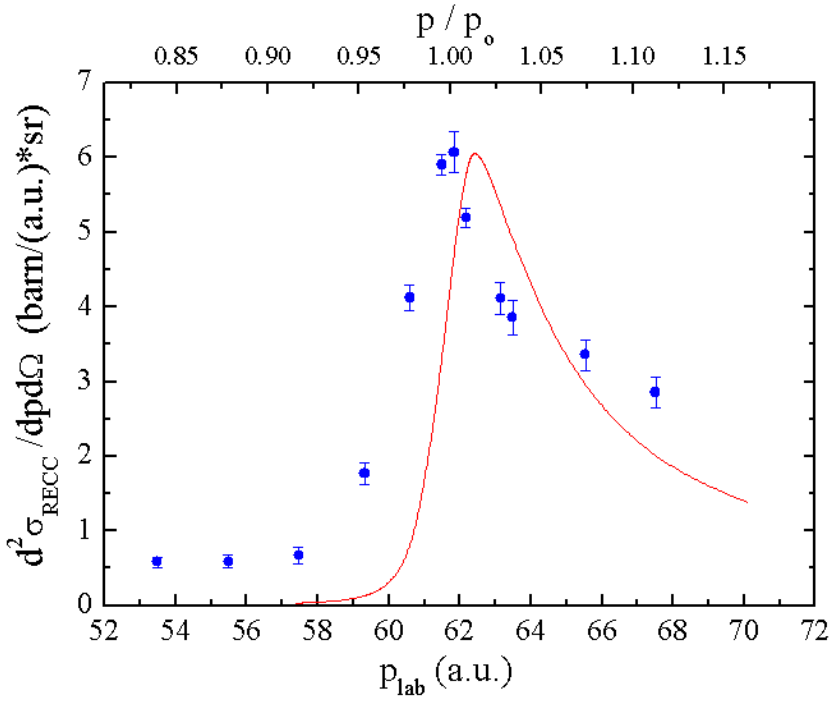

Figure 4.7: Relative differential cross section for radiative electron capture to continuum RECC in comparison with theory (*full line*) as a function of longitudinal electron momentum along the beam direction ($p = \beta\gamma/\alpha$) in the laboratory frame for 90 MeV/u U^{88+} ions incident on N_2 gaseous target. The distribution is peaked at $p \approx 61.68$ a.u. corresponding to electrons traveling with the projectile velocity. The theory is folded with the experimental momentum resolution and the experimental relative cross section is normalized to the maximum of the theoretical differential cross section. The electron relative momentum ($p/p_\circ$) scale appears at the top of the figure.

tained by folding the cross section for electron-nucleus bremsstrahlung with the momentum distribution of the electron in its initial state. This was performed within a relativistic formulation of the impulse approximation using semi-relativistic Sommerfeld-Maue wavefunctions for the ejected electron, i.e. solution of the Dirac equation under the assumption of a pure coulomb field of the nucleus and low atomic number ($\alpha Z << 1$)[38]. McDowell [184] and Briggs [185] have pointed out that for very asymmetric systems where the electron spectrum originates from electrons which move predominantly in the projectile field, the impulse approximation may be applied which includes the strong field (*projectile field*) to all orders and the weak field (*target field*) to first order. This applies to the present case.

Two fundamental assumptions are made for molecular N_2 target within the relativistic impulse approximation: (1) the N_2 target system has a diffuse structure such that the inter-particle distances are large compared with the range of nuclear forces. So, the N_2 target can be regarded as transparent and the amplitude of the wavefunction of the incident U^{88+} ions is not appreciably perturbed in crossing the target system. The near particles of the target system do not cast shadows on the far ones. (2) The interaction occurs over such a short time that the orbital time of the N_2 electron in its initial orbit is considered to be long compared with its interaction time with the incident U^{88+} ions. In this situation the effect of the binding forces during the collision may be neglected. In other words, the loosely bound N_2 electrons are treated as quasifree particles.

The approximations introduced here for the theoretical calculations are well justified and do not affect our basic conclusions. Since we deal with light targets $Z_P >> Z_T$ where Z_P and Z_T are the nuclear charges of projectile and target, respectively, and projectiles moving much faster than the target electrons according to their classical orbiting velocity, $\frac{1}{2}mv^2 >> E_{binding}$, it is safe to neglect the binding energy compared to the electron's kinetic energy in the projectile frame of reference. This also allows for the omission of the electron-target interaction not only in the final electron state, but also in the intermediate states, in particular since we deal with electron capture to continuum where in the final state the relative velocity between the electron and

the projectile approaches zero.

Concerning the use of the Sommerfeld-Maue wavefunctions for the ejected electron, this is certainly a reasonable approximation in the weakly relativistic case according to Shaffer *et al* [186]. Thus the cusp shape is not altered by the use of these functions. For projectiles with high nuclear charge, Sommerfeld-Maue wavefunctions are always expected to give reasonable reliable results [7].

The theory is averaged over the energy resolution of the photon detector ($\Delta E/E = 0.006$) and the theoretical momentum resolution of the forward electron spectrometer $\Delta p/p = 1.9\%$. Since the data are only relative, the experiment is normalized to theory at the cusp maximum. The pronounced peak asymmetry emphasizes the high energy slope of the cusp (*enhancement of emission of electrons parallel to the beam direction*), in accordance with theory [7].

We observe that the maximum of the theoretical DDCS for RECC shifts to slightly higher electron laboratory momenta than that seen experimentally. The shift of the theory away from the true cusp position $p_\circ$ is due to the strong underlying cusp asymmetry: Any folding of an asymmetric shape function S with a resolution function R will shift the maximum of the resulting curve into the direction of the gentler slope of S, and this shift will increase with increasing $\Delta p/p$. However, a contribution in the experimental DDCS not accounted for by theory could originate from electrons which are captured into Rydberg states of the projectile and subsequently are field ionized in the 60° magnet: If radiative electron capture can occur into continuum states lying just above the ionization threshold of the projectile, radiative capture into bound states lying just below the ionization threshold also can occur with comparable probability [187]. This means that Rydberg atoms may emerge from the target zone with comparable intensity as the RECC electrons. Rydberg atoms can be ionized in the Lorentz field of the first 60° dipole magnet of the spectrometer. One can estimate the maximum principal quantum number for electrons not to be file-ionized in the dipole as follows: A hydrogen-like ion (*atomic number* Z) in a Rydberg state n with an energy $E_n = -\frac{Z^2}{2n^2}$ will be exposed to the motional electric field E_m of strength

$$E_m = \gamma v_{proj} B = \gamma \beta c B \tag{4.4}$$

seen by the ions when moving with velocity v_{proj} in the transverse magnetic field B of the dipole. Here c is the speed of light and γ is the relativistic factor $(1/\sqrt{1-\beta^2})$. Rydberg electrons can just escape when the maximum $U(r_\circ)$ of the resulting potential

$$U(r) = -\frac{Z}{r} - E_m r \tag{4.5}$$

corresponds to the energy E_n [$U(r_\circ) = E_n$]. The maximum $U(r_\circ)$ of the potential is characterized by

$$\frac{dU(r_\circ)}{dr} = 0 \tag{4.6}$$

from which results

$$r_\circ = \sqrt{\frac{Z}{E_m}} \qquad \text{and} \qquad U(r_\circ) = -2\sqrt{ZE_m} \tag{4.7}$$

which leads to the result

$$n = \sqrt[4]{\frac{Z^3}{16E_m}} \tag{4.8}$$

which can be written (*with the help of equation* 4.4) as

$$n = \frac{1}{2}\sqrt[4]{\frac{Z^3}{\gamma\beta c B}} \tag{4.9}$$

from which we can estimate that the spectrometer filed will ionize all electrons captured into bound states with n values grater than about 450. This supplemental part of the spectrum is centered at $p_e = p_\circ$ and is not shifted by folding with R; its inclusion in a theoretical calculation would reduce the difference between the experimental and theoretical peak positions. It is highly unlikely that the experimental RECC peak position is due to a spectrometer deficiency: The simultaneously measured ELC cusp (*figure* 4.3) exhibits its maximum at $p_e = p_\circ$ as expected, the same electron momentum as the experimental RECC cusp.

4.5 Simultaneous Electron Capture to Bound and Continuum States

In order to determine the differential cross section for the pure single electron capture to continuum

$$U^{88+}(1s^2 2s^2) + N_2 \rightarrow U^{88+}(1s^2 2s^2) + (N_2^{+*}) + e^-_{cusp}$$

which cannot be measured directly, we turn to a multi-electron channel of the electron capture to continuum, were the U^{88+} projectile have captured simultaneously two electrons, one into the 2p shell and another into a low lying continuum state (*figure* 4.8).

$$U^{88+}(1s^2 2s^2) + N_2 \rightarrow U^{87+}(1s^2 2s^2 2p^1) + (N_2^{q+*}) + e^-_{cusp}$$

This process is investigated by the detection of electrons emitted in the forward direction at 0° in coincidence with the down-charged projectiles U^{87+}. The relative differential cross section ($\frac{d^2\sigma}{dpd\Omega}$) for this simultaneous capture for every pass momentum p_n of the measurement cycle is derived from the area under the coincident time spectrum representing the electron-U^{87+} coincidence (*figure* 4.1c) after fitting and background subtraction. The values are normalized to the corresponding charge exchange rate seen by the particle detector for projectiles having undergone single electron capture. We observe in the resulting spectrum of continuum electrons (*figure* 4.9) a cusp-shaped distribution peaked at electron momentum of ≈ 61.68 *a.u.* corresponding to electrons traveling with the projectile velocity and skewed towards the low energy side of the cusp which points towards a non-radiative capture to continuum accompanied by single electron bound state capture as the active mechanism.

On the other hand, a correlated double electron capture to highly excited bound states of the U^{88+} projectile as

$$U^{88+}(1s^2 2s^2) + N_2 \rightarrow U^{86+}(1s^2 2s^2 nl) + (N^{q+*})$$

with subsequent autoionizing transition via electron and/or photoemission to

$$U^{87+}(1s^2 2s^2 2p^1) + (N^{q+*}) + e^-_{cusp} + h\nu$$

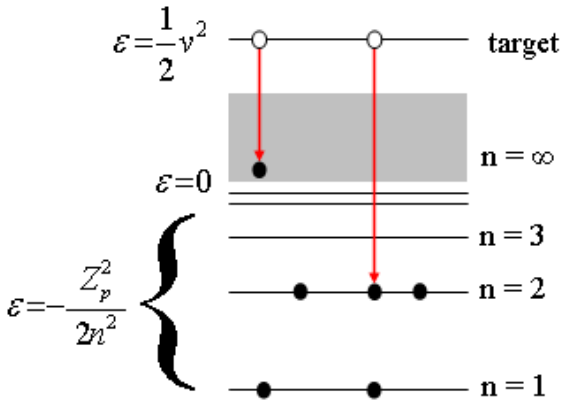

Figure 4.8: Schematic of the non-radiative electron capture to projectile continuum accompanied by a simultaneous bound state capture.

which leaves the projectile in a final charge state U^{87+}, may also contribute as the final state is identical to that for simultaneous continuum and bound state capture without correlation. This correlated electron capture and transfer ionization TI have been seen [95] to be very strong and even dominant at low collision velocities (0.53 MeV/u $F^{8+} + Ne$). However, at 90 MeV/u it is still surprisingly present but the asymmetric cusp shape of the observed distribution disproves such a correlated double capture process as the dominant channel, as it would lead to a symmetric peak, and supports the identification as simultaneous continuum and bound state capture. There is at present no theoretical approach to describe the simultaneous correlated capture. Simultaneous capture without correlation at relativistic velocities as the asymmetry may indicate to be here, has not been treated theoretically either.

4.6 Pure Electron Capture to Continuum ECC

Since a coincidence between electrons emitted in the forward direction and charge-unchanged projectiles (U^{88+}) is not possible from the practical point of view for a circulating beam in a storage ring, the relative double differential cross section ($\frac{d^2\sigma}{dpd\Omega}$) for the non-radiative electron capture to continuum ECC:

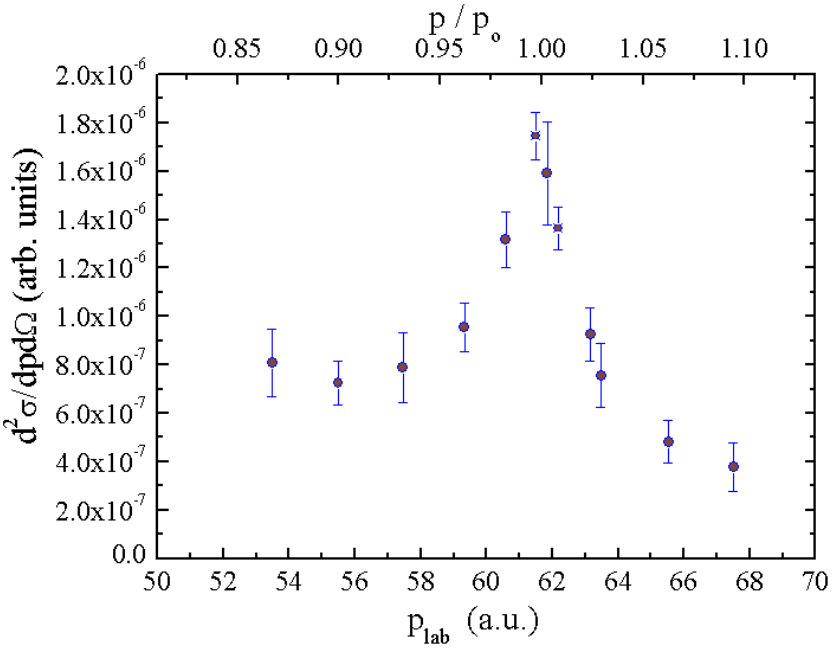

Figure 4.9: Non-radiative electron capture to projectile continuum cusp coincident with bound state capture for 90 MeV/u U^{88+} ions incident on N_2 gaseous target. The electron relative momentum ($p/p_\circ$) scale appears at the top of the figure.

$$U^{88+}(1s^2 2s^2) + N_2 \rightarrow U^{88+}(1s^2 2s^2) + (N_2^{+*}) + e^-_{cusp}$$

cannot be measured directly via electron-projectile coincidences as is possible for the corresponding ELC with coincidences of cusp electrons with U^{89+} projectiles. Taking into account the near 100% detection efficiency for charge changed projectiles in the particle detectors [188], estimation of the the relative cross section can be alternatively accomplished by subtracting from the non-coincident relative differential cross section for forward electron emission, that is all electrons detected by the electron detector, the relative differential cross sections for all other possible processes contributing to forward electron emission other than the ECC: ELC, RECC, and the small contribution of the simultaneous electron capture to bound and continuum states TI.

$$\frac{d^2\sigma_{_{ECC}}}{dpd\Omega} = \frac{d^2\sigma_{_{singles}}}{dpd\Omega} - [\ \frac{d^2\sigma_{_{ELC}}}{dpd\Omega} + \delta \times \frac{d^2\sigma_{_{RECC}}}{dpd\Omega} + \frac{d^2\sigma_{_{TI}}}{dpd\Omega}\ ] \tag{4.10}$$

To remove RECC counts from the singles, the number of RECC counts detected by the x-ray detector (*at* 90° *with respect to the beam direction*) should be multiplied by a factor δ to account for the fact that the x-ray detector spans only a small part of the entire 4π solid angle and therefore detects only a small part of the total radiation emitted. The factor δ is calculated as follows: the x-ray detector covers 2000 mm^2 active area and is positioned 140 mm away from the target zone. This corresponds to a solid angle of $\Delta\Omega/4\pi = 8.8 \times 10^{-3}$. The calculated half-opening polar angle $\Delta\phi$ around the 90° is 9.548°. Since the opening cone of the detector is spherically symmetric, also the half-opening azimuthal angle $\Delta\theta$ is the same, 9.548°. So instead of a total of 2π in the polar direction one has the difference between $90° + 9.548° = 99.548° = 1.737\ rad$ and $90° - 9.548° = 80.452° = 1.404\ rad$ which is 0.333 rad leading to a reduction by $0.333/2\pi = 0.053$. The corresponding reduction in the azimuthal angle depends on the the angular distribution of the emitted photons. This angular distribution can be obtained from the calculations of the double differential cross section $\frac{d^2\sigma_{ion-atom}}{dE_{lab}d\Omega_{lab}}$ for bremsstrahlung in collisions of 90 MeV/u U^{88+} and N_2 target at all possible laboratory angles from $\theta = 0$ to $\theta = \pi$. This can be done using equation (2.34) and tables of electron bremsstrahlung cross sections for neutral atoms given by Kissel *et al* [57]. As an example of how the

calculations are performed, we calculate here in detail, following Anholt [50], the differential cross section $\frac{d^2\sigma_{ion-atom}}{dE_{lab}d\Omega_{lab}}$ for 90 MeV/u $U^{88+} + N_2$ collisions at 90°. The electron energy in the projectile frame is 49.4 keV, so we use Kissel's tables for 50-keV electrons. At the short wavelength limit the fraction of energy radiated is 1 (*named by Kissel as* k/T1) and the angle in the projectile frame corresponding to the 90° laboratory angle is [50]

$$\theta_{proj} = \cos^{-1}(\frac{\cos\theta_{lab} - \beta}{1 - \beta\cos\theta_{lab}}) = 114.2^\circ \tag{4.11}$$

The bremsstrahlung-photon emission angle is always measured with respect to the direction of the incident free electron which is, in the case of inverse kinematics, opposite to the direction of the incident beam in the laboratory frame. Consequently, the bremsstrahlung emission angle is related to θ_{proj} as (*see figure* 4.10):

$$\theta_{brems} = 180 - \theta_{proj} = 65.8^\circ \tag{4.12}$$

The bremsstrahlung cross section is

$$\frac{d^2\sigma_{e-n}}{dE_{proj}d\Omega_{proj}} = S \times (spectrum) \times \frac{Z_p^2}{\beta^2 E_\gamma} \tag{4.13}$$

where Z_p is the projectile atomic number (92 *for uranium*), β is the speed in units of the speed of light (0.41 *for* 90 MeV/u), E_γ is the photon energy (49.4 *keV for the short wave length limit at* 90 MeV/u), S is the shape function defined as

$$S = \frac{d^2\sigma/dE_\gamma d\Omega}{d\sigma/dE_\gamma} \tag{4.14}$$

and "*spectrum*" is the scaled photon energy spectrum defined by Kissel as

$$spectrum = (\frac{\beta^2 E_\gamma}{Z_p^2})\frac{d\sigma}{dE_\gamma} \tag{4.15}$$

the entry for S and "*spectrum*" from the table are 0.1239 sr^{-1} and 5.599 mb respectively. which leads to

$$\frac{d^2\sigma_{e-n}}{dE_{proj}d\Omega_{proj}} = 0.707\ \frac{b}{keV\ sr} \tag{4.16}$$

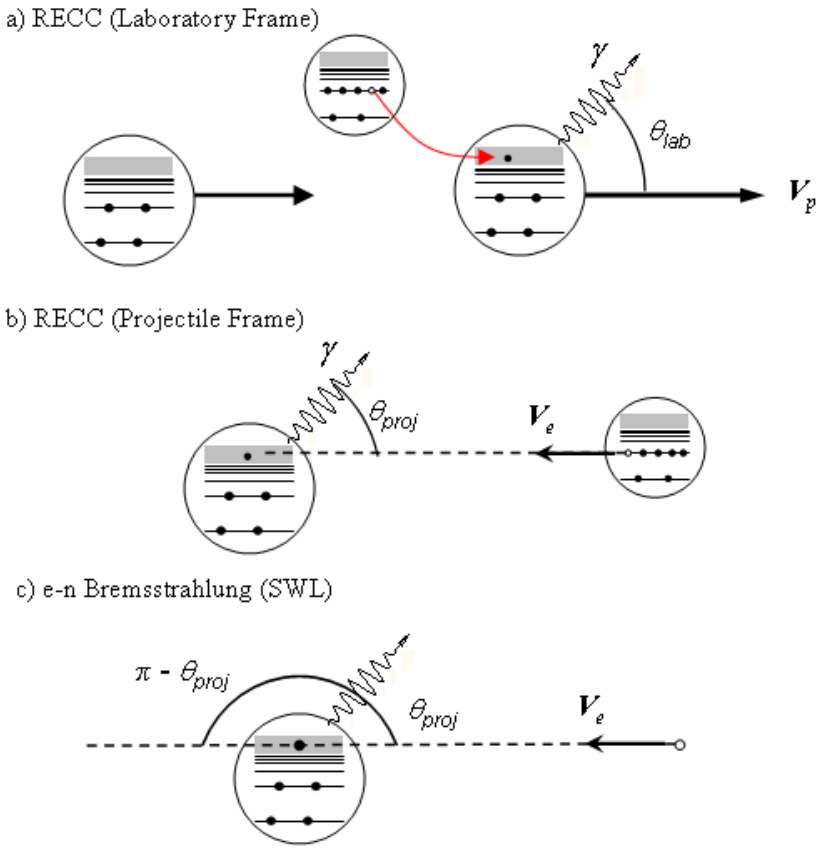

Figure 4.10: Illustration of radiative electron capture to continuum as seen in a) the laboratoray frame b) the projectile frame compared to c) the short wavelength limit of e-n bremsstralung process.

which can be now substituted together with Z_t=7 in equation (2.34) to give

$$\frac{d^2\sigma_{ion-atom}}{dE_{lab}d\Omega_{lab}} = 4.51\ \frac{b}{keV\ sr} \tag{4.17}$$

this procedure is repeated for all laboratory angles from $\theta = 0$ to $\theta = \pi$. The angular distribution of the resulting cross sections is presented in figure(4.11).

It is noteworthy that, this angular distribution of photons resulting from the short wavelength limit follows an approximate $\sin^2\theta$ distribution (*full line of figure* 4.11) at large angles in the domain $\sim 35^\circ < \theta <\sim 135^\circ$ which contains the location of our x-ray detector. A similar behavior is also reported [50, 189] for the radiative capture to bound states (REC) which gives an approximate $\sin^2\theta$ dependence at these energies. This gives an experimental support to the description of the RECC as a continuation of the REC across the ionization limit (*see chapter* 2).

Now the reduction in the azimuthal angle is obtained by performing a numerical integration for the resulting distribution. Integrating from $90^\circ - 9.548^\circ$ to $90^\circ + 9.458^\circ$ (*corresponds to the range* $[57.4^\circ - 74.8^\circ]$ *in the projectile frame*) gives a value of 1.842 in place of a value of 6.675 obtained for the respective integral on the total range from 0 to π, and thus a reduction by 1.842/6.675= 0.276. Thus a total reduction of $0.053 \times 0.276 = 0.0146 \approx 1/68$ leading to a δ factor of $\delta = 68$.

Using equation 4.10, the ECC differential cross section is calculated for every pass momentum p_n of the measurement cycle and normalized to the charge exchange rate seen by the particle detector for projectiles having undergone single electron capture. In figure (4.12), the resulting spectrum for the ECC is plotted together with the theoretical results (*full line*) after normalizing the experimental data to the theory in the peak maximum. It is to be noticed here that the shape of the resulting distribution is not very sensitive to the precision of the x-ray solid angle determination due to the very small cross section of the RECC process compared to the ELC Process ($\frac{d^2\sigma_{ELC}}{dpd\Omega} << \frac{d^2\sigma_{RECC}}{dpd\Omega}$). An error of 10% in the x-ray solid angle is estimated to generate an error of only 3% in the δ factor. This will have no significant effect on the resulting distribution.

In contrast to RECC, the ECC cusp spectrum is nearly symmetric within the width at half maximum. This is expected for the present semi-relativistic

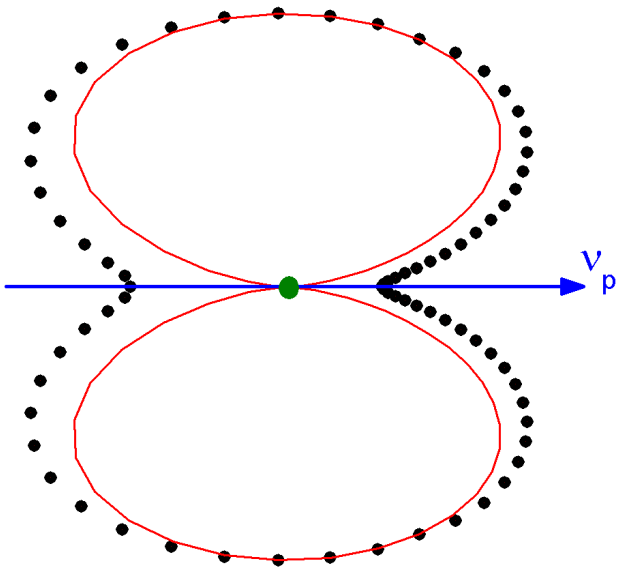

Figure 4.11: Calculated laboratory angular distribution of the short wavelength limit photons resulting from 90 MeV/u U^{88+} ions incident on N_2 gaseous target in comparison with the $sin^2\theta$ distribution (*full line*) expected for REC for weakly relativistic systems. Calculations are made with the help of tables of electron bremsstrahlung cross sections given by Kissel *et al* [57].

collision velocity since the ECC peak asymmetry has been reported to become weaker at higher velocities as $Z_p/v \rightarrow 0$ [52]. For cross sections lower than 30% of the peak maximum, a possible asymmetry is observed towards low electron energies in accordance with ECC cusp measurements at low collision energies [18]. As mentioned previously (*chapter* 2), the ECC process is described in terms of a double scattering mechanism, i.e. ejection of a target electron after being knocked by the projectile with a subsequent scattering by the target field. There, negative skewness is due to a final state interaction with the target ionic potential trying to keep the electrons at the target, i.e. pulling them to the low-energy side in the laboratory frame. This skewness in the ECC is opposite to the one found in the RECC (*figure* 4.7) and is in agreement with the theoretical prediction taking into account the distortion of the electron wave function in the final state. The theoretical calculations were carried out by Dr. Doris Jakubaßa-Amundsen (*LMU München*) within a relativistic formulation of the impulse approximation (*details in section* 4.4).

The figure clearly shows a qualitative agreement between the measured cross sections and the calculated ones concerning the cusp shape and the peak location with a much narrower calculated width (FWHM = 4.43 *a.u.*) compared to the measured one (FWHM = 6.81 *a.u.*). The difference between measured and calculated widths again shows that the presence of Rydberg atoms in the beam emerging from the target zone (*see section* 4.4) do indeed contribute significantly to the cusp peak. It is well known that such Rydberg states are readily formed in fast-ion collisions in gases [190]. If ECC electrons and Rydberg atoms were to emerge from the target in comparable numbers, the intensity and shape observed for the cusp peak would depend critically on the experimental parameters (*magnitude and direction of the spectrometer fields, distance from target to the spectrometer, ..etc.*). The inclusion of additional electrons arising from Rydberg atoms created at the target zone in the theoretical calculations is expected to increase the theoretical width to a value comparable with that of the measured distribution.

With increasing electron energy, on the high energy wing of the peak, a larger discrepancy between measured and calculated cross sections arises where theory predicts much smaller cross sections than observed in the experiment.

There is likely a considerable contribution from the projectile $M, N, ...$ Auger lines which would be situated at the wings of the peak when the Auger energies are transferred to the laboratory frame. Another contribution can originate from U^{88+} electrons emitted in a multiple electron loss to continuum. These electrons cannot be accounted in any contribution mentioned sofar because no coincidences were performed with U^{q+} (q= 90, 91, 92) ions. We surmise that electrons originating from multiple electron loss to continuum are ejected predominantly with laboratory velocities slightly higher than the projectile velocity. The contribution which originates from the low energy tail of the binary encounter peak centered at a momentum of

$$P_{BE} = \frac{2\gamma\sqrt{\gamma^2 - 1}}{\alpha} \tag{4.18}$$

which for 90 MeV/u U^{88+} equals to 135.3 a.u. can be here excluded at the momentum range presented due to the low atomic number (Z_t = 7) of the target and the associated narrow Compton profile.

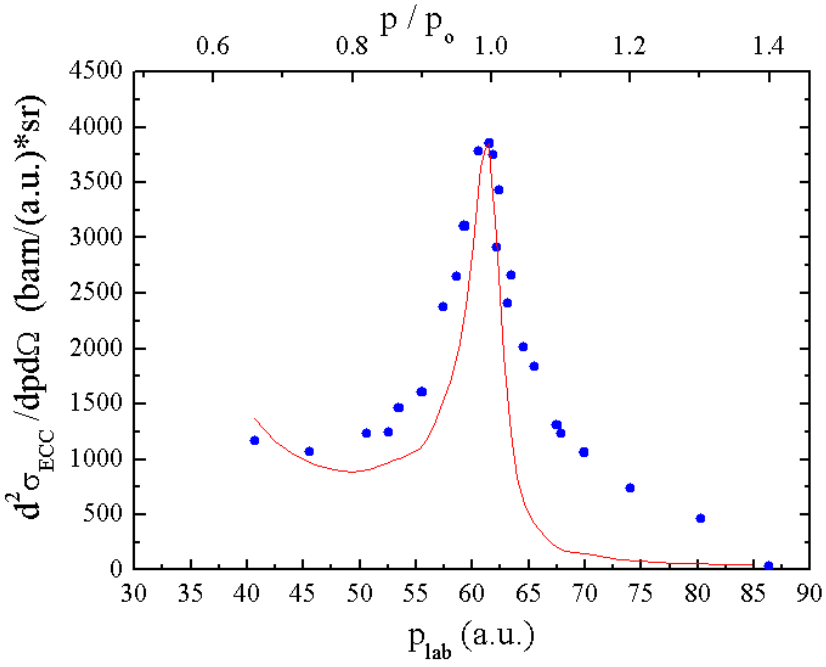

Figure 4.12: Double differential cross section $d^2\sigma/dpd\Omega$ for pure non-radiative electron capture to continuum in comparison with theory (*full line*) as a function of longitudinal electron momentum along the beam direction ($p = \beta\gamma/\alpha$) in the laboratory frame for 90 MeV/u U^{88+} ions incident on N_2 gaseous target. The electron relative momentum ($p/p_\circ$) scale appears at the top of the figure.

Chapter 5

Summary

In this work we have described the first in a planned series of experiments towards measuring the fully differential cross section of the electron-nucleus (e-n) bremsstrahlung at the short wavelength limit; we investigate its relation to the radiative electron capture to continuum RECC in which a target electron approximately at rest in the target frame is captured into a low-lying continuum state of a fast projectile with simultaneous photon emission. The RECC process as seen in the projectile frame (*a quasi-free electron from the target is decelerated from velocity* $v = v_{proj}$ *to* $v \approx 0$ *while emitting a photon of energy* $E = (\gamma - 1)mc^2$) is the kinematic inverse of the electron nucleus bremsstrahlung at the short wavelength limit (SWL). Interestingly, the inverse kinematic where the electron is detected with $v_{electron} \approx v_{Projectile}$ offers the only configuration to investigate the short wavelength limit of e-n bremsstrahlung.

As a first step, we have studied the forward electron emission in the collision of 90 MeV/u U^{88+} beryllium-like uranium impinging upon N_2 gaseous target. We detected electrons emitted with $v_{electron} \approx v_{Projectile}$ into a cone of half angle $\Delta\theta = \pm 1.5^\circ$ about the forward direction. Electrons were analyzed with our imaging forward electron spectrometer in the jet target zone of the experimental storage ring ESR at GSI and detected by means of our new 2D position sensitive electron detector. Moreover, electrons were detected in coincidence with x-rays collected with a Ge(i) detector mounted at 90° with respect to the beam axis.

In the coincident x-ray spectrum (*coincident with electrons emitted in the*

forward direction with the same speed as the projectile) we have observed for the very first time nearly exclusively photons from the short wavelength limit of electron nucleus bremsstrahlung (*figure* 4.4). X-ray spectra were also collected in coincident with electrons emitted in the forward direction for a set of electron velocities ($49\ a.u. < v_e < 61\ a.u.$) close to the projectile velocity of $v_p = 56.24\ a.u.$. The resulting coincident spectra (*figure* 4.6) show that spectra collected at velocities slightly lower than the cusp velocity contain much lower x-ray intensities compared to spectra collected at velocities slightly higher than the cusp velocity. This leads to the measured strong asymmetry toward the high energy side of the electron cusp distribution coincident with the RECC process (*figure* 4.7), as predicted by theory [7], which means an enhancement of emission of electrons parallel to the beam direction.

We have also detected electrons emitted in the forward direction in coincidence with the down charged projectile $U^{87+}(1s^2 2s^2 2p)$, a projectile asymptotically having captured simultaneously one electron into the $2p$ shell and one electron into its continuum. We have observed in this electron continuum spectrum coincident with capture to a projectile bound state a cusp-shaped distribution skewed towards the low energy side (*figure* 4.9) which points towards a non-radiative ECC process as the active mechanism. For comparison and momentum calibration we have measured simultaneously the electron loss to continuum ELC, Electron transfers from bound states of a projectile into continuum states of the projectile itself, by detecting coincidences between electrons emitted in the forward direction and projectiles which experienced a single electron loss U^{89+}. The resulting electron loss to continuum cusp (*figure* 4.3) exhibits a nearly symmetric line shape peaked at electron momentum corresponding to electrons traveling with the projectile velocity in agreement with theories.

Since a coincidence between electrons emitted in the forward direction and charge-unchanged projectiles (U^{88+}) is not possible from the practical point of view, the relative cross section for the non-radiative electron capture to projectile continuum was calculated indirectly by subtracting from the non-coincident cusp electron spectrum, all electrons detected by the electron detector, the number of counts of all other possible processes contributing to forward

electron emission other than the ECC. The resulting ECC cusp distribution (*figure* 4.12) was slightly skewed towards the low energy side in contrast to the RECC distribution.

We compare our results with the results of the theoretical calculations made by D. Jakubaßa-Amundsen for our system based on the relativistic formulation of the impulse approximation [7, 6]. Evidently we found satisfactory agreement between theory and experiment concerning cusp shape and cusp asymmetry.

We report in this work also first results from a study of the longitudinal momentum distribution in simultaneous ionization of target and projectile in 3.6 MeV/u Ne^{3+} and Ar target:

$$Ne^{3+} + Ar \rightarrow Ne^{4+} + Ar^{1+} + e_{fast} + e_{slow}$$

The measurement was performed using the GSI reaction microscope which will be joined in the close future to the forward electron spectrometer to enable for kinematically complete experiments at relativistic energies. The measured low energy electron emission was not nearly isotropic as expected for the present small perturbation but unexpectedly exhibits a strong forward asymmetry (*electrons are emitted predominantly in the forward direction*) while recoil ion momentum distribution has a peak at a small negative value of longitudinal momentum which means that recoil ions are emitted predominantly back to back with respect to the direction of emission of slow electrons (*figure* 3.26). The measured momentum distribution of the Ne^{4+} projectiles was a sharp peak with its center close to zero (*figure* 3.27). It follows that the slow electron longitudinal momentum is not balanced, as might be expected, by neither the longitudinal momentum change of the projectile nor the longitudinal momentum change of the projectile electron but mainly by the backward recoiling of the Ar^{1+} ion.

Chapter 6

Zusammenfassung

In dieser Arbeit beschreiben wir das erste in einer geplanten Experimentenserie zur Messung des vollständig differentiellen Wirkungs-Querschnitts der Elektron-Kern-Bremsstrahlung am kurzwelligen Limit. Klassisch wird Elektron-Kern-Bremsstrahlung erzeugt, wenn ein einlaufendes schnelles Elektron um Coulomb Feld des Kerns eines Targetatoms abgebremst wird. Das Elektron wird abgelenkt und verliert kinetische Energie. Die vom Elektron verlorene Energie wird in ein Photon der elektromagnetischen Strahlung umgewandelt (*Abbildung* 2.1). Das kurzwellige Limit der Elektron-Kern-Bremsstrahlung beschreibt die Situation, wenn die gesamte kinetische Energie des Elektrons in ein Photon umgewandelt wird und die kinetische Energie des auslaufenden Elektrons nah an null ist. Die strenge quantenmechanische Behandlung der Elektron-Kern-Bremsstrahlung zeigt darüber henaus, dass der StrahlungsProzess einen endlichen Querschnitt am kurzwelligen Limit hat, welches als scharfe Kante am hochfrequenten Ende des Strahlungsspektrums erscheint (*Abbildung* 2.9).

Wir untersuchen die Beziehung zwischen dem kurzwelligen Limit der Elektron-Kern-Bremsstrahlung und dem radiativen Elektroneneinfang ins Projektilkontinuum RECC (***R**adiative **E**lectron **C**apture to **C**ontinuum*). Im RECC wird ein Targetelektron aus dem Grundzustand des Targetsystems in einen energetisch niedrigliegenden Kontinuumzustand eines schnellen Projektils mit simultaner Photonemission eingefangen. Anstatt den Prozess im Laborsystem zu beschreiben, wo das Targetelektron im Grundzustand ist, kann der RECC im Ruhesystem des Projektils beschreiben werden. In diesem Fall sieht ein

Beobachter, der auf dem Projektil sitzt, dass das quasi-freie Targetelektron mit einer hohen kinetischen Energie $(\gamma - 1)mc^2$ ankommt, entsprechend der Geschwindigkeit des Projektils $v_e = v_{proj}$, dann abgebremst wird zu $v_e \approx 0$ unter Emission eines Photons von Energie $E = (\gamma - 1)mc^2$. Im Projektilsystem erscheint der RECC Prozess als das kinematisch Inverse des kurzwelligen Limits der Elektron-Kern Bremsstrahlung. Interessanterweise bietet die inverse Kinematik die einzige Konfiguration in der das kurzwelligen Limit der Elektron-Kern-Bremsstrahlung experimentell untersucht werden kann. Dies kann in den experimentellen Standardtechniken nicht geleistet werden. In experimentellen Standardkonfigurationen wird ein Photon und ein auslaufenden Elektron koinzident gemessen. Die Messung eines Elektrons koinzident mit dem Photon vom kurzwelligen Limit würde aber bedeuten, das dieses Elektron seine gesamte Energie verloren hat und deshalb das Target überhaupt nicht mehr verlassen kann.

Im Rahmen dieser Arbeit haben wir die Elektron-Kern-Bremsstrahlung und die Vorwärtselektronemission im Stoß von 90 MeV/u U^{88+} beryllium-ähnlichem Uran mit N_2 Gas Target untersucht. Wir haben Elektronen gemessen, die mit $v_e \approx v_{proj}$ in einen Kegel mit halbem Öffnungswinkel $\Delta\theta = \pm 1.5^\circ$ um die Vorwärtsrichtung emittiert werden. Die Elektronen werden mit einem Vorwärtselektronspektrometer analysiert, das in der Jettargetzone des experimentellen Speicherringes ESR in GSI in Darmstadt (www.gsi.de) für 0° Elektronenspektroskopie installiert ist. Das Vorwärtselektronen-spektrometer soll schnelle Elektronen analysieren, die in der Vorwärtsrichtung in einen schmalen Kegel um die Strahlrichtung emittiert werden und mit einem Orts- und Zeitempfindlichen Detektor nachgewiesen werden. Das Design des Spektrometers ist mittels elektronenoptische Rechnungen und Simulationen mit dem MIRKO Code [175] entwickelt worden. Das Spektrometer besteht aus einem 60° magnetischen Dipol mit Krümmungsradius 200 mm, der 940 mm von der Targetzone und sofort hinter der Targetkammer angebracht ist. Dieser Dipol wird von einem magnetischen Quadrupoletriplet mit 80 mm Blendenöffnung und einem zweiten 60° magnetischen Dipol, der mit dem ersten Dipol elektronenoptisch identisch ist, gefolgt. Darauf folgt ein Paar horizontale Schlitze zur Impulsdefinition, daran schließt sich ein 2D ortsempfindlicher multi-hit fähiger

Elektronendetektor an, der im Fokus des zweiten Dipolmagneten 40 *cm* hinter den Schlitzen positioniert ist.

Die Elektronen, die im Spektrometer analysiert werden, werden in Koinzidenz mit den Röntgenphotonen, die aus der Targetzone emittiert werden, gemessen. Die Röntgenphotonen werden mit einem Ge(i) Detektor nachgewiesen, der am Target unter 90° in Bezug auf die Strahlrichtung aufgebaut ist. Zeitkoinzidenzen werden zwischen den jenegen Elektronen gemessen, die in der Vorwärtsrichtung emittiert werden, und den Photonen, die unter 90° in Bezug auf die Strahlrichtung ausgesendet werden (*Abbildung* 4.1a). Ebenso zwischen den Elektronen und umgeladenen Projektilen U^{89+}, Elektronenverlust (*Abbildung* 4.1b), und zwischen den Elektronen und umgeladenen Projektilen U^{87+}, Elektroneneinfang (*Abbildung* 4.1c).

Im Koinzidenzeröntgenspektrum (*Koinzidenz von Röntgenphotonen mit den Elektronen, die in einen sehr engen Konus um die Vorwärtsrichtung mit der gleichen Geschwindigkeit wie das Projektil emittiert wurden*) haben wir erstmalig Photonen nahezu ausschließlich von dem kurzwelligen Limit der Elektron-Kern-Bremsstrahlung beobachtet (*Abbildung* 4.4). Für zwölf Elektronengeschwindigkeiten ($49\ a.u. < v_e < 61\ a.u.$) um die Projektilegeschwindigkeit von $v_p = 56.24\ a.u.$ wurden Röntgenspektren in Koinzidenz mit Elektronen, die in der Vorwärtsrichtung emittiert, gemessen. Die resultierenden koinzident Röntgenspektren (*Abbildung* 4.6) zeigen, dass die Röntgenspektren, die für Elektronengeschwindigkeiten unterhalb Cuspgeschwindigkeit gemessen werden, deutlich niedrigere Röntgenintensität enthalten, verglichen mit den Röntgenspektren, die für Elektrongeschwindigkeiten oberhalb der Cuspgeschwindigkeit gemessen werden. Dieses führt zu der gemessenen starken Asymmetrie der Cusplinie mit der höheren Intensität auf der Seite der hohen Impulse der Elektroncuspverteilung koinzident mit dem RECC Prozess (*Abbildung* 4.7), wie von der Theorie [7] vorausgesagt.

In dem hier vorgestellten Experiment konnte auch erstmals der Transfer IonisationsProzess (TI) bei relativistischen Geschwindigkeiten gemessen werden: wir haben die Elektronen, die in der Vorwärtsrichtung emittiert werden, in Koinzidenz mit dem umgeladenen Projektil $U^{87+}(1s^2 2s^2 2p)$ (*ein Projektil, das gleichzeitig ein Elektron anregt und ein Elektron in sein Kontinuum*

asymptotisch eingefangen hat) gemessen. Im resultierenden Kontinuumelektronenspektrum (*Abbildung* 4.9) haben wir eine cuspförmige Impulsverteilung beobachtet. Die Verteilung hat ein Maximum für Elektronimpuls von $p_e \approx 61.68\ a.u.$, das entspricht Elektronen, die sich mit der Projektilgeschwindigkeit von $v_p = 56.24\ a.u.$ bewegen. Das Spektrum ist asymmetrisch mit der höheren Intensität auf der Seite der niederen Impulse. Dies entspricht der Asymmetrie eines nicht-radiativen Elektroneneinfangs ins Projektilkontinuum ECC (***E****lectron* ***C****apture to* ***C****ontinuum*). Die gemessene Asymmetrie schließt als Mechanismus für den TI den Kanal Anregung und Einfang, gefolgt von Autoionisation, aus.

Zum Vergleich und zur Impulskalibrierung haben wir gleichzeitig den Elektronenverlust zum Kontinuum ELC (***E****lectron* ***L****oss to* ***C****ontinuum*) gemessen. ELC ist die Anregung eines Elektrons von einem gebundenen Zustand des Projektils in einem Kontinuumzustand des Projektils. ELC wird durch die Koinzidenz zwischen den Elektronen, die in der Vorwärtsrichtung emittiert werden und den umgeladenen Projektilen U^{89+} gemessen. Wir finden für das resultierende ELC Kontinuumelektronenspektrum (*Abbildung* 4.3) eine longitudinal nahezu symmetrische Verteilung. Die Verteilung hat ein Maximum bei einem Elektronimpuls von $\approx 61.68\ a.u.$, das entspricht Elektronen, die sich mit der Projektilgeschwindigkeit bewegen. Eine solche Symmetrie des longitudinale ELC Cusp wird von der ersten Bornshen Nährung vorhergesagt. Innerhalb der Nachweisempfindlichkeit wurden keine Photonen in Koinzidenz mit den ELC Elektronen gemessen. Das bedeutet, dass der ELC überwiegend nicht von einem simultanen radiativen Elektroneinfang in das Kontinuum begleitet ist.

Mittels den gemessenen koinzidenten Elektronenspektren konnten wir auch den nicht-radiative Elektroneneinfang in das Projektilkontinuum ECC (***E****lectron* ***C****apture to* ***C****ontinuum*) untersuchen. In dem ECC Prozess wird ein gebundenes Targetelektron in einen niedrigliegenden Kontinuumzustand des Projektils strahlungslos eingefangen. Da sich der Ladungszustand des Projektils in diesem Prozess nicht ändert ist eine Koinzidenz zwischen den Elektronen, die in der Vorwärtsrichtung emittiert werden, und um Ladungszustand unveränderte Projektile U^{88+} im Speicherring nicht möglich. Infolgedessen kann der relative

doppelte differentiale Querschnitt $\frac{d^2\sigma}{dpd\Omega}$ für den nicht-radiative Elektroneneinfang in das Projektilkontinuum ECC nicht direkt über Elektron-Projektile Koinzidenz gemessen werden, wie für das entsprechend ELC-Spektrum mit Koinzidenzen zwischen Cuspelektronen und U^{89+} Projektile möglich ist. Die fast 100% Nachweiswahrscheinlichkeit für umgeladene Projektile in den Teilchendetektoren [188] im Ring ermöglicht jedoch eine alternative indirekte Abschätzung der relativen Querschnitte von ECC durch Subtraktion der relativen differentiellen Querschnitte aller anderen möglichen Prozesse, die zur Vorwärtselektronemission anders als das ECC beitragen: ELC, RECC, und der kleine Beitrag von dem simultanen Elektroneneinfang zum gebundenen Zustand und Kontinuumzustand TI vom nicht-koinzidenten relativen differentialen Querschnitte (*alle Elektronen ermittelt durch den Elektrondetektor*). Die resultierende ECC Cuspverteilung (*Abbildung* 4.12) ist nahezu symmetrisch innerhalb der Halbwertsbreite. Dieses wird für die semi-relativistische Stoßgeschwindigkeit erwartet, weil die longitudinal Asymmetrie des ECC bei höheren Geschwindigkeiten ($Z_p/v \rightarrow 0$) abnimmt [52]. Auf der Flanke des Cusps unterhalb 30% des Maximums beobachten wir eine schwache Asymmetrie, zu kleinen Elektronenimpulsen, in Übereinstimmung mit den Cuspmessungen bei niedrigen Stoßenergien [18].

Wir vergleichen unsere experimentellen Ergebnisse mit den 90 MeV/u U^{88+} mit N_2 theoretischen Berechnungen, die von D. Jakubaßa-Amundsen für dieses System gemacht wurden. Die theoretische Berechnung basiert auf der relativistischen Formulierung der Impulsnäherung [6, 7]. Zwei grundlegende Annahmen wurden für molekulares N_2 Target innerhalb der relativistischen Impulsnäherung gemacht: (1) Das N_2 Targetsystem hat eine Struktur, dass die Inter-Kern Abstände verglichen mit den Stoßparameter charakteristisch für Elektron Anregung groß sind. (2) Die Wechselwirkung tritt über ein kurzes Zeitintervall auf, so dass die Umlaufzeit des N_2 Elektrons in seiner Bahn lang ist verglichen mit seiner Wechselwirkungszeit mit den U^{88+} Ionen. In dieser Situation kann der Effekt der molekularen Bindungskräfte während des Zusammenstoßes vernachlässigt werden. Anders gesagt, die locker gebundenen N_2 Elektronen werden als quasi-free Teilchen behandelt. Der Vergleich zwischen Experiment und Theorie zeigt offensichtlich eine sehr gute Übereinstimmung

der Messdaten mit den Resultaten der relativistische Impulsenäherung, besonders hinsichtlich der Cuspform und der Cuspasymmetrie. Der Vergleich zeigt aber auch, dass noch spezifische Diskrepanzen existieren.

Im Rahmen der vorliegenden Arbeit wurde auch das GSI Reaktionsmikroskop für Rückstoßionen und Elektronen als Teil des neues "*Extended Reaction Microscope*" in Betrieb genommen. Wir haben die Longitudinalimpulsverteilungen von niederenergetischen Elektronen sowie Rückstoßionen gemessen, die in der simultanen Ionisation von Projektil und Target in Stößen von 3.6 MeV/u Ne^{3+} mit Argon emittiert wurden: $Ne^{3+} + Ar \rightarrow Ne^{4+} + Ar^{1+} + e_{fast} + e_{slow}$

Die gemessene Emission von niederenergetischen Elektronen war nicht isotrop, wie eigentlich für die kleine Störung durch das Ne^{3+} Projektil erwartet ist, aber es zeigte eine unerwartete starke Vorwärtsasymmetrie (*Elektronen werden meistens in die Vorwärtsrichtung gestreut*). Die Rückstoßionenimpulsverteilung hat ein Maximum bei einem kleinen negativen Wert des Longitudinalimpulses, das bedeutet, dass Rückstoßionen überwiegend entgegengesetzt in Bezug auf die Richtung der Emission von langsamen Elektronen gestreut werden (*Abbildung* 3.26). Die gemessene Longitudinalimpulsverteilung der Ne^{4+} Projektile war einer scharfer Peak mit seiner Mitte nahe Impuls null (*Abbildung* 3.27). Es folgt, dass der Longitudinalimpuls des langsamen Elektrons weder durch die Longitudinalimpulsänderung vom Projektil noch durch die Longitudinalimpulsänderung vom Projektilelektron kompensiert wird, wie es vielleicht zu erwarten war, sondern hauptsächlich durch die rückwärtige Emission des Ar^{1+} Ions. Das GSI Reaktionsmikroskop ist inzwischen an das Vorwärtselektronenspektrometer am ESR Jettargetzone angeschlossen (*Herbst 2006*) um als "*Extended Reaction Microscope*" kinematisch komplette Experimente bei relativistischen Energie zu ermöglichen.

Chapter 7

A View into the Future

In the elementary process of electron nucleus bremsstrahlung at the short wavelength limit, the photon receives the entire kinetic energy of the incident electron and leaves the outgoing electron with virtually no kinetic energy and cannot be detected in coincidence with the emitted photon. Consequently, most of authors dealing with bremsstrahlung at the short wave length limit have considered either the doubly differential cross section, differential in photon energy and direction, integrated over the angles of the outgoing electrons or only the singly differential cross section, differential in photon energy, integrated over the angles of final electrons and photons [18, 38, 44, 191]. Theoretical calculations show that although the outgoing electrons have virtually zero velocity, their angular distribution is still correlated to the direction of emission of photons (*see section* 2.1.2) and the fully differential cross section for the short wavelength limit of electron nucleus Bremsstrahlung depends on the direction of the outgoing electron.

Using RECC as inverse kinematics we find ourselves in a situation where we can conceive an experiment in which the emission directions of the emitted photons and of the scattered electrons (*in the projectile frame*) are measured in coincidence in order to get the complete differential cross section for the short wavelength limit of Bremsstrahlung.

Apparently the emission direction of the photon is given by the location of the x-ray detector, whereas determination of the initial transverse momenta of the scattered electrons in the projectile reference frame and their azimuthal

distribution resulting from the ionizing collision is obtained from the information contained in the distribution of counts on the image of the 2D-PSD after careful electro-optical mapping of electrons from the target zone to the electron detector. For this purpose, the spectrometer needs to be operating in the telescopic imaging mode with the focus in the slit plane with narrow opening of the momentum defining slits.

It is further planned to measure the differential cross section of e-n bremsstrahlung including polarization correlations. It is reported [18] that the emitted radiation is totally polarized in the collision plane defined by the directions of the emitted photon and scattered electron. This is to be measured by an electron-photon coincidence experiment using a pixel x-ray detector sensitive to polarization of the emitted photons.

It is also planned to perform kinematically complete experiments at relativistic energies in which all momentum components of the collision products are determined in coincidence. This will be possible using the extended reaction microscope resulting from the combination of the forward electron spectrometer with our reaction microscope which is planned in the few months to come.

List of Figures

List of Tables

Bibliography

[1] D. H. Jakubassa-Amundsen, *Nucl. Instr. Meth. B* ***86*** , 82 (1994).

[2] M. E. Rudd and J. H. macek, *Vol* ***3****, ed M R C McDowell and E W McDaniel (Amsterdam: North Holland)* , 49 (1972).

[3] D. H. Jakubassa-Amundsen, *Lecture Notes in Physics, Vol.* ***213****, Springer, Berlin* , 17 (1984).

[4] M. Breining, S. B. Elston, S. Huldt, L. Liljeby, C. R. Vane, S. D. Berry, G. A. Glass, M. Schauer, I. A. Sellin, G. D. Alton, S. Datz, S. Overbury, R. Laubert, and M. Suter, *Phys. Rev. A* ***25*** , 3015 (1982).

[5] R. Shakeshaft and L. Spruch, *Phys. Rev. Lett.* ***41*** , 1037 (1978).

[6] D. Jakubassa-Amundsen, *J. Phys. B* ***16*** , 1767 (1983).

[7] D. Jakubassa-Amundsen, *J. Phys. B* ***36*** , 1971 ((2003).

[8] J. Burgdörfer, *Lecture Notes in Physics, Vol.* ***213****, Springer, Berlin* , 32 (1984).

[9] J. Macek, *Phys. Rev. A* ***1*** , 235 (1970).

[10] J. Burgdörfer, *Phys. Rev. A* ***33*** , 1578 (1986).

[11] J. S. Briggs and K. Dettmann, *J. Phys. B* ***10*** , 1113 (1977).

[12] J. S. Briggs and K. Dettmann, *Phys. Rev. Lett.* ***33*** , 1123 (1974).

[13] T. Stöhlker, T. Ludziejewski, H. Reich, F. Bosch, R. W. Dunford, J. Eichler, B. Franzke, C. Kozhuharov, G. Menzel, P. H. Mokler, F. Nolden, P. Rymuza, Z. Stachura, M. Steck, P. Swiat, A. Warczak, and T. Winkler, *Phys. Rev. A 58* , 2043 (1998).

[14] R. Shakeshaft and L. Spruch, *Rev. of Mod. Phys.* ***51*** , 369 (1979).

[15] W. Nakel, *Phys. Rep.* ***243*** , 317 (1994).

[16] M. Nofal, S. Hagmann, C. Kozhuharov, R. Moshammer, N. Lineva, and X. Wang, *GSI Scientefic Anuual Report* , 303 (2005).

[17] H. Kollmus, Ph.D. thesis, Universität Frankfurt, (2002).

[18] E. Haug and W. Nakel, *World Scientific Lecture Notes in Physics Vol. 73* ((2004).

[19] E. Haug and M. Keppler, *J. Phys. B* ***17*** , 2075 (1984).

[20] M. Komma and W. Nakel, *J. Phys. B* ***15*** , 1433 (1982).

[21] J. W. Motz, *Phys. Rev.* ***100*** , 1560 (1955).

[22] D. H. Rester, *Nucl. Phys. A* ***118*** , 129 (1968).

[23] E. Haug, *Phys. Lett. A* ***54*** , 339 (1975).

[24] W. Nakel and E. Pankau, *Phys. Lett. A* ***38*** , 307 (1972).

[25] W. Nakel and E. Pankau, *Phys. Lett. A* ***44*** , 65 (1973).

[26] W. Nakel and E. Pankau, *Z. Physik A* ***264*** , 139 (1973).

[27] W. Nakel and E. Pankau, *Z. Physik A* ***274*** , 319 (1975).

[28] O. Scherzer, *Ann. Phys. (Leipzig)* ***13*** , 137 (1932).

[29] W. Nakel, *Phys. Lett.* ***22*** , 614 (1966).

[30] W. Nakel, *Phys. Lett. A* ***25*** , 569 (1967).

[31] W. Nakel, *Z. Physik A* ***214*** , 168 (1968).

[32] H. W. Koch and J. W. Motz, *Rev. Mod. Phys.* ***31*** , 920 (1959).

[33] J. D. Jackson, *Wiley, New York* (1975).

[34] A. Aehlig and M. Scheer, *Z. Physik A* ***250*** , 235 (1972).

[35] R. Hub and W. Nakel, *Phys. Lett. A* ***24*** , 601 (1967).

[36] L. Kim and R. H. Pratt, *Phys. Rev. A* ***36*** , 45 (1987).

[37] H. Bethe and W. Heitler, *Proc. Roy. Soc. (London) Ser. A* ***145*** , 83 (1934).

[38] G. Elwert and E. Haug, *Phys. Rev.* ***183*** , 90 (1969).

[39] P. Kienle, M. Kleber, B. Povh, R. M. Diamond, F. S. Stephens, E. Grosse, M. R. Maier, and D. Proetel, *Phys. Rev. Lett.* ***32*** , 1099 (1973).

[40] A. Yamadera, K. Ishii, and K. Sera, *Phys. Rev. A* ***23*** , 24 (1981).

[41] T. Ludziejewski, T. Stöhlker, S. Keller, H. Beyer, F. Bosch, O. Brinzanescu, R. W. Dunford, B. Franzke, C. Kozhuharov, D. Liesen, A. E. Livingston, G. Menzel, J. Meier, P. H. Mokler, H. Reich, P. Rymuza, Z. Stachura, M. Steck, L. Stenner, P. ´Swiat, and A. Warczak, *J. Phys. B* ***31*** , 2601 (1998).

[42] R. Y. Yin, O. V. Gabriel, and R. H. Pratt, *Phys. Rev. A* ***36*** , 1207 (1987).

[43] E. Haug, Ph. D. thesis, University Tübingen (1996).

[44] U. Fano, H. W. Koch, and J. W. Motz, *Phys. Rev.* ***112*** , 1679 (1958).

[45] K. W. McVoy and U. Fano, *Phys. Rev.* ***116*** , 1168 (1959).

[46] R. H. Pratt, *Phys. Rev.* ***120*** , 1717 (1960).

[47] U. Fano, *Phys. Rev.* ***116*** , 1156 (1959).

[48] R. Anholt, S. Nagamiya, J. O. Rasmussen, J. G. Ioannou-Yannou, and E. Rauscher, *Phys. Rev. A* ***14*** , 2103 (1976).

[49] R. Anholt, J. G. Ioannou-Yannou, H. Bowman, E. Rauscher, S. Nagamiya, and J. O. Rasmussen, *Phys. Lett. A* ***59*** , 429 (1977).

[50] R. Anholt, C. Molitoris, D. W. Spooner, E. Morenzoni, S. A. Andriamonje, W. E. Meyerhof, H. Bowman, J.-S. Xu, Z.-Z. Xu, J. O. Rasmussen, and D. H. H. Hofmann, *Phys. Rev. A* ***33*** , 2270 (1986).

[51] D. H. Jakubassa and M. Kleber, *Z. Physik. A* ***273*** , 29 (1975).

[52] D. H. Jakubassa-Amundsen, *J. Phys. B* ***20*** , 325 (1987).

[53] J. E. G. Farina, *J. Phys. A* ***11*** , 1915 (1978).

[54] G. F. Chew, *Phys. Rev.* ***80*** , 196 (1950).

[55] W. Heitler, *"The Quantum Theory of radiation"*, Clarendon, Oxford, London, 242 (1954).

[56] C. MØller, *"The Theory of Relativity"*, Oxford University Press, (1952).

[57] L. Kissel, C. A. Quarles, and R. H. Pratt, *Atomic Data and Nuclear Data Tables* ***28*** , 381 (1983).

[58] K. Ishii and S. Morita, *Phys. Rev. A* ***31*** , 1168 (1985).

[59] K. Ozawa, J. H. Chang, Y. Yamamoto, S. Morita, and K. Ishii, *Phys. Rev. A* ***33*** , 3018 (1986).

[60] K. Ishii, K. Maeda, M. Takami, Y. Sasa, M. Uda, and S. Morita, *Nucl. Instr. Meth. B* ***75*** , 73 (1993).

[61] H. Tawara, T. Azuma, T. Ito, K. Komaki, Y. Yamazaki, T. Tonuma, K. Shima, A. Kitagawa, and E. Takada, *Phys. Rev. A* ***33*** , 3018 (1986).

[62] A. R. Sohval, J. P. Delvaille, K. Kalata, and H. W. Schnopper, *J. Phys. B* ***8*** , L426 (1975).

[63] C. B. Crooks and M. E. Rudd, *Phys. Rev. Lett* ***25*** , 1599 (1970).

[64] A. Salin, *J. Phys. B: Proc. Phys. Soc., London* ***2*** , 631 (1969).

[65] K. G. Harrison and M. W. Lucas, *Phys. lett. A* ***33*** , 142 (1970).

[66] K. Dettmann, K. G. Harrison, and M. W. Lucas, *J. Phys. B* ***7*** , 269 (1974).

[67] R. Cranage and M. W. Lucas, *J. Phys. B* ***9*** , 445 (1976).

[68] R. Strong and M. W. Lucas, *Phys. Rev. lett.* ***39*** , 1350 (1977).

[69] I. A. Sellin, *Journal de Physique* ***40****, No. 2* , C1 (1979).

[70] V. H. Ponce and W. Meckbach, *Comments At. Mol. Phys.* ***10*** , 231 (1981).

[71] K. O. Groenveld, W. Meckbach, I. A. Sellin, and J. Burgdörfer, *Comments At. Mol. Phys.* ***14*** , 187 (1984).

[72] F. Drepper and J. S. Briggs, *J. Phys. B* ***9*** , 2063 (1976).

[73] W. Meckbach, R. Vidal, P. Focke, I. B. Nemirovsky, and E. G. Lepera, *Phys. Rev. Lett.* ***52*** , 621 (1984).

[74] W. E. Wilson and L. H. Toburen, *Phys. Rev. A* ***7*** , 1535 (1973).

[75] D. Burch, H. Wieman, and W. B. Ingalls, *Phys. Rev. Lett.* ***30*** , 823 (1973).

[76] J. Macek, J. E. Potter, M. M. Duncan, M. G. Menendez, M. W. Lucas, and W. Steckelmacher, *Phys. Rev. Lett.* ***46*** , 1571 (1981).

[77] M. W. Lucas, W. Steckelmacher, J. Macek, and J. E. Potter, *J. Phys. B* ***13*** , 4833 (1980).

[78] S. D. Berry, G. A. Glass, I. A. Sellin, K.-O. Groeneveld, D. Hofmann, L. H. Andersen, M. Breinig, S. B. Elston, P. Engar, M. M. Schauer, N. Stolterfoht, H. Schmidt-Böcking, G. Nolte, and G. Schiwietz, *Phys. Rev. A* ***31*** , 1392 (1985).

[79] M. H. day, *J. Phys. B* ***13*** , L65 (1980).

[80] J. S. Briggs and F. Drepper, *J. Phys. B* ***11*** , 4033 (1978).

[81] K. C. R. Chiu, J. W. McGowan, and J. B. A. Mitchell, *J. Phys. B* ***11*** , L117 (1978).

[82] J. S. Briggs and M. H. Day, *J. Phys. B* ***13*** , 4797 (1980).

[83] J. S. Briggs, J. H. Macek, and K. Taulbjerg, *Comments At. Mol. Phys.* ***12*** , 1 (1982).

[84] E. C. Montenegro, W. S. Melo, W. E. Meyerhof, and A. G. de Pinho, *Phys. Rev. Lett.* ***69*** , 3033 (1992).

[85] R. Dörner, V. Mergel, R. Ali, U. Buck, C. L. Cocke, K. Froschauer, O. Jagutzki, S. Lencinas, W. E. Meyerhof, S. Nüttgens, R. E. Olson, H. Schmidt-Böcking, L. Spielberger, K. Tökesi, J. Ullrich, M. Unverzagt, and W. Wu, *Phys. Rev. Lett.* ***72*** , 3166 (1994).

[86] K. L. Bell, V. Dose, and A. E. Kingston, *J. Phys. B* ***3*** , 129 (1970).

[87] E. C. Montenegro and W. E. Meyerhof, *Phys. Rev. A* ***46*** , 5506 (1992).

[88] J. Burgdörfer, M. Breining, S. B. Elston, and I. A. Sellin, *Phys. Rev. A* ***28*** , 3277 (1983).

[89] R. Cranage, W. Steckelmacher, and M. W. Lucas, *Nucl. Instr. Meth.* ***194*** , 419 (1982).

[90] L. H. Thomas, *Proc. R. Soc.* ***114*** , 561 (1927).

[91] R. M. Drisko, Ph.D. Thesis, Cargegie Institue of technology, (1955).

[92] M. Suter, C. R. Vane, I. A. Sellin, S. B. Elston, G. D. Alton, R. S. Thoe, and R. Laubert, *Phys. Rev. Lett.* ***41*** , 399 (1978).

[93] M. RØdbro and F. Andersen, *J. Phys. B* ***12*** , 2883 (1979).

[94] W. Meckbach, I. B. Nemirovsky, and C. R. Garibotti, *Phys. Rev. A* ***24*** , 1793 (1981).

[95] A. Skutlartz, S. Hagmann, and H. Schmidt-Böcking, *J. Phys. B* ***21*** , 3609 (1988).

[96] C. R. vane, I. A. Sellin, S. B. Elston, M. Suter, R. S. Thoe, G. D. Alton, S. D. Berry, and G. A. Glass, *Phys. Rev. Lett.* ***43*** , 1388 (1979).

[97] N. Stolterfoht, R. D. DuBois, and R. D. Rivarola, *Springer Series on Atoms and Plasmas Vol* ***20*** (1997).

[98] H. Rothard, D. H. Jakubass-Amundsen, and A. Billebaud, *J. Phys. B* ***31*** , 1563 (1998).

[99] D. H. Jakubassa-Amundsen, *J. Phys. B* ***30*** , 365 (1997).

[100] F. Bell, M. Z. Wu, and H.-D. Betz, *J. Phys. B* ***16*** , 187 (1983).

[101] F. Bell and H. Böckl, *Nucl. Instr. Meth. B* ***2*** , 311 (1984).

[102] K. Kroneberger, M. Kuzel, R. Maier, M. Schosnig, C. Fiedler, M. Tobisch, M. J. ans S. Suarez, and K. O. Groeneveld, *Nucl. Instr. Meth. B* ***93*** , 142 (1994).

[103] D. R. Schultz and R. E. Olson, *J. Phys. B* ***24*** , 3409 (1991).

[104] C. Liao, S. Hagmann, C. P. Bhalla, S. R. Grabbe, C. L. Cocke, and P. Richard, *Phys. Rev. A* ***59*** , 2773 (1999).

[105] C. Liao, P. Richard, S. R. Grabbe, C. P. Bhalla, T. J. M. Zouros, and S. Hagmann, *Phys. Rev. A* ***50*** , 1328 (1994).

[106] R. Dörner, J. Ullrich, O. Jagutzki, A. gensmantel, and H. Schmidt-Böcking, *edited by W. R. MacGillivray, I. E. McCarthy, M. C. Standage, Adam Hilger IO Publishing, Bristol* , p. 351 (1991).

[107] J. Ullrich, Ph.D. Thesis, Johann-Wolfgang Goethe Universität Frankfurt, (1987).

[108] F. Afaneh, Ph.D. Thesis, Johann-Wolfgang Goethe Universität Frankfurt, (2001).

[109] V. Mergel, Diploma Thesis, Johann-Wolfgang Goethe Universität Frankfurt, (1994).

[110] J. Ullrich, R. Moshammer, R. Dörner, O. Jagutzki, V. Mergel, H. Schmidt-Böcking, , and L. Spielberger, *J. Phys. B* ***30*** , 2917 (1997).

[111] R. Moshammer, J. Ullrich, M. Unverzagt, W. Schmidt, P. Jardin, R. E. Olson, R. Mann, R. Dörner, V. Mergel, U. Buck, , and H. Schmidt-Böcking, *Phys. Rev. Lett.* ***73*** , 3371 (1994).

[112] R. Dörner, V. Mergel, O. Jagutzki, L. Spielberger, J. Ullrich, R. Moshammer, and H. Schmidt-Böcking, *Phys. Rep.* ***330*** , 95 (2000).

[113] V. D. Rodríguez, Y. D. Wang, and C. D. Lin, *Phys. Rev. A* ***52*** , R9 (1995).

[114] Y. D. Wang, V. D. Rodríguez, C. D. Lin, C. L. Cocke, S. Kravis, M. Abdallah, and R. Dörner, *Phys. Rev. A* ***53*** , 3278 (1996).

[115] P. Spädtke, J. Bossler, H. Emig, K. Leible, M. Khaouli, C. Mühle, S. Schennach, H. Schulte, and K. Tinschert, *C. Hill and M. Vertenar editors "Proceedings of the XVIII international linear accelerator conference", Geneva, Switzerland* (1996).

[116] P. Spädtke, F. Hezmach, R. Hollinger, R. Iannucci, R. Lang, H. Reich, H. Schulte, and K. Tinschert, *GSI (Annual report 2000), Darmstadt, Germany* (2001).

[117] B. Wolf, H. Emig, D. Rück, and P. Spädtke, *Rev. Sci. Instrum.* ***65*** , 3091 (1994).

[118] E. Oks, P. Spädtke, H. Emig, and B. Wolf, *Rev. Sci. Instr.* ***65*** , 3109 (1994).

[119] S. Yaramishev, W. Barth, L. Dahl, L. Groening, and S. Richter, p. 19 (2004).

[120] B.Franzke, K. Beckert, F. Bosch, H. Eickhoff, B.Franczak, A. Gruber, O. Klepper, F. Nolden, P. Raab, H. R. P. Spädtke, M. Steck, and J. Struckmeier, p. 1645 (1993).

[121] H. Geissel, T. Schwab, P. Armbruster, J. Dufour, E. Hanelt, K. Schmidt, B. Sherrill, and G. Münzenberg, *Nucl. Instr. Meth A* ***282*** , 247 (1989).

[122] B. Franzke, *GSI-ESR/TN-86-01 (Internal Report)* (1986).

[123] B. Franzke, *Nucl. Instr. Meth B* ***24/25*** , 18 (1987).

[124] N. Angert, W. Bourgeois, H. Emig, B. Franzke, B. Langenbeck, K. Leible, H. Schulte, P. Spädtke, and B. Wolf, "*Proceedings of the European Particle Accelerator Conference*", p. 1436, (1988).

[125] M. Steck, K. Beckert, H. Eickhoff, B.Franzke, F. Nolden, and P. Spädtke, "*Proceedings of the 1993 particle accelerator conference*", p. 1738, (1993).

[126] M. Steck, K. Beckert, P. Beller, B.Franzke, F. Nolden, U. Popp, and A. Schwinn, *Physica Scripta* ***T104*** , 64 (2003).

[127] M. Steck, K. Beckert, P. Beller, B. Franczak, B.Franzke, and F. Nolden, "*Proceedings of the European Particle Accelerator Conference, Vienna, Austria*", p. 587, (2000).

[128] M. Steck, *ICFA Workshop*, p. 542, (2004).

[129] M. Steck, K. Beckert, H. Eickhoff, B.Franzke, O. Klepper, R. Moshammer, F. Nolden, P. Spädtke, and T. Winkler, *eds. V. Suller and Ch. Petit-Jean-Genaz (World Scientific, Singapore)* , 1197 (1994).

[130] R. Hasse, *Phys. Rev. Lett.* ***83*** , 3430 (1999).

[131] J. Posser, "*Proceedings of the CAS: 5th Advanced Accelerator Physics Course*", Rhodes, Greece, p. 673, (1993).

[132] L. Groening, Ph.D. Thesis, University of Heidelberg, (1998).

[133] H. Danared, A. Källberg, K. Rensfelt, and A. Simonsson, *Phys. Rev. Lett.* ***88*** , 174801 ((2002).

[134] H. Totsuji, *Phys. Rev. A* ***46*** , 2106 (1992).

[135] F. Nolden, *GSI-ESR/TN-86-01 (Internal Report)* (1986).

[136] U. Schaaf, Ph. D. thesis, Universität Frankfurt, (1991).

[137] M. Steck, P. Beller, K. Beckert, B. Franzke, and F. Nolden, *Nucl. Instr. Meth. A* ***532*** , 357 ((2004).

[138] H. Reich, W. Bourgeois, B. Franzke, A. Kritzer, and V. Varentsov, *Nucl. Phys. A* ***626*** , 417c (1997).

[139] A. Krämer, Ph. D. Thesis, Universität Frankfurt, (2000).

[140] J. Eichler and T. Stöhlker, "*Radiative electron capture in relativistic ion-atom collisions and the photoelectric effect in hydrogen-like high-Z systems*", in print, (2006).

[141] T. Stöhlker, O. Brinzanescu, A. Krämer, T. Ludziejewski, X. Ma, and A. Warczak, *AIP Conference Proc. 506, (Chicago, Illinois, 1999)* , 389 ((2000).

[142] T. Stöhlker, T. Ludziejewski, F. Bosch, R. W. Dunford, C. Kozhuharov, P. H. Mokler, H. F. Beyer, O. Brinzanescu, B. Franzke, J. Eichler, A. Griegal, S. Hagmann, A. Ichihara, A. Krämer, J. Lekki, D. Liesen, F. Nolden, H. Reich, P. Rymuza, Z. Stachura, M. Steck, P. Swiat, and A. Warczak, *Phys. Rev. Lett* ***82*** , 3232 (1999).

[143] O. Klepper and C. Kozhuharov, *Nucl. Instr. in Physics Research B* ***204*** , 553 ((2003).

[144] J. Ullrich, R. Moshammer, A. Dorn, R. Dörner, L. ph H. Schmidt, and H. Schmidt-Böcking, *Rep. Prog. Phys.* ***66*** , 1463 ((2003).

[145] W. Wu, K. L. Wong, R. Ali, C. Y. Chen, C. L. Cocke, V. Frohne, J. P. Giese, M. Raphaelian, B. Walch, R. Dörner, V. Mergel, H. Schmidt-Böcking, , and W. E. Meyerhof, *Phys. Rev. Lett.* ***72*** , 3170 (1994).

[146] J. Ullrich and H. Schmidt-Böcking, *Phys. Lett. A* ***125*** , 193 (1987).

[147] J. Ullrich, M. Horbatsch, V. Dangendorf, S. Kelbch, and H. Schmidt-Böcking, *J. Phys. B* ***21*** , 611 (1988).

[148] J. Ullrich, H. Schmidt-Böcking, and C. Kelbch, *Nucl. Instr. Meth. A* ***268*** , 216 (1988).

[149] A. Martin, P. Jenlinsky, M. Lampton, and R. Malina, *Rev. Sci. Instr.* ***52*** , 1067 (1981).

[150] S. Sobottka and M. Williams, *IEEE Trans. Nucl. Sci.* ***35*** , 348 (1988).

[151] O. Jagutzki, V. Mergel, K. Ullmann-Pfleger, L. Spielberger, U. Meyer, R. Dörner, and H. Schmidt-Böcking, *Nucl. Instr. Meth., in: SPIE-Proc. No. 3438 & Imaging Spectroscopy IV' (Proceedings of the International Symposium on Optical Science, Engineering, and Instrumentation), San Diego, CA, USA* (1998).

[152] R. Moshammer, M. Unverzagt, W. Schmitt, J. Ullrich, and H. Schmidt-Böcking, *Nucl. Instr. Meth. B* ***108*** , 425 (1996).

[153] J. Ullrich, R. Moshammer, M. Unverzagt, W. Schmitt, P. Jardin, R. E. Olson, R. Dörner, V. Mergel, and H. Schmidt-Böcking, *Nucl. Instr. Meth. B* ***98*** , 375 (1995).

[154] S. Hagmann, T. Söthlker, J. Ullrich, C. Kozhuharov, R. Moshammer, H. Kollmus, R. Mann, and M. Nofal, *Nucl. Instr. Meth. B* ***205*** , 207 (2003).

[155] R. Dörner, H. Bräuning, J. M. Feagin, V. Mergel, O. Jagutzki, L. Spielberger, T. Vogt, H. Khemliche, M. H. Prior, J. Ullrich, C. L. Cocke, and H. Schmidt-Böcking, *Phys. Rev. A* ***57*** , 1074 (1998).

[156] H. Kollmus, Diploma thesis, Johann-Wolfgang-Geothe-Universität, Frankfurt, (1997).

[157] W. Wiley and I. McLaren, *Rev. Sci. Instr.* ***26*** , 1150 (1955).

[158] J. Ullrich and V. P. Shevelko, "*Many Particle Quantum Dynamics in Atomic and Molecular Fragmentation*": in Springer Series on Atoms and Plasmas, Vol. 35, (2003).

[159] R. Moshammer, J. Ullrich, M. Unverzagt, W. Schmitt, P. Jardin, R. E. Olson, R. Dörner, V. Mergel, and H. Schmidt-Böcking, *Nucl. Instr. Meth. B* ***107*** , 62 (1996).

[160] B. Fastrup, in: Methods of experimental Physics, Academic Press, New York, Vol. **17**, p. 149, (1980).

[161] H. Buchenau, E. L. Knuth, J. Northby, J. P. Toennies, , and C. Winkler, *J. Chem. Phys.* ***92*** , 6875 (1990).

[162] D. Miller, in: G. Scoles and D. Bassi and U. Buck and D. laine(Eds.) "*Atomic and Molecular Beam Methods*", Oxford University Press, New York, Vol. **14**, (1988).

[163] E. Eremina, Ph.D. thesis, Technischen Universität Berlin, (2005).

[164] J. P. Toennies and K. Winkelmann, *J. Chem. Phys.* ***66*** , 3965 (1977).

[165] W. Schmitt, Ph.D. thesis, Universität Frankfurt, (1999).

[166] A. Kantrowitz and J. Grey, *Rev. Sci. Instr.* ***22*** , 328 (1951).

[167] J. Braun, P. K. Day, J. P. Toennies, and G. Witte, *Rev. Sci. Instr.* ***68*** , 3001 (1997).

[168] V. Mergel, O. Jagutzki, L. Spielberger, K. Ullmann-Pfleger, R. Dörner, and H. Schmidt-Böcking, *Conference Proceedings of the MRS, Boston* (1997).

[169] RoentDek Handels GmbH, Frankfurt am Main, Germany, www.roentdek.de.

[170] G. Battistone, P. Campa, V. Chiarella, U. Denni, E. Iarocci, and G. Nicoletti, *Nucl. Instr. Meth.* ***202*** , 459 (1982).

[171] Mathematica, *Wolfram Research* , http://www.wolfram.com (1997).

[172] D. A. D. S. 3D, *Idaho National Lab (INL)* , http://www.simion.com (1995).

[173] J. Pedersen, P. Hvelplund, A. Petersen, and P. fainstein, *J. Phys. B* ***24*** , 4001 (1991).

[174] V. Rodríguez, Y. Wang, and C. Lin, *J. Phys. B* ***28*** , L471 (1995).

[175] B. J. Franczak, *GSI, Darmstadt-Germany* (1995), http://www-linux.gsi.de/∼redelbac/MIRKO/.

[176] K. Beckert, P. Beller, W. Bourgeous, F. N. B. Franzke, U. Popp, A. Schwinn, and M. Steck, *GSI (Annual report 2002), Darmstadt, Germany* ((2002).

[177] W. R. Leo, "*Techniques for Nuclear and Particle Physics Experiments*", Springer Verlag, p. 228, (1994).

[178] J. A. Bearden, *Rev. Mod. Phys.* ***39*** , 78 (1967).

[179] E. Browne, J. M. Dairiki, and R. E. Doebler, Table of Isotopes, John Wiley and Sons, INC, New York, p. 1450, (1978).

[180] S. I. Salem, S. L. Panossian, and R. A. Krause, *Atomic Data and Nuclear Data Tables* ***14*** , 91 (1974).

[181] A. Adamczewski, M. Al-turany, D. Bertini, H.G.Essel, and S. Linev, *GSI, Darmstadt* ((2005).

[182] Andrey Surzhykov, MPI Heidelberg, Private Communication (2006).

[183] J. P. Desclaux and P. Indelicato, *Input Data For relativistic Atomic Program MCDFGME V 2005.10* , france, (2005).

[184] M. R. C. McDowell, *Proc. R. Soc. A* ***264*** , 277 (1961).

[185] J. S. Briggs, *J. Phys. B* ***10*** , 3075 (1977).

[186] C. D. Shaffer, X.-M. Tong, and R. H. Pratt, *Phys. Rev. A* ***53*** , 4158 (1996).

[187] Z. Vager, B. J. Zabransky, D. Schneider, E. P. Kanter, G. Y. Zhuang, and D. S. Gemmell, *Phys. Rev. Lett.* ***48*** , 592 (1982).

[188] C. Kozhuharov, Private Communication, (2006).

[189] E. spindler, H.-D. Betz, and F. Bell, *Phys. Rev. Lett.* ***42*** , 832 (1979).

[190] A. C. Riviere, *Meth. Exp. Phys.* ***7A*** , 208 (1968).

[191] R. J. Jabbur and R. H. Pratt, *Phys. Rev.* ***129*** , 184 (1963).

Acknowledgements

It is hard to imagine how I would have done all of this without my **God**'s care. There were frequent moments I was disappointed throughout the years of my PhD, but through it all I believed that **God** looked after me and helped me. I truly thank my **God** every time I think of any single obstacle he helped me to overcome. Everything I accomplished or will accomplish in my life is the fruit of his mercy towards me.

Next, I would like to express my very special thanks to **Prof Dr. Horst Schmidt-Böcking**, **Prof. Dr. Reinhard Dörner**, **Prof. Dr. Thomas Stöhlker**, and **Prof. Dr. Heinz-Jürgen Kluge** for the acceptance and admittance of me as a PhD student in Frankfurt University and offering me their unique opportunity to collect a lot of experience and do this work. My special thanks are extended also to my close friend **M. Al-turany** who introduced and recommended me to them and helped me starting my life in Germany.

In the four and half years I spent in this PhD work, I have had the great pleasure to work with my direct advisor **Prof. Dr. Siegbert Hagmann** who introduced me into the field of experimental atomic physics and taught me the basics of electron spectroscopy. Because of his broad experience, Siegbert was a wonderful source of ideas and insights, I have learned an immense amount from him in millions of conversations in his office or in the laboratory. He has demonstrated nearly infinite patience in discussing our work. I thank Siegbert also for encouragement, guidance, constructive support and availability. One particularly nice aspect of having Siegbert as an advisor is his determination to teach me the German language. He talked to me always in German which gave me a fortune of words and sentences to help me cope with life in Germany.

I am infinitely grateful to **Dr. Doris Jakubaßa-Amundsen** for performing the theoretical calculations and for the very instructive discussions. I thank Doris also for communicating the unpublished theoretical data and information.

The important comments and financial support of **Prof. Dr. J. Ullrich** from Max Planck Institute is also highly appreciated.

I also appreciate the great assistance of **Dr. Ch. Kozhuharov**. His

enlightening discussions and important comments have been helpful and provided very useful guidance along the way. He has always the answer to any question, whether it concerns physics or any other topic (history, languages, ... etc).

I wish to express my thanks also to **Dr. Ottmar Jagutzki** for his assistance in building and optimizing the electron detectors. My thanks also go to **Dr. Nikolaus Kurz** from the experimental-electronic department of GSI for providing help in the laboratory computer network and data acquisition system. **A. Adamczewski** and **S. Linev** from the experimental-electronic department have given great assistance in the on-line and off-line analysis of my data concerning the analysis program Go4.

I would like also to thank all members of the GSI accelerator staff for all their help and kindness in preparing and tuning the UNILAC and ESR beam. My special thanks also go to the GSI mechanical workshop crew for their technical support which was crucial for the success of our experimental work. particularly I mention **Heinrich Wesp**, **Davide Racano** and **Markus Romig**.

The creation of this PhD work would not have been possible without the emotional support of my great wife **Rana Al-Halabi** who made my last four years substantially easier. I thank Rana for patience, understanding, sacrifices, bearing my absence during the long working hours, worrying about me everyday, and for the many happy moments we spent together. The Presence of my two kids **Laith** and **Wisam** has been a singular source of joy during the process of this work. I thank them for the nice environment at home, sense of humor, and for accepting many bad things to help me reach where I am.

My parents, **Mohammed Nofal** and **Mariam Nofal**, have both been a great source of support and encouragement throughout my life and the last four years have been no exception. I thank them both for teaching me things that have helped bring me this far. My **family in-low** in Saudia-Arabia and have also been very supportive and encouraging. I am also grateful to the rest of my family members and friends in Jordan, those who, in spite of the distance, were always close to me and conveyed the familiar feeling of home.

My niece **Enas Abu-Wardeh** deserves a special mention in this acknowledgement for her distinguished emotional support which kept me in great spirits throughout my PhD work. In fact, her contact with me during all the years of my Ph. D. work was very important and supportive for me.

A very special place in my thanksgiving I have to reserve for my former close friend and school-mate **Wael Ali** for his great friendship during 18 years (1986-2004) and for encouraging me at the first two years of this work. In fact his death at 3.11.2004 after 6 years of struggling against Leukemia was a great shock in my life. It saddens me that he is not alive to see this moment in my life. It is the minimum I can do to dedicate this work to his memory.

During my PhD, I was pleasantly surprised by the cooperative spirit among my colleagues in the atomic physics department. Among this crowd I must particularly thank **U. Spillmann**, **M. Trassinelli**, **H. Kollmus**, **R. Reuschel**, **X. Wang**, **S. Salem**, **A. Gumberidze**, **D. Banas**, **S.Trotsenko**, **S. Heß**, **S. Tachenov**, **C. Brandau**, and **S. Chatterjee**. I have had the great fortune to make good friends at various stages in my life and I am honored to count these among them. It was also always nice to deal with the staff of the atomic physics group at GSI: **R. Mann**, **F. Bosch**, **D. Liesen**, **H. Beyer**, **W. Nörtershäuser**, **P. Mokler**, **A. Bräuning-Demian**, **W. Ender**s, **O. Kester**, and **S. Lüttges**.

The financial support for this Ph.D. work was provided by the **Institute of Nuclear Physics** (*University of Frankfurt/Germany*), the **Max Planck Institute for Nuclear Physics** (*Heidelberg/Germany*), and the **Gesellschaft für Schwerionenforschung GSI** (*Darmstadt/Germany*). Together, all these sources provided me with the wonderful opportunity to study without being concerned about my finances during the work.

And last but not least, I would like to express my gratitude to all those people who have contributed to the completion and success of this work. I apologize if I have accidentally omitted somebody to whom acknowledgement is due.

Muaffaq Nofal